

NASA TECHNICAL NOTE



NASA TN D-4183

e.1

LOAN COPY: IN
AFWL COPY
KIRTLAND AFB, TX

0130854



TECH LIBRARY KAFB, NM

NASA TN D-4183

BODY MOTIONS AND ANGLES OF ATTACK
DURING PROJECT FIRE FLIGHT II REENTRY

by William I. Scallion and John H. Lewis, Jr.

Langley Research Center

Langley Station, Hampton, Va.



NATIONAL AERONAUTICS AND SPACE ADMINISTRATION • WASHINGTON, D. C. • OCTOBER 1967



0130854

NASA TN D-4183

BODY MOTIONS AND ANGLES OF ATTACK DURING
PROJECT FIRE FLIGHT II REENTRY

By William I. Scallion and John H. Lewis, Jr.

Langley Research Center
Langley Station, Hampton, Va.

NATIONAL AERONAUTICS AND SPACE ADMINISTRATION

For sale by the Clearinghouse for Federal Scientific and Technical Information
Springfield, Virginia 22151 - CFSTI price \$3.00

BODY MOTIONS AND ANGLES OF ATTACK DURING
PROJECT FIRE FLIGHT II REENTRY

By William I. Scallion and John H. Lewis, Jr.
Langley Research Center

SUMMARY

The angle-of-attack time history of the Project Fire reentry package was calculated from rate-gyro and accelerometer measurements telemetered during reentry. The measured rates and accelerations are also presented. The reentry velocity was about 11 327 m/sec at an altitude of 121 920 m and the flight-path angle was -14.74° .

The results indicate that the reentry package entered the sensible atmosphere at an angle of attack of about 3° . Subsequent to atmospheric encounter, the angle-of-attack envelope successively increased to levels of about 7.7° and 13° and to a maximum of about 19.5° near the end of the experimental period. These changes in angle of attack were caused by disturbances associated with the changing physical characteristics of the reentry package during reentry.

INTRODUCTION

Project Fire is a National Aeronautics and Space Administration research program undertaken to determine the hot-gas radiance and the total heat-transfer rates on a blunt-face body reentering the atmosphere at hyperbolic velocity. Results of the first flight have been published in references 1 to 5. The second and final flight occurred on May 22, 1965. Some of the results of this flight have been presented in references 6 to 11.

The primary purpose of this report is to present the calculated reentry-package angle-of-attack history, the basic body-motion data, and an analysis of the disturbances which caused the motions.

The body rate gyro and accelerometer data were used in conjunction with static aerodynamic wind-tunnel data to determine angles of attack. In addition, angles of attack for certain periods were obtained by computer simulation techniques. The angles of attack were obtained for velocities and altitudes ranging from 11 007 to 1109 m/sec and from 59 880 to 27 544 m, respectively. The ranges of velocity and altitude extended well beyond the significant heating experiment periods.

SYMBOLS

The positive directions of accelerations, angles, and angular rates are shown in figure 1. The coefficients and symbols used are as follows:

- a_N normal acceleration, $-a_Z$, g units
- a_X, a_Y, a_Z acceleration parallel to X_b -, Y_b -, and Z_b -axis, respectively, g units
- C_m pitching-moment coefficient, $\frac{M_Y}{\bar{q}Sd}$
- $C_{m,0}, C_{n,0}$ pitching- and yawing-moment coefficients due to asymmetries at $\alpha = 0^\circ$
- $C_{m\alpha}$ pitching-moment-curve slope per radian
- C_N normal-force coefficient, $\frac{-F_Z}{\bar{q}S}$
- $C_{N,0} = -C_{Z,0}$
- $C_{N\alpha}$ normal-force-curve slope per radian
- $C_{n\beta}$ yawing-moment-curve slope per radian
- C_R resultant-force coefficient in Y_b - Z_b plane
- C_X longitudinal-force coefficient, $\frac{F_X}{\bar{q}S}$
- C_Y lateral-force coefficient, $\frac{F_Y}{\bar{q}S}$
- $C_{Y,0}, C_{Z,0}$ force coefficient due to asymmetry along Y_b - and Z_b -axis, respectively, at $\alpha = 0^\circ$
- d reference diameter, meters
- F_X, F_Y, F_Z force along X_b -, Y_b -, and Z_b -axis, respectively, newtons
- g acceleration due to gravity at sea level, meters/second²
- H_{YZ} resultant angular momentum about Y_b - and Z_b -axes, newton-meter-second
- I_X, I_Y, I_Z mass moment of inertia about X_b -, Y_b -, and Z_b -axis, respectively, kilogram-meters²

M_Y, M_Z	moment about Y_b - and Z_b -axis, respectively, newton-meters
m	mass, kilograms
$m' = \frac{m\bar{V}}{qS}$	seconds
p, q, r	angular velocity about X_b -, Y_b -, and Z_b -axis, respectively, radians/second
\bar{q}	dynamic pressure, newtons/meter ²
q_{trim}, r_{trim}	angular velocity about Y_b - and Z_b -axis, respectively, caused by asymmetries, radians/second
S	reference area, meters ²
t	elapsed flight time, seconds
\bar{V}	earth-relative velocity, meters/second
X_b, Y_b, Z_b	orthogonal body-axis system with origin at center of gravity
X_g, Y_g, Z_g	orthogonal gravity-axis system with origin at center of gravity
x	longitudinal distance along X_b -axis from Fire station 0, meters
y_b, z_b	coordinate along Y_b - and Z_b -axis, respectively, meters
α	angle of attack, degrees
β	angle of sideslip, degrees
$\alpha_{trim}, \beta_{trim}$	angles of attack and sideslip caused by asymmetries, radians
γ_p	earth-relative flight-path angle, degrees
γ_y	earth-relative heading, degrees
η	total angle of attack, degrees

θ, ψ, ϕ body attitude angles relative to gravity-axis system, degrees

Subscripts:

cg center-of-gravity value

i indicated value

A dot over a symbol denotes differentiation with respect to time.

DESCRIPTION OF FLIGHT AND SPACE VEHICLE

Space Vehicle and Flight Profile

In general, the Project Fire flight II space vehicle consists of a powered spacecraft, composed of a velocity package with an Antares rocket motor and a reentry package, mounted atop an Atlas D launch vehicle. The space vehicle was launched from Cape Kennedy, Florida, down the Eastern Test Range to permit reentry into the Ascension Island area.

The Atlas D launch vehicle placed the flight II spacecraft into a precise ballistic trajectory along the Eastern Test Range. After separation from the Atlas D, the spacecraft was oriented to the proper Antares ignition attitude by the velocity-package control system. Just prior to Antares ignition, the spacecraft was spun up to approximately 158 revolutions per minute for spin stabilization and the velocity-package control system was jettisoned. Following burnout of the Antares rocket, the reentry package was separated from the spent motor by a spring mechanism and reentered the sensible atmosphere at a velocity of 11 326.6 m/sec at an altitude of 121 920 m. A more detailed description of the space vehicle and flight events may be found in reference 6.

Reentry Package

A sketch of the reentry package, which is the experimental portion of the Project Fire space vehicle and which contains the primary data-gathering system, is shown in figure 2. The package consists of a blunt forebody and a conical afterbody. The forebody consists of a multilayer arrangement of three beryllium calorimeters alternated with three phenolic-asbestos heat-protection shields. The physical characteristics and pertinent dimensions of the reentry package are given in table I.

The motion instrumentation contained in the reentry package consisted of three rate gyros and three linear accelerometers. The accelerometers were located off the center of gravity and therefore measured the combined effects of linear acceleration, angular

velocity, and angular acceleration. The measurement ranges of all the instruments and the accelerometer locations are listed in table II.

Reentry Events

The sequence of significant flight events during reentry is presented in table III. Following burnout of the Antares rocket motor, separation of the reentry package from the spent motor was indicated by telemetry as having occurred at an elapsed flight time of 1610.43 sec. Telemetry blackout occurred at an elapsed flight time of 1624.7 sec. The experimental heating data and motion data were recorded on a continuous tape during telemetry blackout and were replayed by way of telemetry after emergence from blackout. A sample of the telemetry record obtained after emergence from blackout is shown in figure 3. As shown in this figure, the rate-gyro data are relatively free of noise. Two of the several disturbances to the body can be seen on the pitch and yaw rate-gyro traces.

DATA REDUCTION

Measurements

The spacecraft flight measurements were telemetered to a ground receiving station where they were recorded on tape for later use. The station data tapes were read out and digitized on automatic equipment and the calibrations were applied with a digital computer program.

The digitized pitch and yaw rate-gyro data were smoothed by a digital frequency filter and then were differentiated. The smoothing operation was used primarily to assure smooth values of the angular accelerations \dot{q} and \dot{r} . Because the roll rate-gyro measurements were commutated at 5 points per second, the machine smoothing program could not be applied. These data were plotted and faired by hand to provide values of roll rate for the same times as for the pitch rate and yaw rate data. Although disturbances in the roll rate may exist, they cannot be distinguished from the scatter of the commutated data points; for this reason, only the trends in the data were faired.

The accelerometer data consisted of commutated measurements and therefore were obtained as discrete data points. The linear accelerometer data in the transverse plane (a_y, a_z) were commutated at the rate of 20 points per second and the longitudinal acceleration was commutated at the rate of 5 points per second. The transverse measurements were corrected for errors caused by off center-of-gravity displacements of the instrumentation. The longitudinal accelerometer data available for this analysis consisted of a 100-points-per-second interpolation of the original 5-points-per-second data.

Corrections and Accuracies

The data were corrected for filter lag resulting from the digital readout operation. Corrections were also applied to account for the variations in tape recorder speed during the flight.

The overall accuracy of the telemetry system was estimated to be 2.0 percent or 0.34 rad/sec for pitch and yaw rates, 0.49 rad/sec for roll rate, and 0.28g for the normal and transverse accelerometers.

The data scatter bands were evaluated by determining the root-mean-square deviation from the mean for several selected time periods. The deviation in pitch and yaw rates varied from 0.048 to 0.113 for the delay time data obtained during blackout and was 0.021 for the real time data obtained after blackout. Since the roll rate and accelerations were on the same commutator, the deviations for all these parameters were determined by assessing the roll rate scatter band. The roll rate deviation was 0.352 rad/sec and the deviation in acceleration was estimated to be 0.211g.

ANGLE-OF-ATTACK CALCULATIONS

Aerodynamic forces and moments were calculated from the accelerometer and rate-gyro data, respectively. Aerodynamic coefficients were then determined from the forces and moments and were used in conjunction with static aerodynamic wind-tunnel data to obtain values of angle of attack. In addition, angle-of-attack values were determined for certain short time periods by computer simulation techniques.

Moment Calculations

The smoothed pitch and yaw rate-gyro data were examined to identify the existence of trim conditions. Where trim conditions were found, values of q_{trim} and r_{trim} were recorded and were used to calculate $C_{m,0}$ and $C_{n,0}$ by the following method. The equations relating q_{trim} and r_{trim} to α_{trim} and β_{trim} , as given in reference 5, are

$$q_{\text{trim}} = p\beta_{\text{trim}} + \frac{C_{N\alpha}}{m'} \alpha_{\text{trim}} - \frac{C_{Z,0}}{m'}$$

$$r_{\text{trim}} = p\alpha_{\text{trim}} - \frac{C_{N\alpha}}{m'} \beta_{\text{trim}} + \frac{C_{Y,0}}{m'}$$

The last two terms are small for the range of altitudes and velocities in which trim effects existed and when they are neglected, $\beta_{\text{trim}} = \frac{q_{\text{trim}}}{p}$ and $\alpha_{\text{trim}} = \frac{r_{\text{trim}}}{p}$.

The values of $C_{n,o}$ and $C_{m,o}$ were then obtained from

$$C_{n,o} = -\beta_{\text{trim}} C_{n\beta}$$

and

$$C_{m,o} = -\alpha_{\text{trim}} C_{m\alpha}$$

By assuming that the in-flight asymmetries changed $C_{m,o}$ and $C_{n,o}$ but did not affect $C_{m\alpha}$ and $C_{n\beta}$, trim angle-of-attack conditions were accounted for by adjusting the wind-tunnel aerodynamic moment data for the calculated values of $C_{m,o}$ and $C_{n,o}$. Wind-tunnel tests have shown that this assumption is reasonable.

The smoothed p , q , and r data with the angular accelerations \dot{q} and \dot{r} were utilized in equations taken from reference 12 to compute the body moments as follows:

$$M_Y = \dot{q}I_Y + pr(I_X - I_Z)$$

$$M_Z = \dot{r}I_Z + pq(I_Y - I_X)$$

The aerodynamic moment coefficients were obtained by using the values of dynamic pressure taken from the Flight II reentry trajectory (ref. 6).

The variation of pitching-moment coefficient with angle of attack obtained from tests of a basic Apollo body shape in the Ames hypersonic free-flight facility at a Mach number of 35 is presented in figure 4. This aerodynamic moment data (adjusted where appropriate for $C_{m,o}$ and $C_{n,o}$), referenced to the center of gravity during the particular flight period, were used to determine the angle of attack α and angle of sideslip β . Once the values of α and β were determined, the value of total angle of attack η was obtained by calculating the magnitude of the vector sum of α and β .

Force Calculations

The aerodynamic force coefficients C_N and C_Y were calculated by using the following equations:

$$C_N = \frac{a_{N,cg} mg}{\bar{q}S}$$

and

$$C_Y = \frac{a_{Y,cg} mg}{\bar{q}S}$$

The dynamic pressures were obtained from reference 6. During the periods in which the rate-gyro data did not indicate any significant trim effects, the body was considered symmetrical, and the angles of attack and sideslip were determined as functions of the resultant force coefficient C_R obtained from reference 5 and shown in figure 4.

The accelerometer measurements were commutated at a frequency too low to permit interpolation of $a_{N, cg}$ and $a_{Y, cg}$ at the same time; therefore, the calculated values of α and β are not coincident in time. For this reason, the total angle of attack η could not be determined from the accelerometer measurements.

Where significant trim effects existed (between $t = 1652.7$ and 1662.5 sec), the angle-of-attack calculations were not considered valid because $C_{N, o}$ and $C_{Y, o}$ could not be determined without continuous data.

Simulations

The spacecraft angles of attack were also determined for several periods by the rate simulation techniques described in reference 5. Essentially, a curve-fit program utilizing the angular rate solution to the linearized equations of motion was used to match the rate-gyro data obtained in flight. The rates, angular accelerations, and frequencies obtained were used to calculate the initial conditions for input into a six-degree-of-freedom computer program (ref. 13) in which the body angles of attack and the acceleration of points on the body representing flight instrumentation locations are part of the output. These simulations were conducted for the following time periods:

$t = 1644.07$ to 1645.00 sec

$t = 1648.30$ to 1649.50 sec

$t = 1649.30$ to 1650.50 sec

$t = 1652.20$ to 1653.10 sec

$t = 1654.20$ to 1654.99 sec

$t = 1662.08$ to 1663.00 sec

RESULTS AND DISCUSSION

Basic Motion Data

The basic pitch and yaw rates as obtained from the flight data are plotted against elapsed flight time in figures 5 to 7. From separation to $t = 1640.38$ sec, only samples of the data are presented because the indicated rates are very small. From $t = 1640$ to 1666 sec, the data are presented continuously.

The effectiveness of the smoothing process is shown in figures 5, 6(a), and 7(a), where the smoothed rate-gyro data are compared with the flight data. The commutated roll rates and faired roll rates are shown in figure 8 as a function of elapsed flight time.

Portions of the commutated accelerometer data as received during the flight are presented as a function of elapsed flight time in figures 9 and 10. In figure 9 the uncorrected accelerations along the body longitudinal axis are compared with accelerations computed for the reentry trajectory of reference 6. The sparsity of the commutated normal and lateral acceleration data points did not permit an accurate definition of the variation of lateral and normal acceleration with time. For this reason, the transverse accelerations are presented in figure 10 only for the time periods for which the simulations provided a continuous variation for comparison. Although the accelerometer data are scattered, a pattern similar to the simulation curves is discernible but appears to be unaccountably displaced in time.

Disturbances in Motion

During the flight the reentry package experienced several disturbances beginning with separation. These disturbances appeared to be confined to angular impulses about the body pitch and yaw axes as shown by the changes in q and r in figures 5(a), 6(a), and 7(a).

With the exception of impulses occurring from about $t = 1658$ to 1662 sec (which is subsequently discussed), any angular impulses about the body roll axis were masked by the scatter of the commutated-roll-rate data. The resultant angular momentum about the Y_b - and Z_b -axes are shown as a function of elapsed flight time in figure 11. All the major body angular disturbances can be seen in this figure as increased values of angular momentum.

Reentry package separation occurred at $t = 1610.43$ sec (fig. 5(a)). The angular impulse at this time was 0.8745 N-m-sec with a calculated resultant moment of 10.927 N-m acting over a period of 0.08 sec. As can be seen in figure 2, the separation impulse is provided by a spring which, when compressed, exerts a force of 2112.905 N. Preflight calculations showed that, assuming no friction, the force ranged from the maximum compressed value to zero in approximately 0.073 sec, a time very close to the action time indicated by the rate data. The preflight estimated maximum off center alinement of this spring was 0.00777 m. Combining this misalignment distance with the average spring force of 1056.453 N results in a calculated tipoff moment of 8.209 N-m. Although the comparison between the preflight and the flight calculated tipoff moments are not exact, it is believed that the separation impulse was caused by the forces exerted between the separation spring and the reentry-package-afterbody mating surface.

The second disturbance occurred at $t = 1640.38$ sec (fig. 11). At this time, the first beryllium calorimeter was melting and the reentry package was losing the melted material simultaneously with changes in the shape of the front face because of the melting.

The angular impulse at this time was 6.440 N-m-sec. If one-third of the calorimeter was assumed to be lost at the time of the disturbance, the calculated resultant moment from this mass asymmetry was 7.891 N-m, as compared with a flight value of approximately 68 N-m. Even if the total mass of the calorimeter were asymmetrically located, it would cause a moment of only one-third of the flight value. The disturbance, then, cannot be completely caused by mass asymmetries; therefore, the aerodynamic effects of asymmetrical melting of the calorimeter were considered. The 68 N-m moment is equivalent to a pitching-moment coefficient of approximately 0.0125. The results of wind-tunnel tests at a Mach number of 4.63 on a model of the reentry package with several asymmetries on the calorimeter face are shown in figure 12. The pitching-moment coefficient at zero angle of attack ranged from -0.0007 for configuration B to 0.011 for configuration A. Although the configurations used in the tests cannot be considered to duplicate exactly the actual flight configuration, the test results do show that aerodynamic asymmetries on the face of the reentry package can cause pitching moments equivalent to those encountered in flight at the time of the disturbance. It can reasonably be concluded that the disturbance occurring at $t = 1640.38$ sec was caused by mass and/or aerodynamic asymmetries in the face of the melting beryllium calorimeter.

The third disturbance occurred at $t = 1648.18$ sec (fig. 11). The change in angular momentum at this time represents an angular impulse of approximately 9.49 N-m-sec. The duration of the disturbance was about 0.02 second. It has been established from the stagnation radiometer data and from photographs in appendix A of reference 11 that coincident with the disturbance the second phenolic-asbestos heat shield was moving off the face of the third calorimeter. Preflight calculations and wind-tunnel tests have shown that after the retaining link was released, the heat-shield sectors slid outward over the calorimeter face for approximately 0.016 second before aerodynamic loads caused them to tip over the outer edge of the calorimeter and begin to clear the reentry package. The total time to clear was estimated to be 0.021 second, about the duration of the disturbance. The movement of the heat-shield sectors is illustrated in figure 13. Although the nature of the disturbance could not definitely be established, it is believed to be associated with the ejection of the second phenolic-asbestos heat shield.

The last disturbance noted was different from the preceding ones in that it consisted of a series of disturbances beginning at about $t = 1652.7$ sec and lasting until about $t = 1662.7$ sec. As can be seen in figure 11, the variations in angular momentum were not as large as those shown for the two previous disturbances. The first disturbance at $t = 1652.7$ sec resulted in trim values of q and r (figs. 7(d) and 7(e)) and, consequently, a trim angle of attack. The second in the series of disturbances occurred at $t \approx 1656.5$ sec (fig. 11). The effect of a third disturbance is shown in figure 8, where at $t = 1658$ sec the roll rate experienced a rapid reduction from 13.6 rad/sec to 6.6 rad/sec at $t = 1662$ sec. Also, a fairly sharp reduction in angular momentum H_{YZ}

between $t = 1661.5$ and 1662.5 sec is shown in figure 11. After this time, the trim values of q and r are reduced to zero, and the roll rate remains fairly constant.

Although the source of these disturbances is not known, there is a definite correlation with the behavior of the beryllium calorimeter thermocouple outputs. Between $t = 1652$ and 1653.8 sec, an entire radial line of thermocouples from the stagnation point to the rim of the calorimeter failed to register. This failure indicated that either the thermocouple leads were broken or burned through. Another radial line of thermocouples also failed to register between $t = 1656.5$ and 1657.2 sec. Although none of the thermocouples indicated temperatures high enough for melt, it is possible that the thin portions of the calorimeter (between the thermocouple radial lines) melted through; this allowed hot gas to burn through the thermocouple leads behind the beryllium. The resulting asymmetries in the beryllium face could produce the aerodynamic moments necessary to maintain a trim angle of attack and to reduce the roll rate. The return to a symmetrical trim condition at $t = 1662.7$ sec (fig. 7(m)) could be caused by a complete loss of the calorimeter at this time. This hypothesis cannot be substantiated because reduced calorimeter data beyond $t = 1662$ sec were not available.

Angle-of-Attack Data

Separation to $t = 1640.2$ sec.- The reentry-package longitudinal axis was not aligned with the velocity vector at separation. The attitude of the reentry stage relative to the gravity-axis system at ignition was known, and this information, coupled with the assumption that the spin-stabilized stage remained at a fixed inertial orientation from ignition to separation, yielded an estimate of the attitude at separation. The angle between the reentry-package longitudinal axis and the velocity vector at separation was estimated to be 1.52° . The coning half-angle subsequent to separation was about 0.8° and the resulting angle between the reentry-package longitudinal axis and the velocity vector oscillated between 0.72° and 2.32° before reentry into the sensible atmosphere. In order to determine whether the reentry package would trim to a symmetrical motion pattern about the velocity vector after entering the atmosphere, a six-degree-of-freedom trajectory simulation was generated from separation to $t = 1640$ sec. The simulation results showed that the body motions were symmetrical about the velocity vector by $t = 1640$ sec and that the maximum value of η ranged from 2.3° at separation to 2° at $t = 1640$ sec.

The total angles of attack calculated from the flight measurements just prior to the first beryllium calorimeter melting ($t = 1635.4$ to 1640.2 sec) are shown in figure 14. The maximum value of η generally ranged between 1° and 4° . The erratic variation of η with elapsed flight time is indicative of the rate-gyro data scatter shown in figures 5(c) and 5(d). Because of the scatter in the flight data, it was concluded that a maximum total angle-of-attack value of 2° to 3° as obtained from the simulation would be more representative of the total angle of attack from separation to $t = 1640$ seconds.

t = 1640.2 to 1666 sec.- The angles of attack and sideslip derived from the flight rate-gyro measurements are presented as functions of elapsed time in figures 15 and 16. The angles of attack and sideslip derived from the accelerometer measurements for periods when trim angles of attack were negligible are presented in figures 15, 16(a), 16(b), 16(c), 16(d), 16(e), 16(m), 16(n), and 16(o). The angles of attack obtained from the digital simulations are also shown for comparison in figures 15(d), 16(a), 16(b), 16(c), 16(e), 16(f), 16(g), and 16(m).

Poor agreement between the rate data and accelerometer data cannot be satisfactorily explained. In some of the figures (figs. 15(e), 15(f), and 16(d), for example) can be seen a trend in the angles of attack derived from the accelerometer data that is similar to the trend of the curves derived from the rate data. A comparison of these angle-of-attack data suggests a time displacement similar to that noted for the accelerometer data in figure 10.

The digital simulation results are in good agreement with the angles of attack calculated from the flight measurements (figs. 15 and 16). This agreement is expected since the rate data and the static wind-tunnel aerodynamics were the sources of the input data for the digital simulations. The slight differences between the flight data and the simulation results are caused by corresponding differences in the product of $C_{m\alpha}$ and \bar{q} which are functions of the accuracies of the wind-tunnel aerodynamic data and the atmospheric density measurements. The product $C_{m\alpha}\bar{q}$ used in calculating α and β from the rate-gyro measurements was composed of the wind-tunnel value of $C_{m\alpha}$ and the dynamic pressures of reference 6. The product $C_{m\alpha}\bar{q}$ used to determine simulation initial conditions was calculated to achieve a close match of the frequencies of the flight pitch and yaw rates. For convenience, the wind-tunnel value of $C_{m\alpha}$ was used and \bar{q} was varied to provide the required product. Since the same $C_{m\alpha}$ was used in both methods, the differences in \bar{q} are a direct measure of the differences in the product $C_{m\alpha}\bar{q}$. In figure 17 are presented a time history of \bar{q} from the Flight II reentry trajectory (ref. 6) and values of \bar{q} required by the present simulations. Corresponding differences in the altitude-velocity-profile are shown in figure 18. These differences are considered small and may be accounted for by uncertainties in the atmospheric measurements or the wind-tunnel data, or both.

Total angle-of-attack envelope.- The total angle-of-attack envelope is presented in figure 19 and includes the maximum and minimum bounds of oscillations. The disturbances at $t \approx 1640.38$ sec and 1648.18 sec are readily apparent. The maximum total angle of attack increased to approximately 7.7° at $t = 1640.38$ sec and gradually decreased to 5° prior to the next disturbance caused by ejection of the second heat shield. This disturbance ($t = 1648.18$ sec) increased the maximum value of η to over 13° . The maximum total angle of attack reached 19.5° when the disturbance

beginning at $t = 1652.7$ sec produced a trimmed angle of attack of approximately 7° . The trim condition persisted until about $t = 1662$ sec, after which the trim angle of attack decreased to zero. The subsequent values of η increased as the dynamic pressure decreased.

Assessment of Measurement System

In general, the rate measurements were found to be sufficient to determine the body angles of attack with a reasonable degree of accuracy. The commutated accelerometer measurements neither adequately nor accurately defined the envelope of body attitudes during the reentry; however, it is believed that continuous accelerometer measurements, compensated for locations off the center of gravity, would do so.

SUMMARY OF RESULTS

The results of an analysis of the rate-gyro and accelerometer data from the Project Fire Flight II reentry package are summarized as follows:

1. The angular motions of the reentry package were caused by several discrete disturbances and a prolonged disturbance during reentry. The origins of the disturbances were associated with the changing physical properties of the reentry package, such as asymmetric melting of the beryllium calorimeters and ejection of the phenolic-asbestos heat shields.

2. The reentry-package maximum total angle of attack ranged from 2° to 3° from separation to the melting of the first beryllium calorimeter and subsequently varied from an initial value of about 7.7° to approximately 5° just prior to ejection of the second heat shield. The maximum total angle of attack increased to about 13° during the second heat-shield ejection and remained near this value for about 5 seconds and then increased to about 19.5° .

3. The variation of angle of attack with time could not be adequately defined from the commutated accelerometer data.

4. A comparison of the combined aerodynamic and atmospheric parameters used in the angle-of-attack calculations with those used in the simulations showed that the uncertainties in the atmospheric properties and wind-tunnel data used in the angle-of-attack calculations were small.

Langley Research Center,

National Aeronautics and Space Administration,

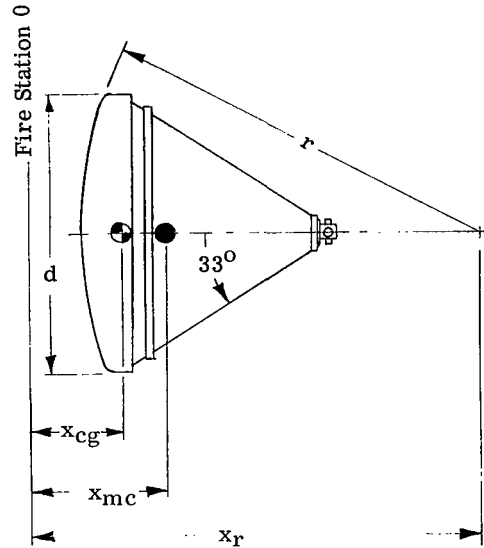
Langley Station, Hampton, Va., May 11, 1967,

714-00-00-01-23.

REFERENCES

1. Scallion, William I.; and Lewis, John H., Jr.: Flight Parameters and Vehicle Performance for Project Fire Flight 1, Launched April 14, 1964. NASA TN D-2996, 1965.
2. Cornette, Elden S.: Forebody Temperatures and Total Heating Rates Measured During Project Fire 1 Reentry at 38 000 Feet Per Second. NASA TM X-1120, 1965.
3. Cauchon, Dona L.: Project Fire Flight 1 Radiative Heating Experiment. NASA TM X-1222, 1966.
4. Slocumb, Travis H., Jr.: Project Fire Flight 1 Heating and Pressure Measurements on the Reentry-Vehicle Afterbody at a Velocity of 38 000 Feet Per Second. NASA TM X-1178, 1965.
5. Woodbury, Gerard E.: Angle-of-Attack Analysis for Project Fire 1 Payload Reentry Flight. NASA TN D-3366, 1966.
6. Lewis, John H., Jr.; and Scallion, William I.: Flight Parameters and Vehicle Performance for Project Fire Flight II, Launched May 22, 1965. NASA TN D-3569, 1966.
7. Cornette, Elden S.: Forebody Temperatures and Calorimeter Heating Rates Measured During Project Fire II Reentry at 11.35 Kilometers Per Second. NASA TM X-1305, 1966.
8. Cauchon, Dona L.: Radiative Heating Results From the Fire II Flight Experiment at a Reentry Velocity of 11.4 Kilometers Per Second. NASA TM X-1402, 1967.
9. Slocumb, Travis H., Jr.: Project Fire Flight II Afterbody Temperatures and Pressures at 11.35 Kilometers Per Second (37 200 Feet Per Second). NASA TM X-1319, 1966.
10. Richardson, Norman R.: Project Fire Instrumentation for Radiative Heating and Related Measurements. NASA TN D-3646, 1966.
11. McKee, Charles W.: Project Fire Photographic Summary and Record of Reentry Phenomena at Hyperbolic Velocities. NASA TN D-3571, 1966.
12. Lovelace, Uriel M.; Hoffman, Sherwood; and Mayhue, Robert J.: Analysis of the Trajectory and Large-Amplitude Motions of a Scout Vehicle During Fourth-Stage Reentry Flight. NASA TN D-2309, 1964.
13. Dennison, A. J.; and Butler, J. F.: Missile and Satellite Systems Program for the I.B.M. 7090. Tech. Inform. Ser. No. 61 SD 170, Missile and Space Vehicle Dept., Gen. Elec. Co., Feb. 1962.

TABLE I.- PHYSICAL CHARACTERISTICS OF REENTRY PACKAGE



Configuration	Mass, kg	x_{cg} , m	I_X , kg-m ²	I_Y , kg-m ²	I_Z , kg-m ²	d, m	r, m	x_r , m	¹ x_{mc} , m
Complete reentry package (t = 1617.75 to 1639.7 sec)	86.586	0.277	3.511	2.806	2.874	0.672	0.935	1.048	0.306
Less first calorimeter (t = 1640.48 to 1642.12 sec)	83.189	.282	3.281	2.644	2.698	.651	.929	1.048	.307
Less first phenolic layer (t = 1642.12 to 1645.26 sec)	76.022	.293	2.806	2.305	2.359	.630	.805	.937	.313
Less second calorimeter (t = 1646.1 to 1647.5 sec)	72.166	.299	2.562	2.128	2.183	.607	.799	.937	.319
² Less second phenolic layer (t = 1647.53 sec to end of flight)	66.179	.309	2.183	1.857	1.925	.587	.702	.852	.322

$${}^1x_{mc} = x_r - r + 0.2875d.$$

²Thermocouple instrumentation indicated that the third beryllium calorimeter did not completely melt; therefore, for data reduction purposes, the mass and inertia of the reentry package were arbitrarily kept constant subsequent to t = 1647.53 seconds.

TABLE II. - MOTION INSTRUMENTATION

Motion instrument	Measurement range	Location		
		x, m	y _b , m	z _b , m
Axial accelerometer (a _x)	0 to -120g	0.3099	0.0475	-0.0394
Transverse accelerometer (a _y)	+6g to -6g	.3968	0	-.0315
Normal accelerometer (a _z)	+6g to -6g	.3968	.0546	0
Roll rate gyro (p)	0 to 24.5 rad/sec			
Pitch rate gyro (q)	±7.0 rad/sec			
Yaw rate gyro (r)	±7.0 rad/sec			

TABLE III. - SEQUENCE OF EVENTS DURING REENTRY

Event	Elapsed flight time, t, sec
Reentry-package separation (first disturbance)	1610.43
Arrival at altitude of 121 920 meters (400 000 feet)	1617.75
Begin telemetry blackout	1624.70
Begin C-band radar blackout	1629.00
Start reentry timer (10.4g deceleration)	1639.11
Second disturbance	1640.38
First heat-shield ejection (signal)	1642.12
Second heat-shield ejection (signal)	1647.53
Third disturbance	1648.18
End telemetry blackout	1655.1
Reentry-package impact	1934.3

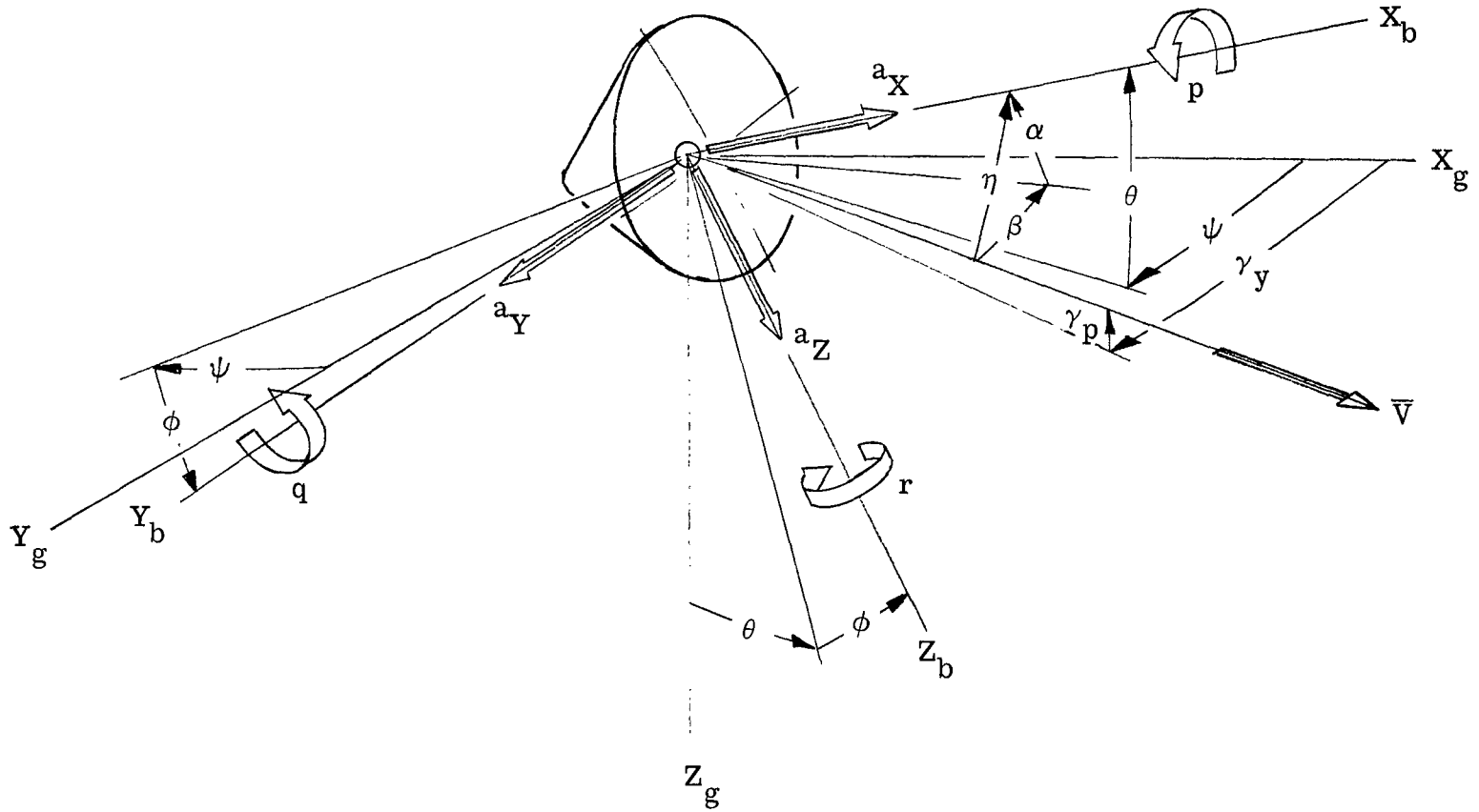


Figure 1.- Axis systems and sign conventions.

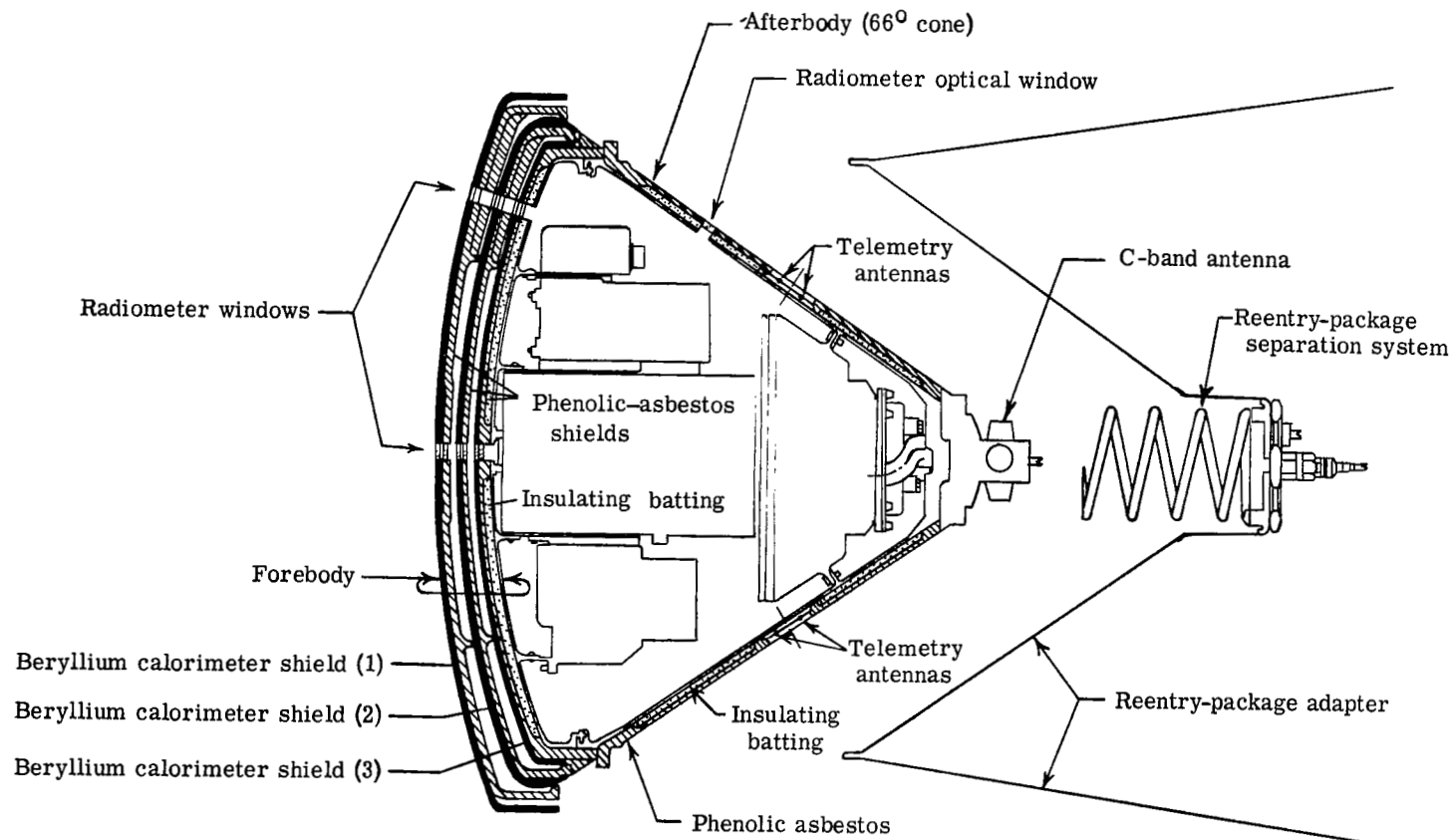


Figure 2.- Sketch of Project Fire reentry package and adapter.

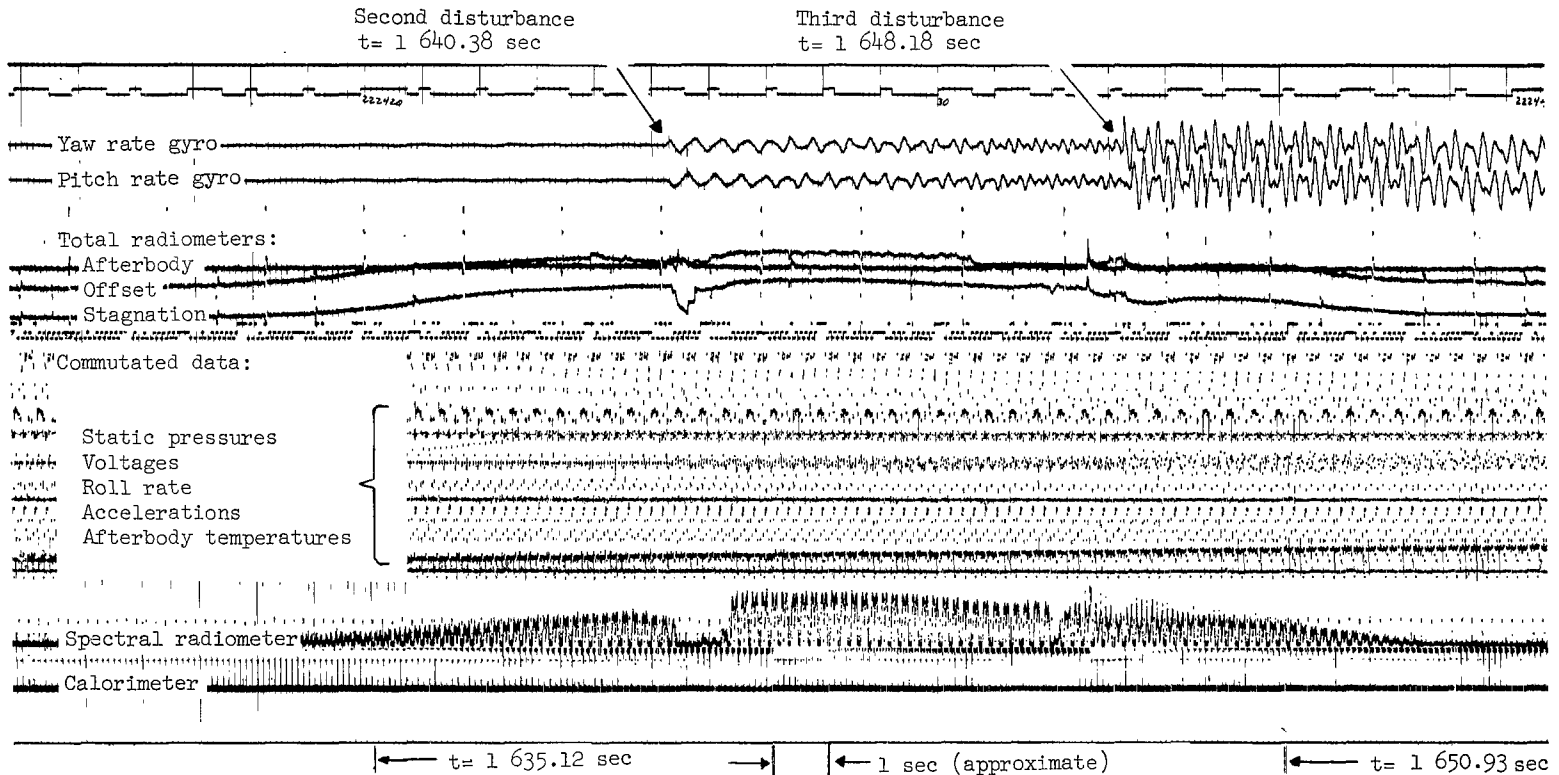


Figure 3.- Sample of telemetered data received by Ascension Island telemetry receiver.

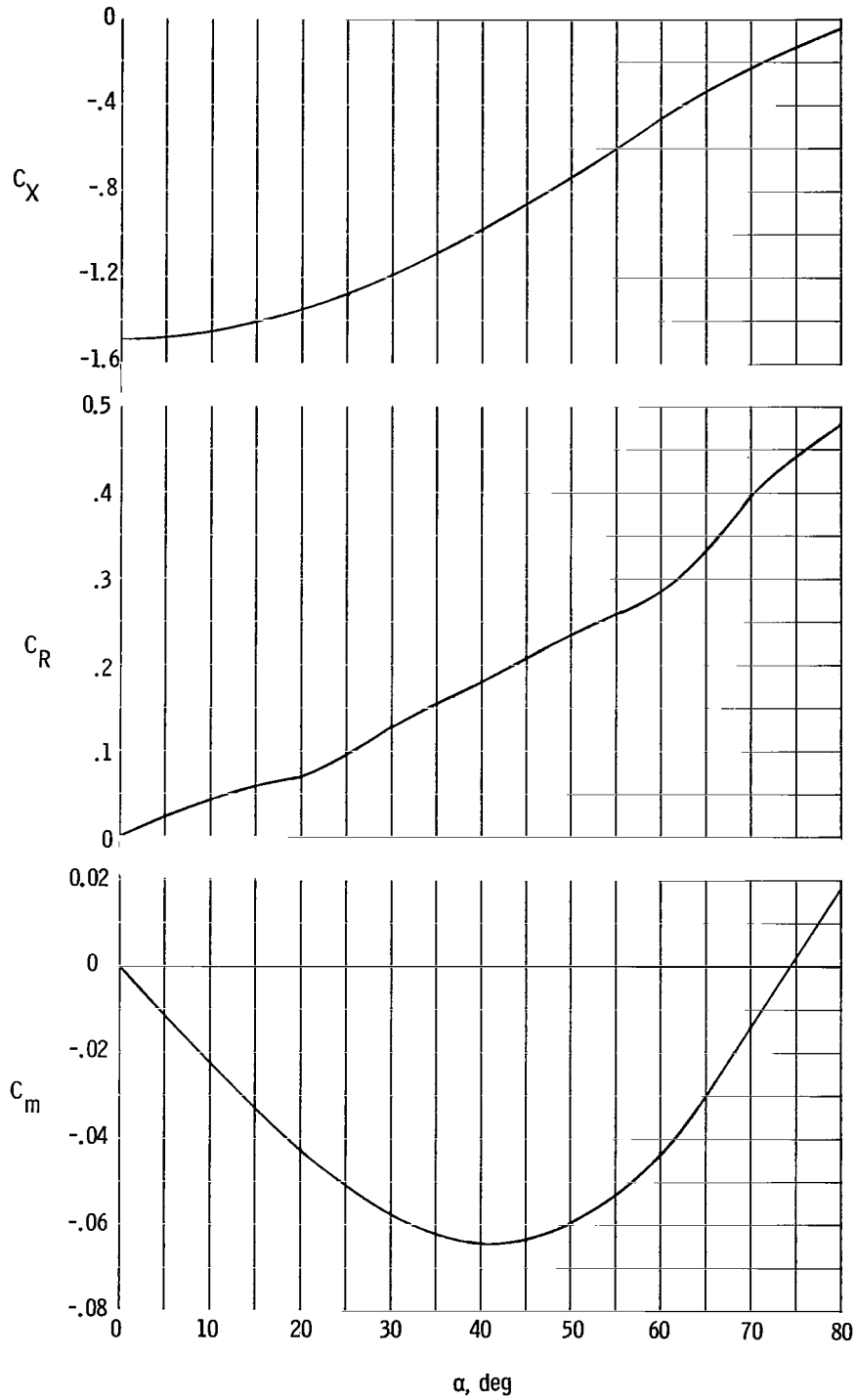
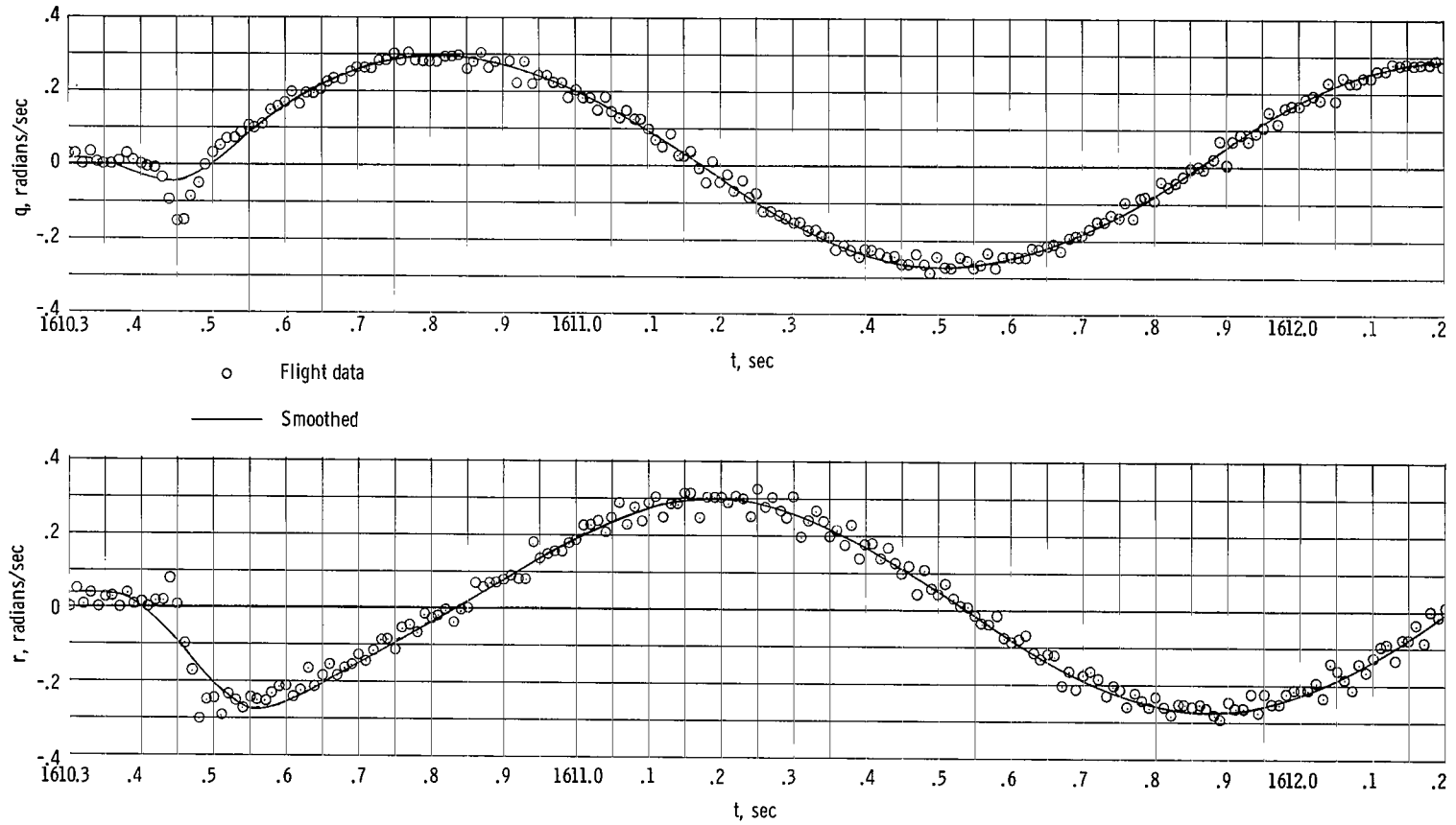
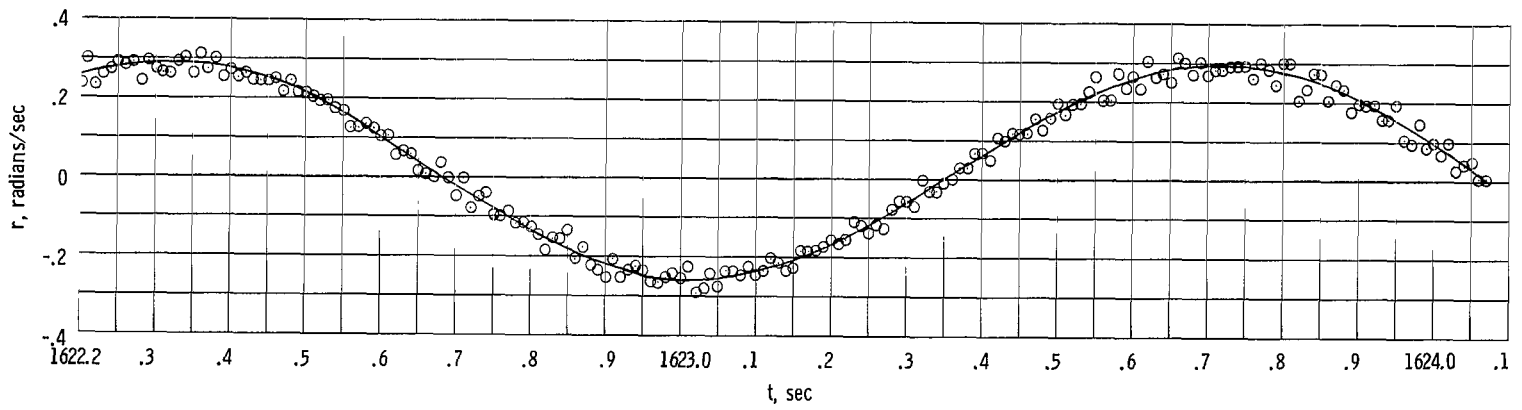
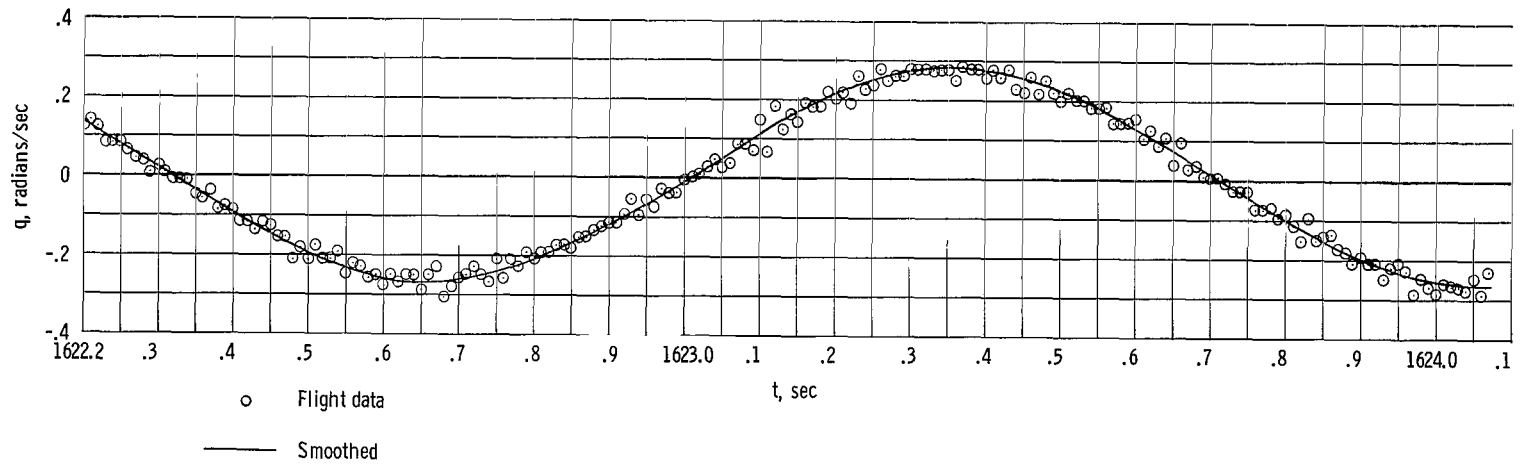


Figure 4.- Static longitudinal aerodynamic data used in the angle-of-attack analysis.



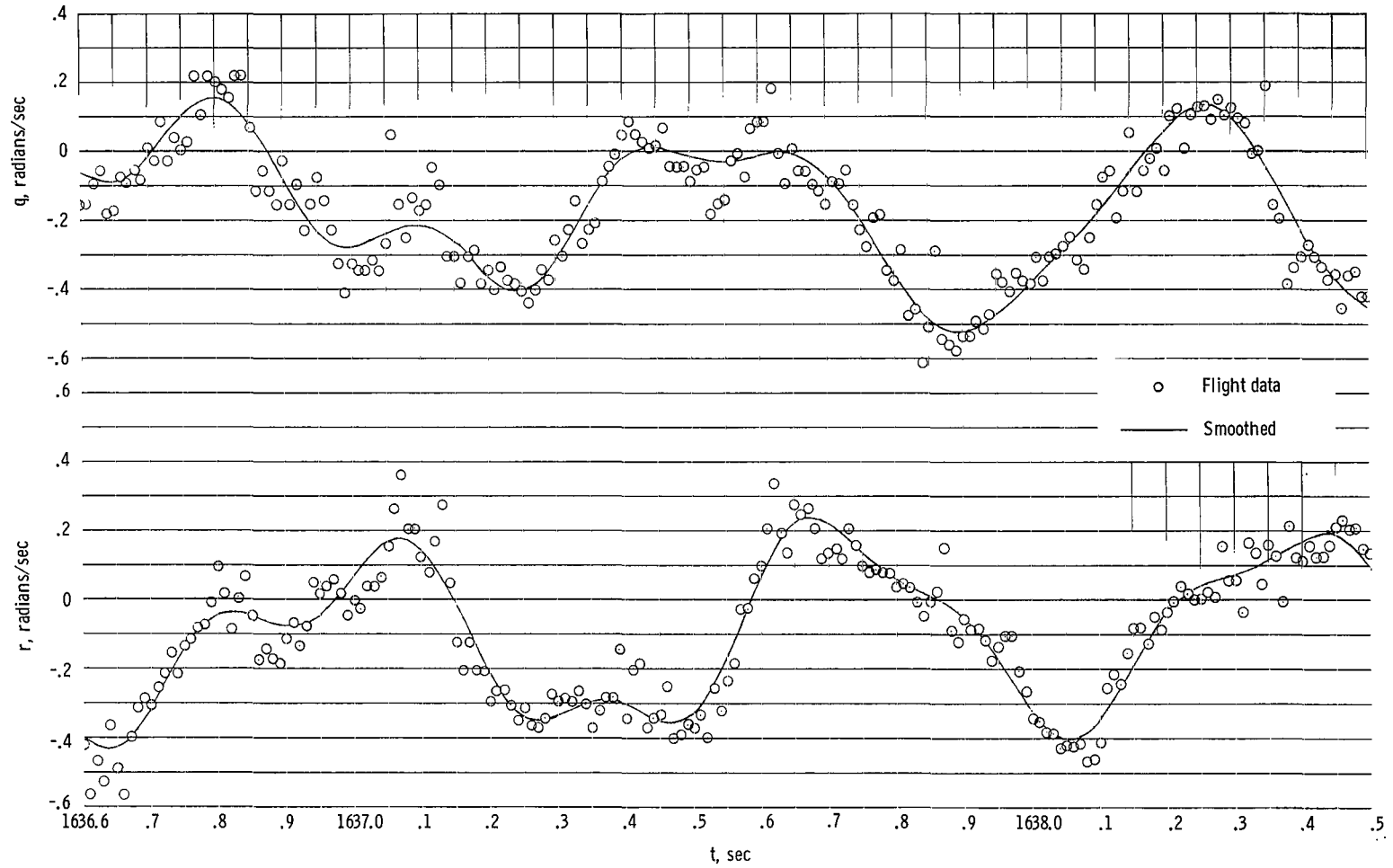
(a) $t = 1610.3$ to 1612.2 seconds.

Figure 5.- Pitch and yaw rates prior to melting of first beryllium calorimeter.



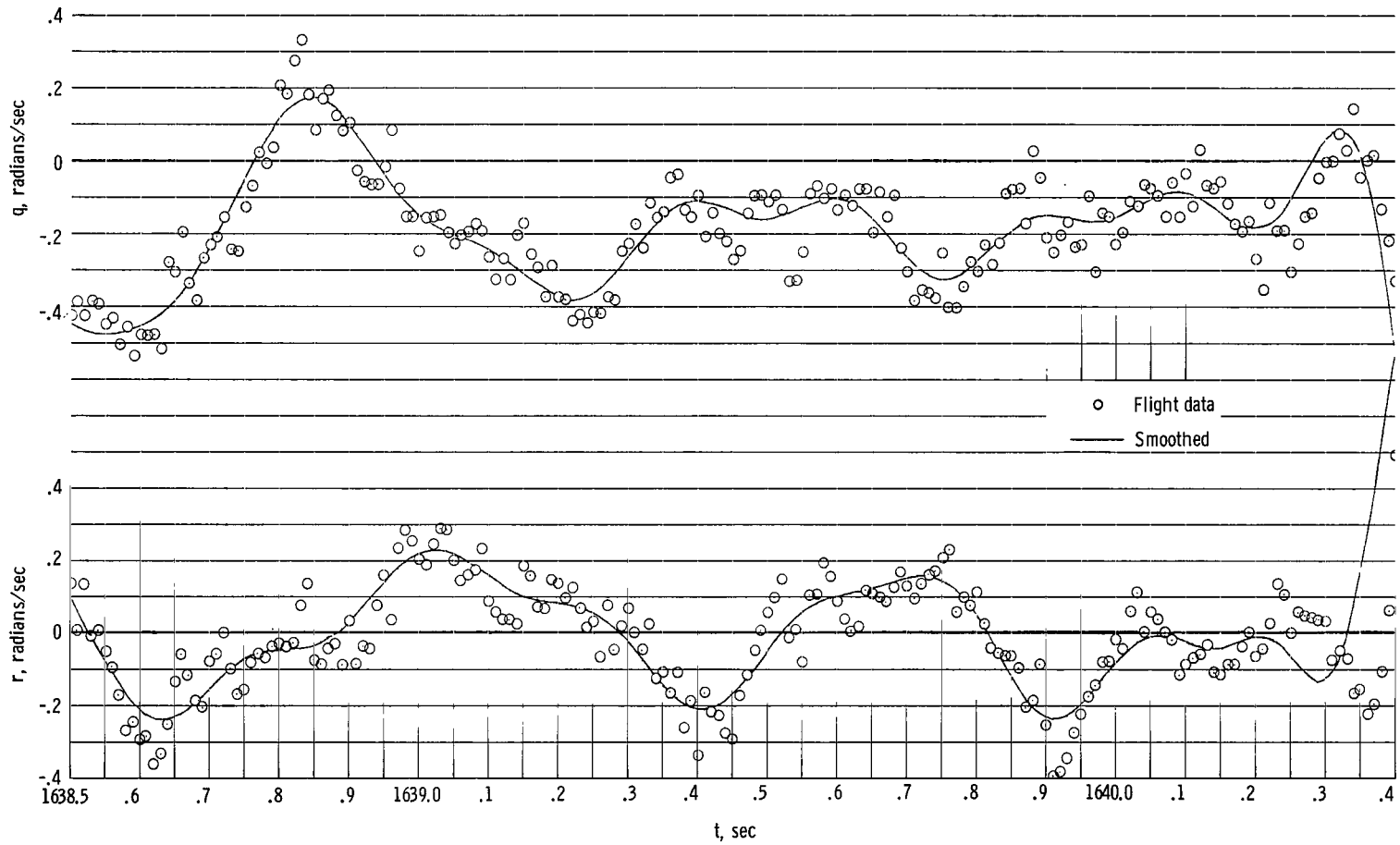
(b) $t = 1622.2$ to 1624.1 seconds.

Figure 5.- Continued.



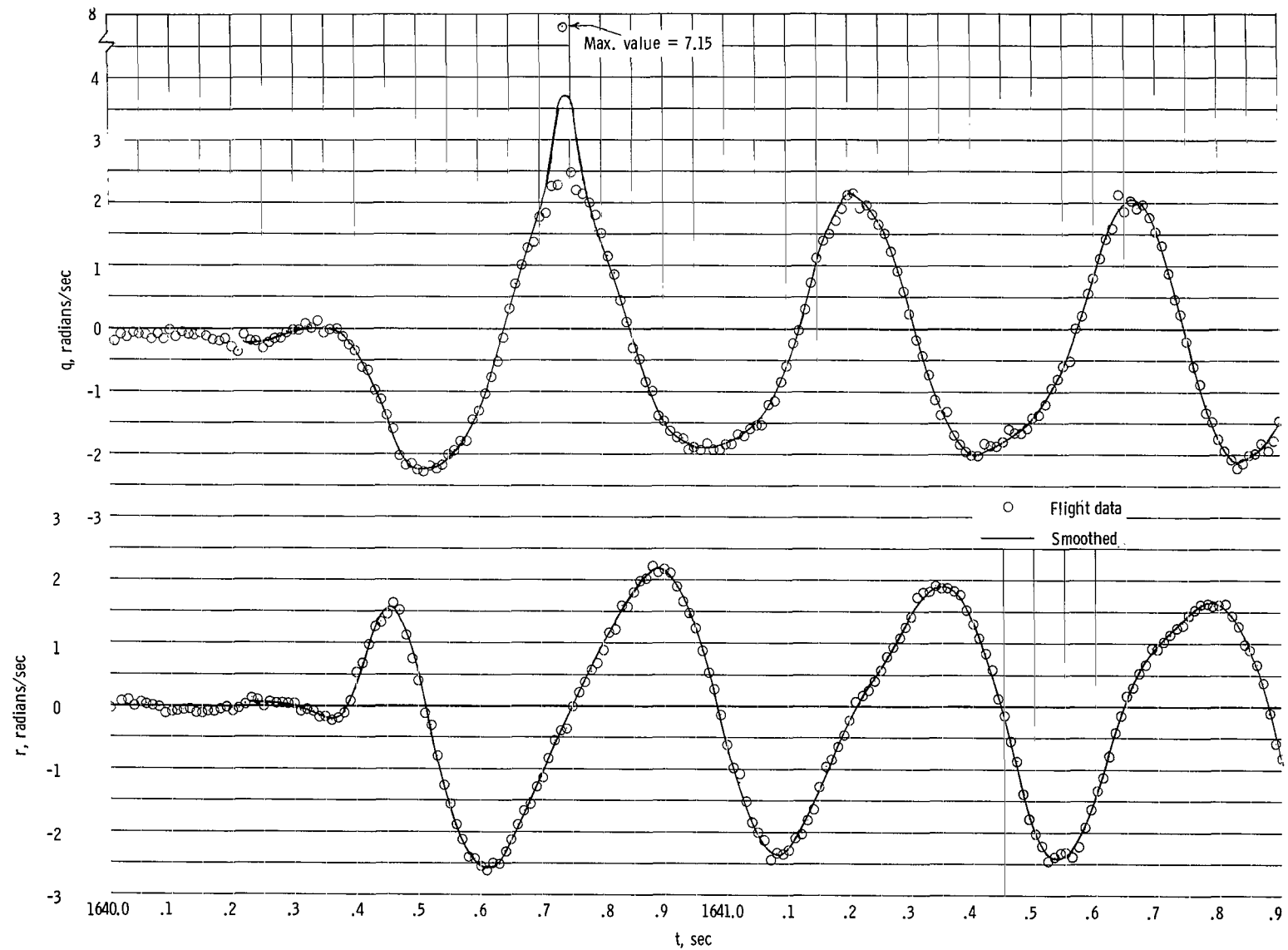
(c) $t = 1636.6$ to 1638.5 seconds.

Figure 5.- Continued.



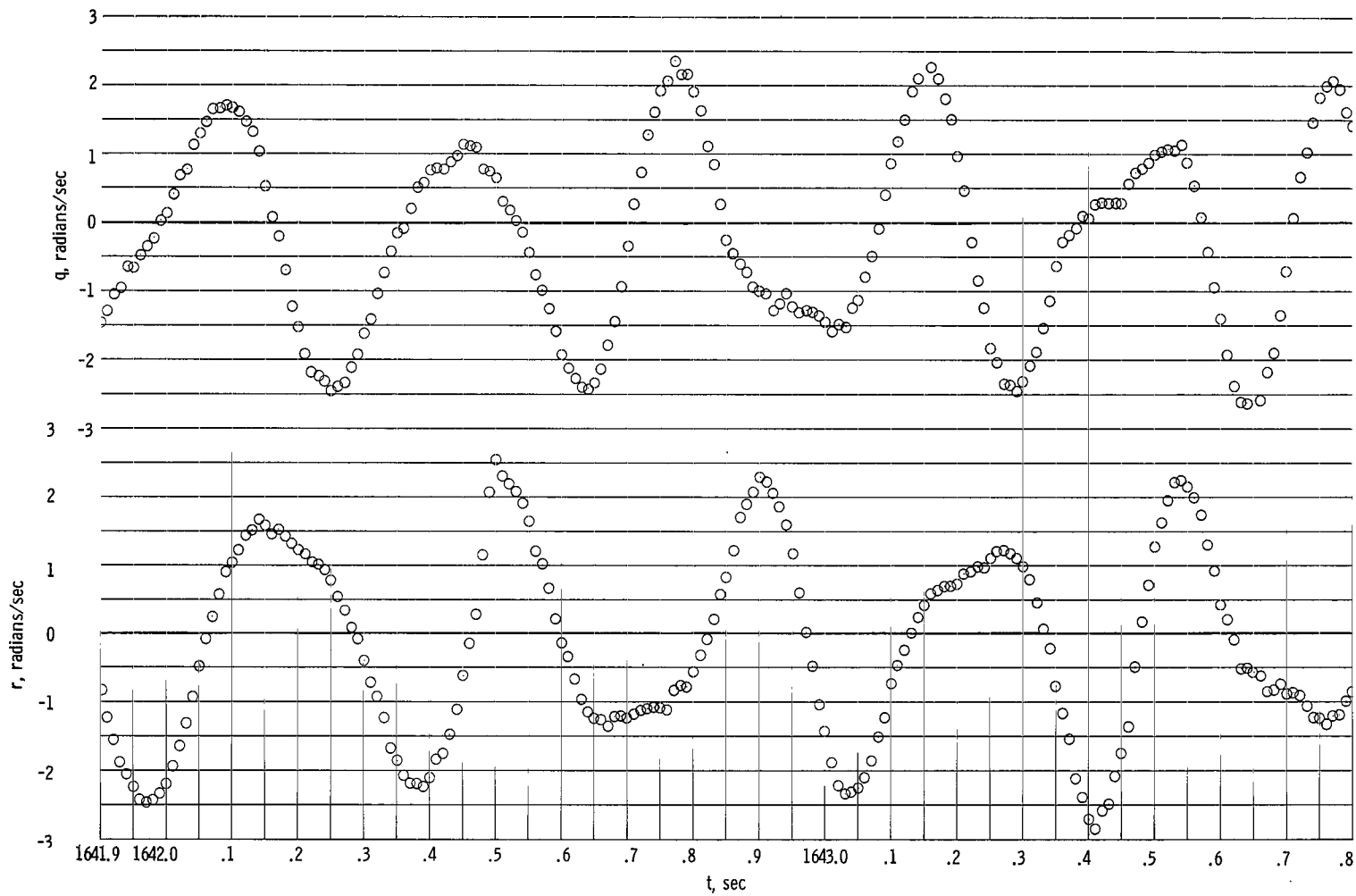
(d) $t = 1638.5$ to 1640.4 seconds.

Figure 5.- Concluded.



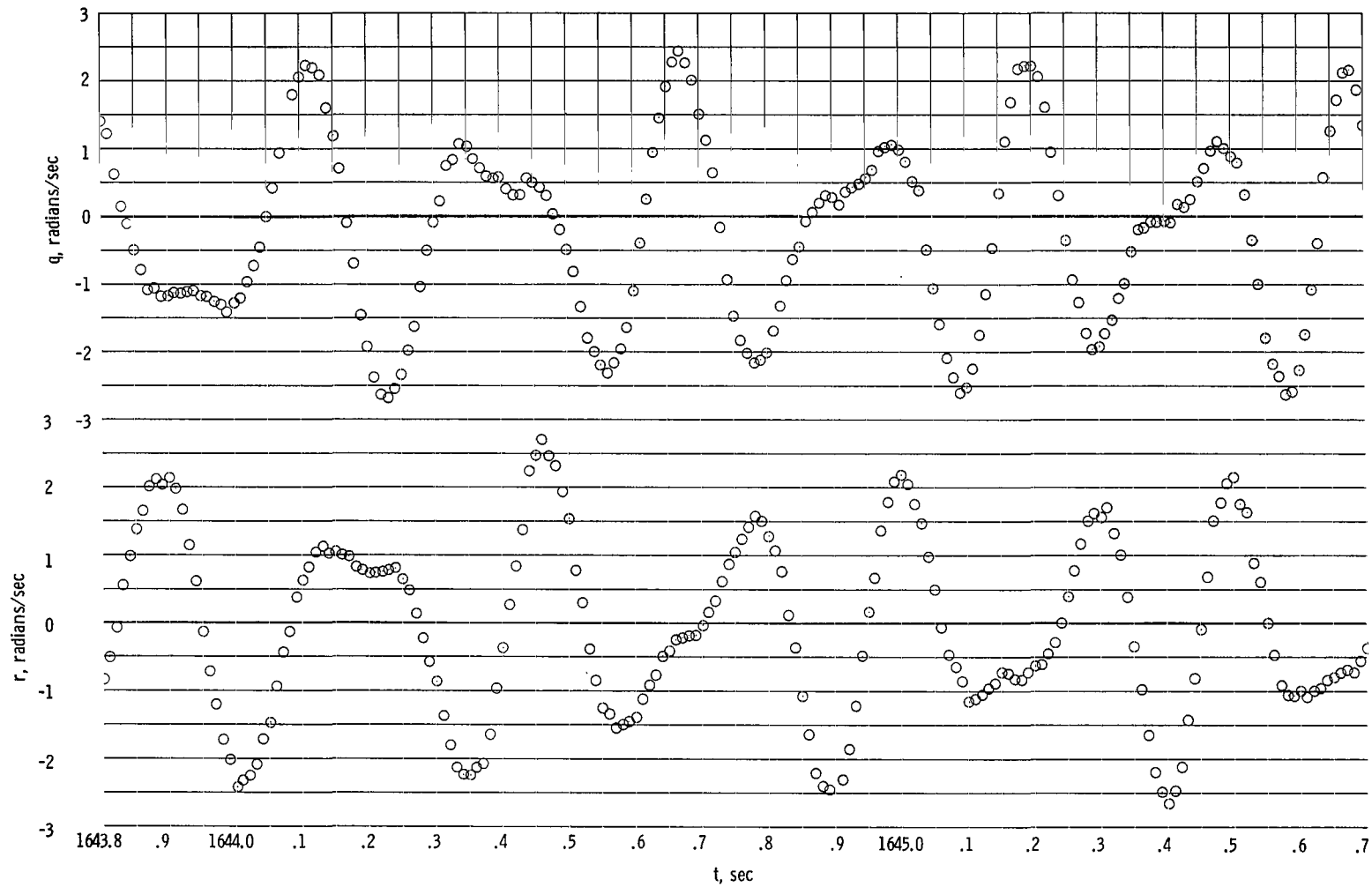
(a) $t = 1640.0$ to 1641.9 seconds.

Figure 6.- Pitch and yaw rates from melting of first beryllium calorimeter to ejection of second phenolic-asbestos heat shield.



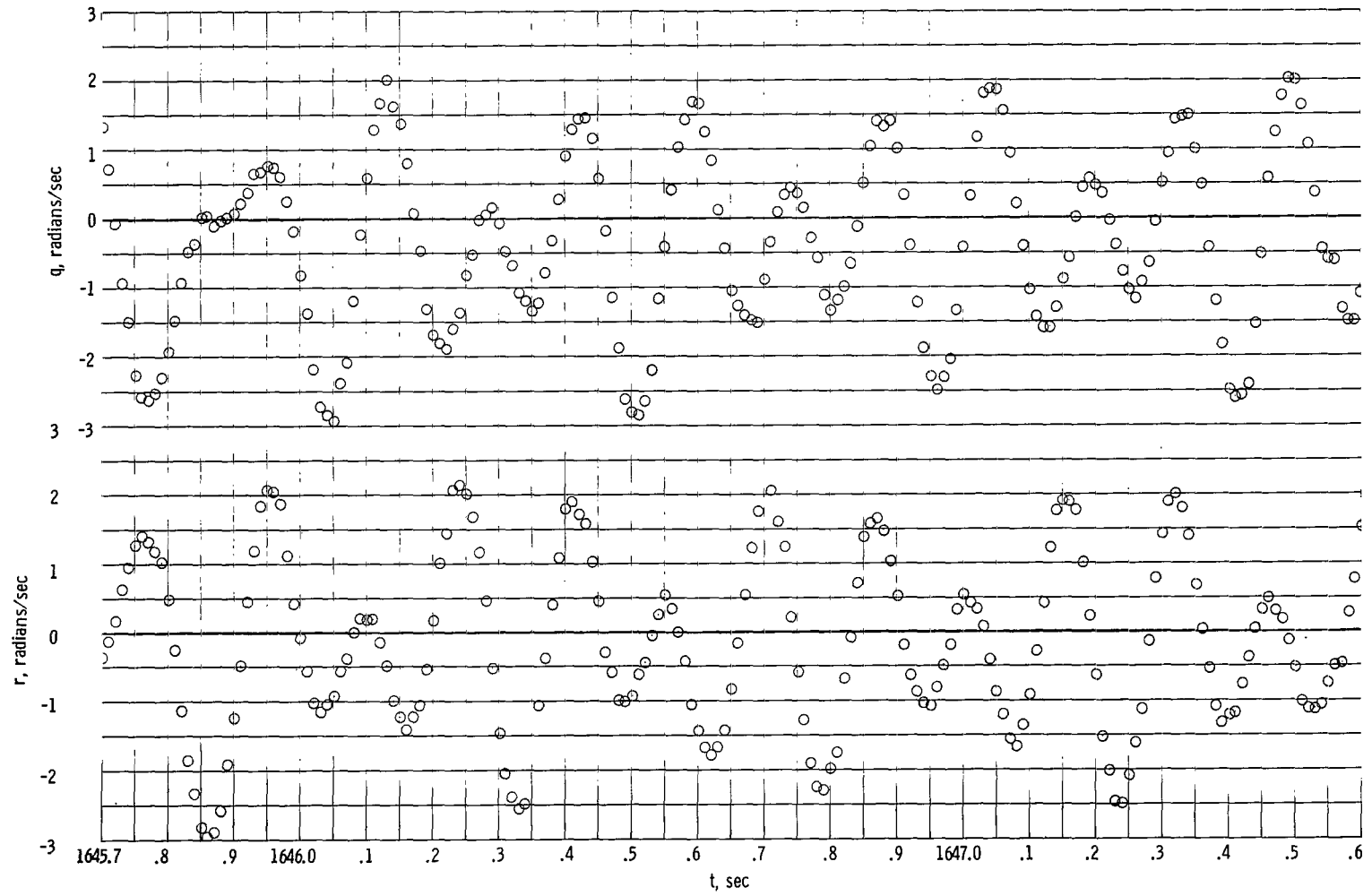
(b) $t = 1641.9$ to 1643.8 seconds.

Figure 6.- Continued.



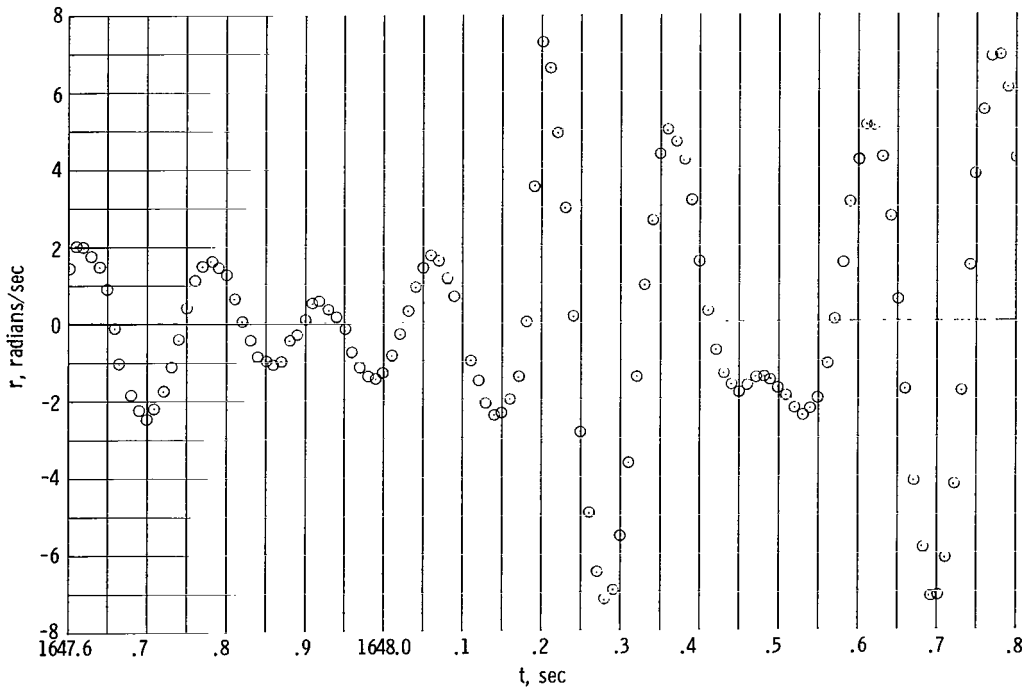
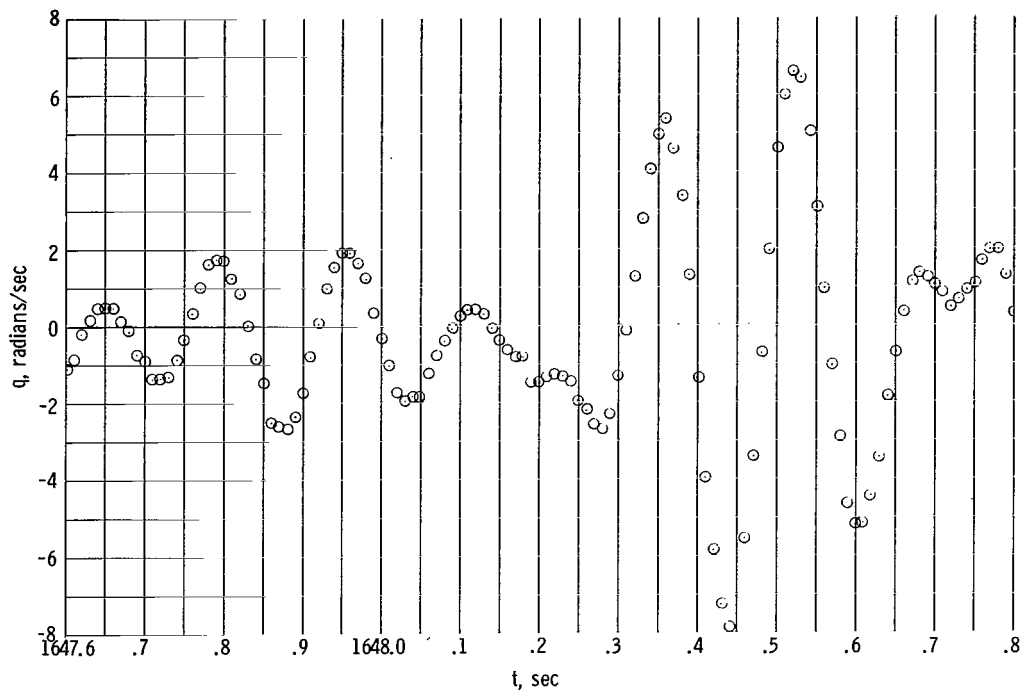
(c) $t = 1643.8$ to 1645.7 seconds.

Figure 6.- Continued.



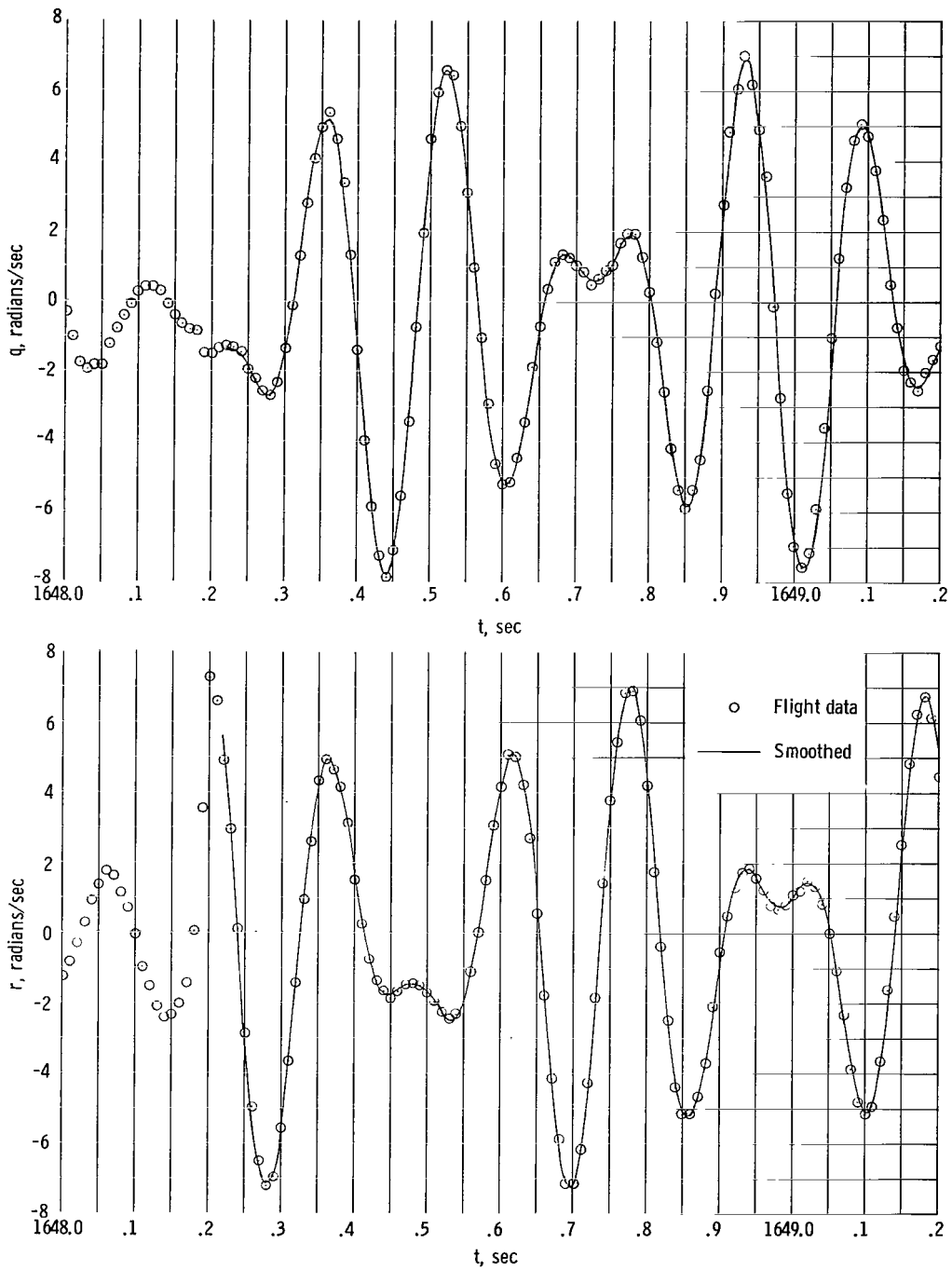
(d) $t = 1645.7$ to 1647.6 seconds.

Figure 6.- Continued.



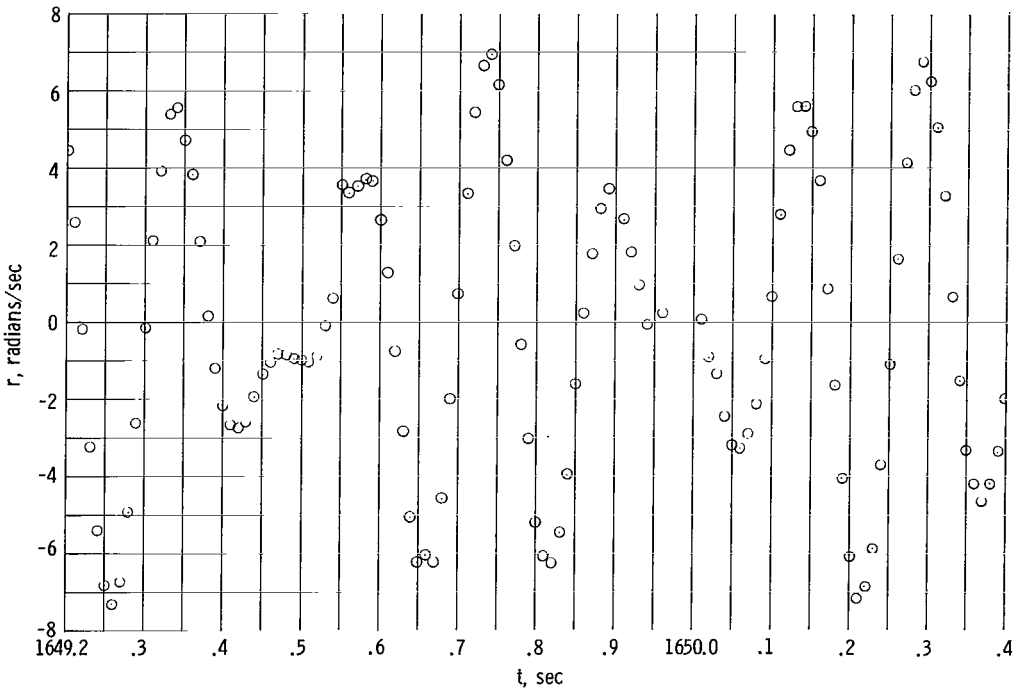
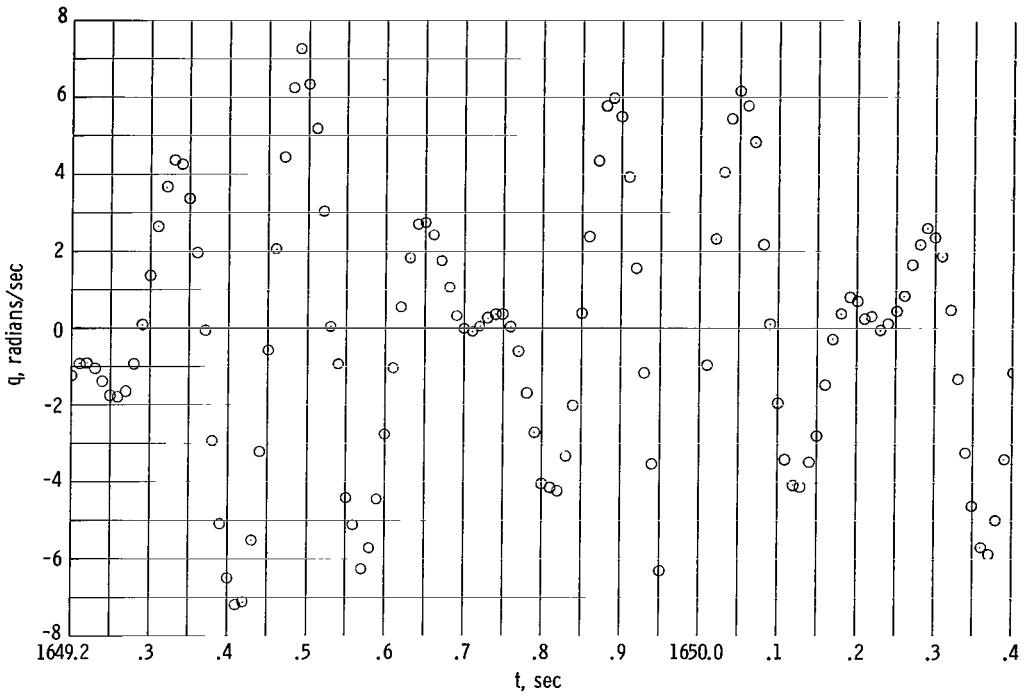
(e) $t = 1647.6$ to 1648.8 seconds.

Figure 6.- Concluded.



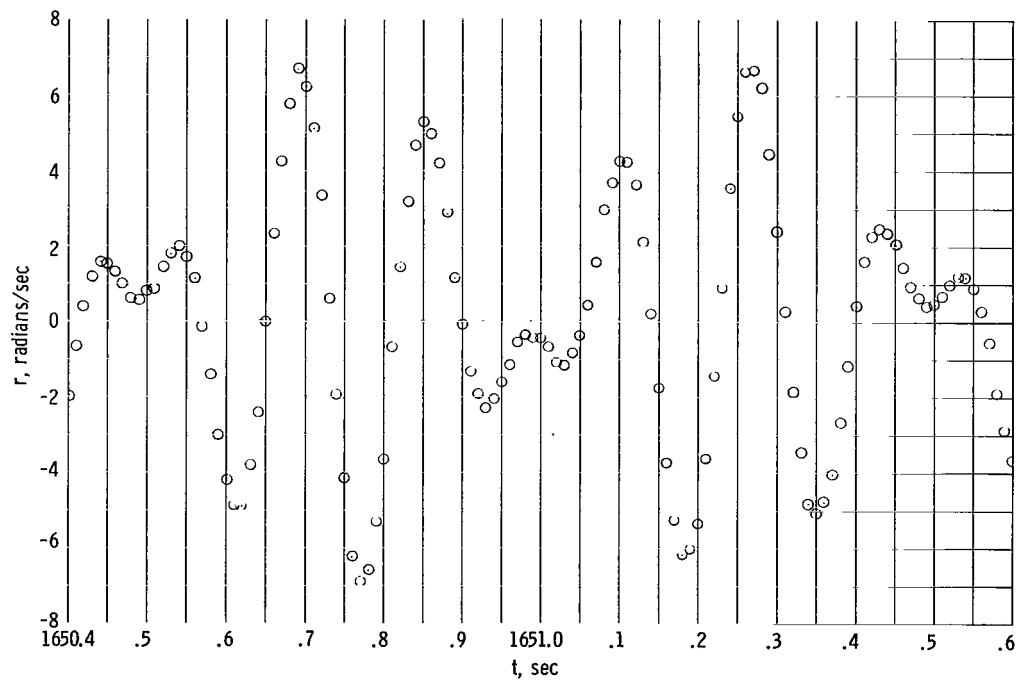
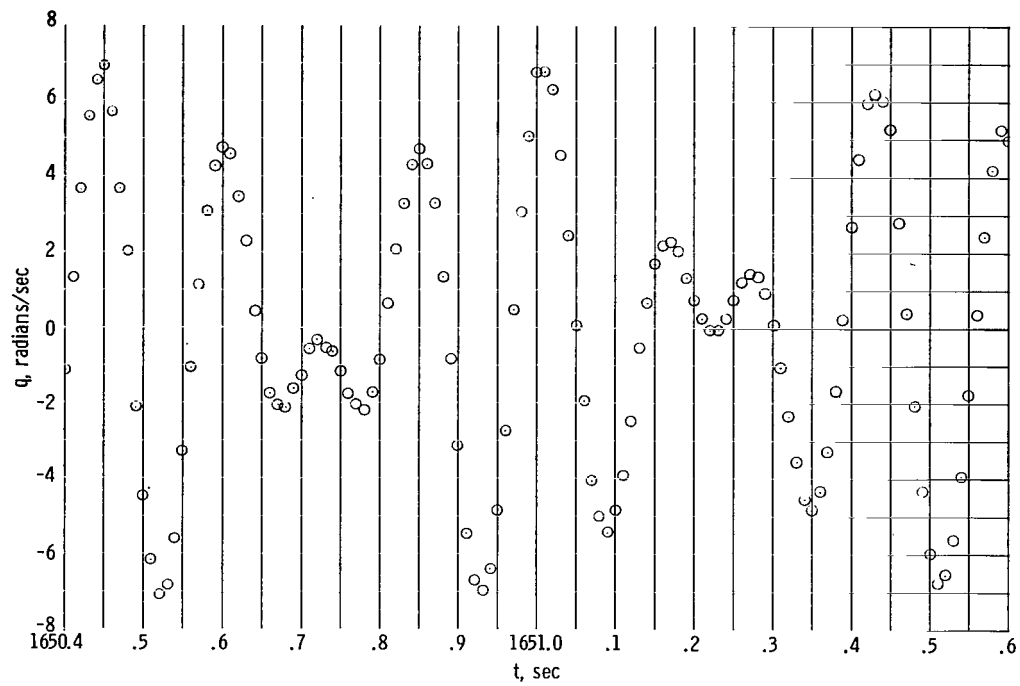
(a) $t = 1648.0$ to 1649.2 seconds.

Figure 7.- Pitch and yaw rates from ejection of the second phenolic-asbestos heat shield to $t = 1666$ seconds.



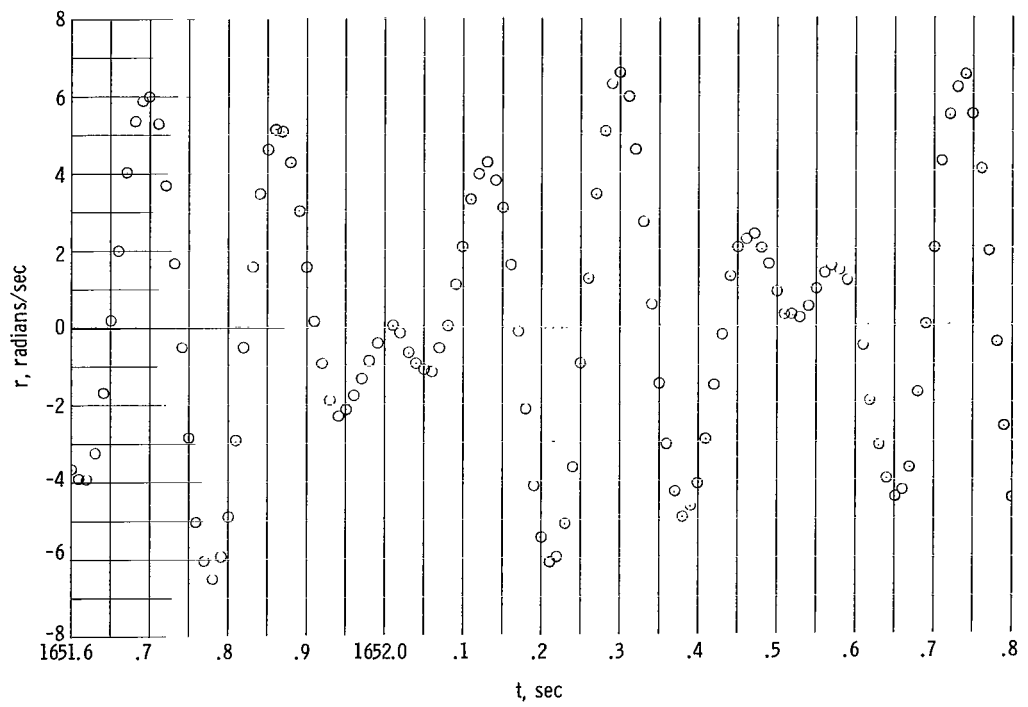
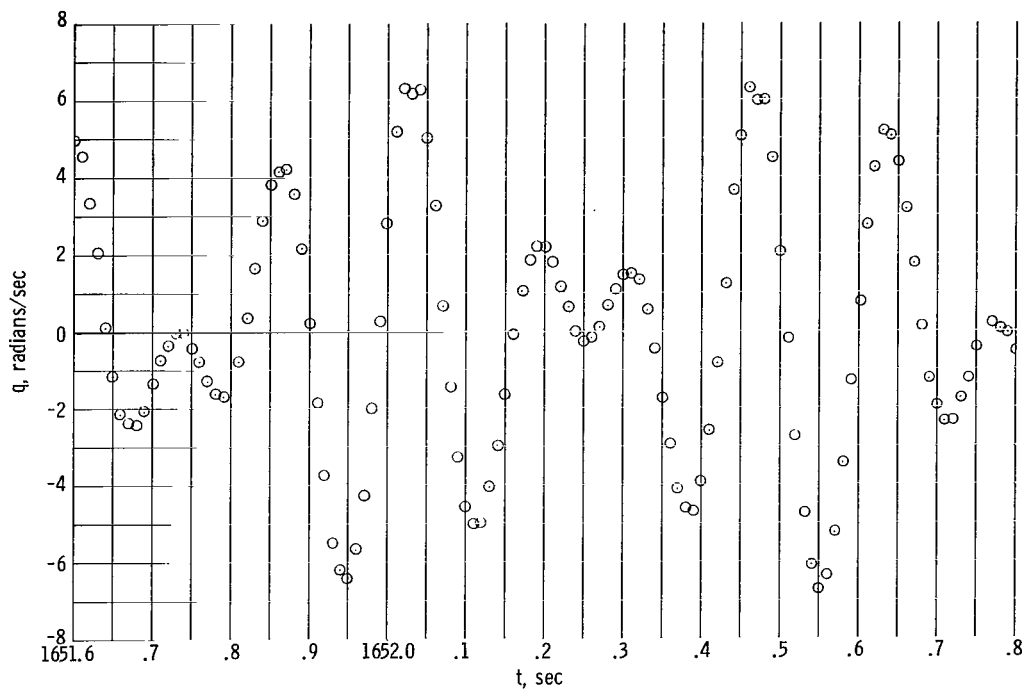
(b) $t = 1649.2$ to 1650.4 seconds.

Figure 7.- Continued.



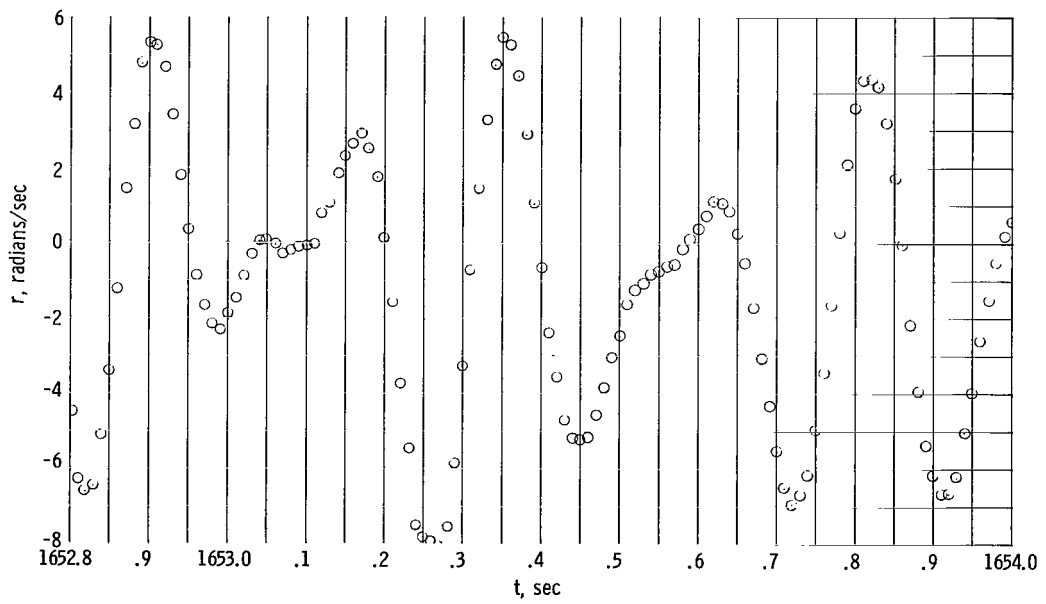
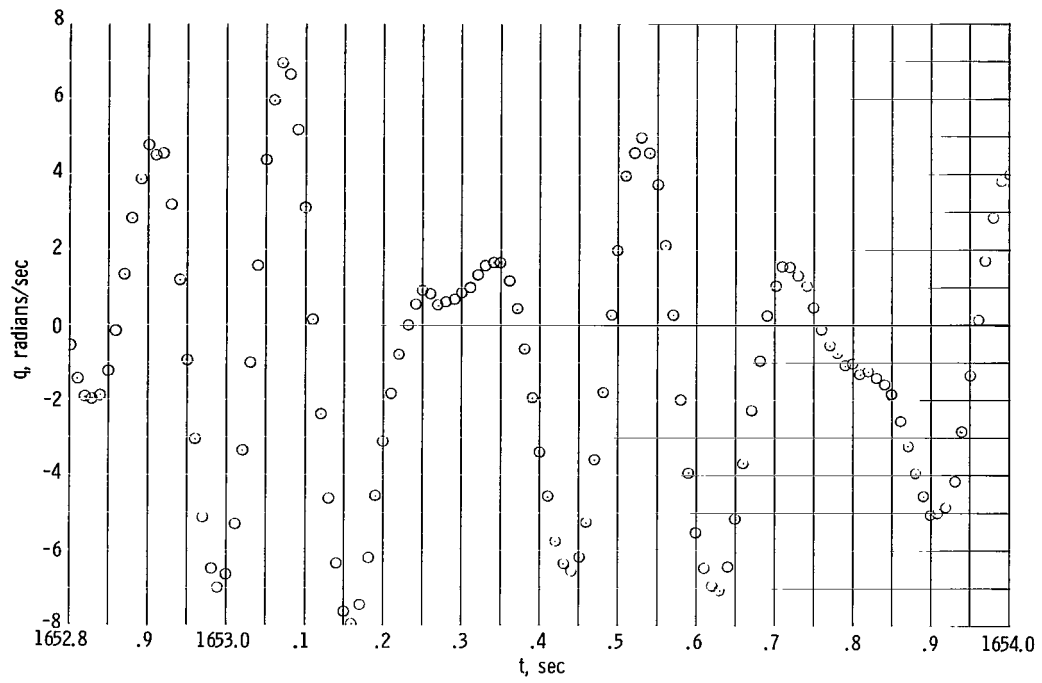
(c) $t = 1650.4$ to 1651.6 seconds.

Figure 7.- Continued.



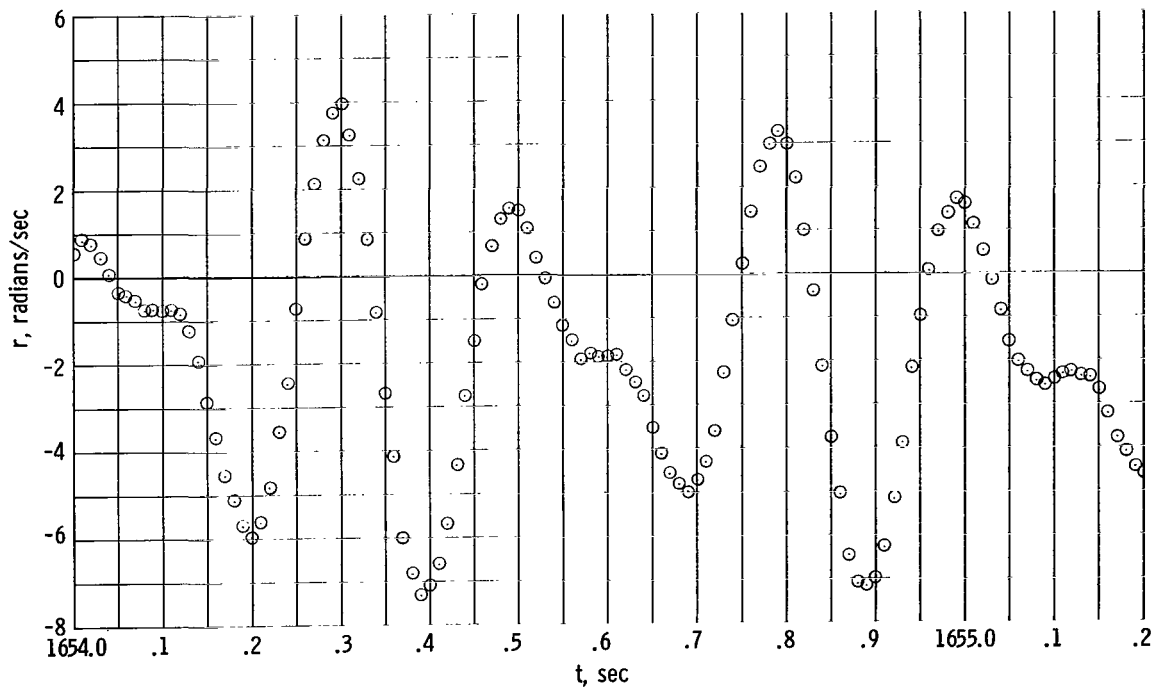
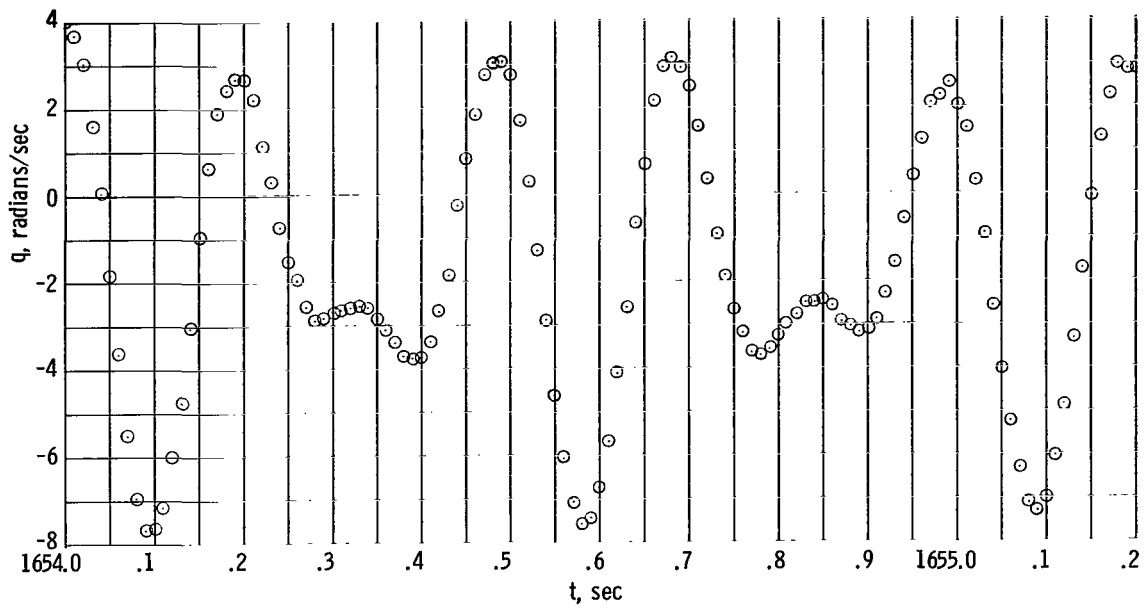
(d) $t = 1651.6$ to 1652.8 seconds.

Figure 7.- Continued.



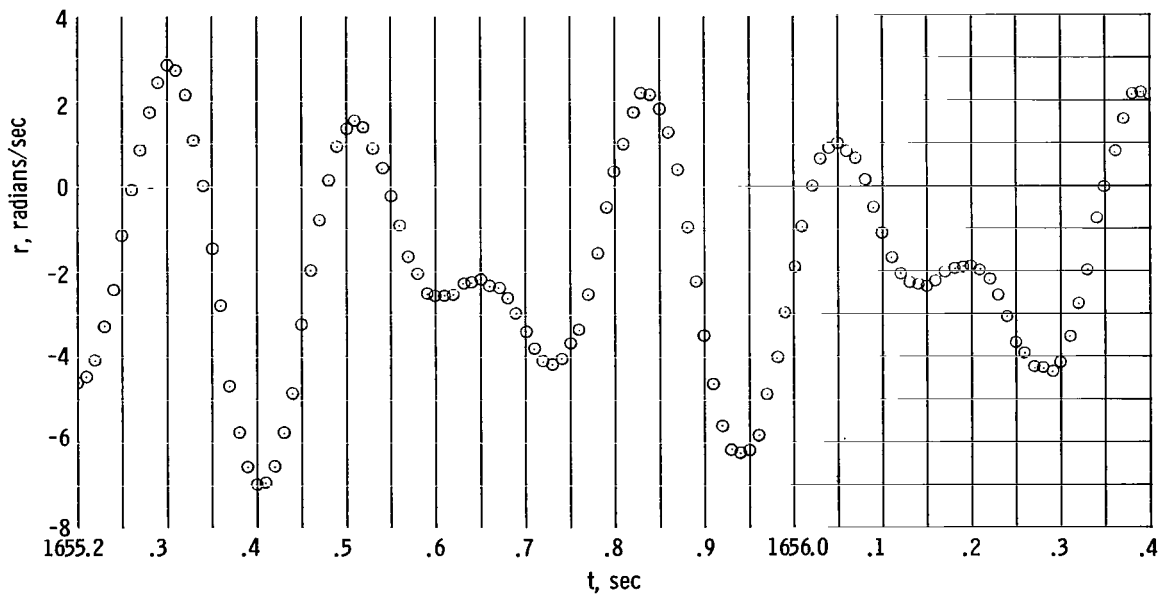
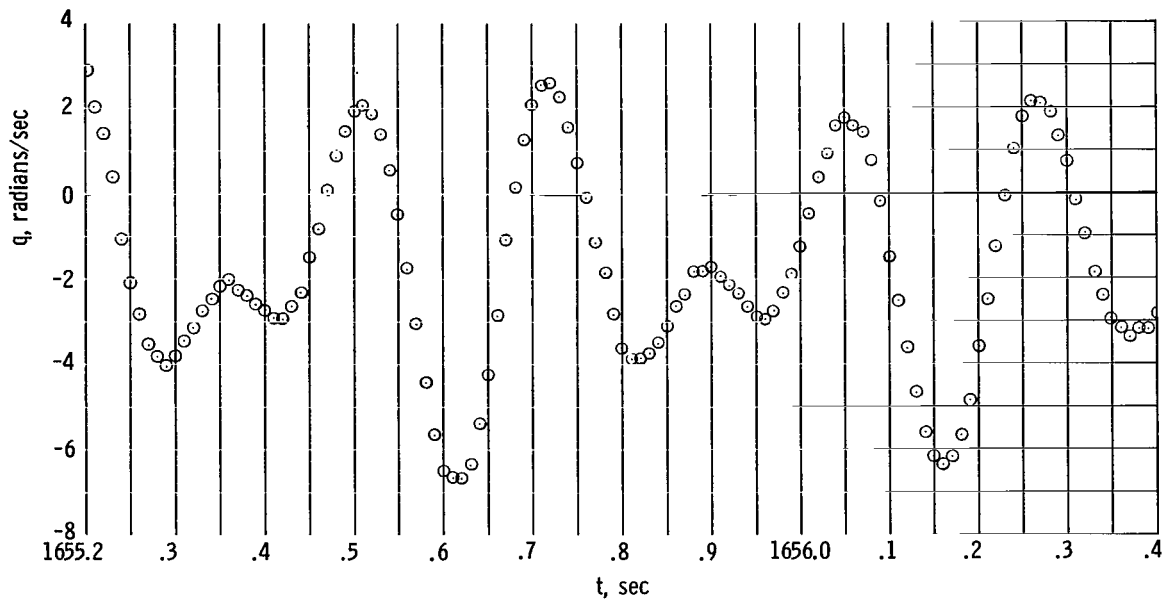
(e) $t = 1652.8$ to 1654.0 seconds.

Figure 7.- Continued.



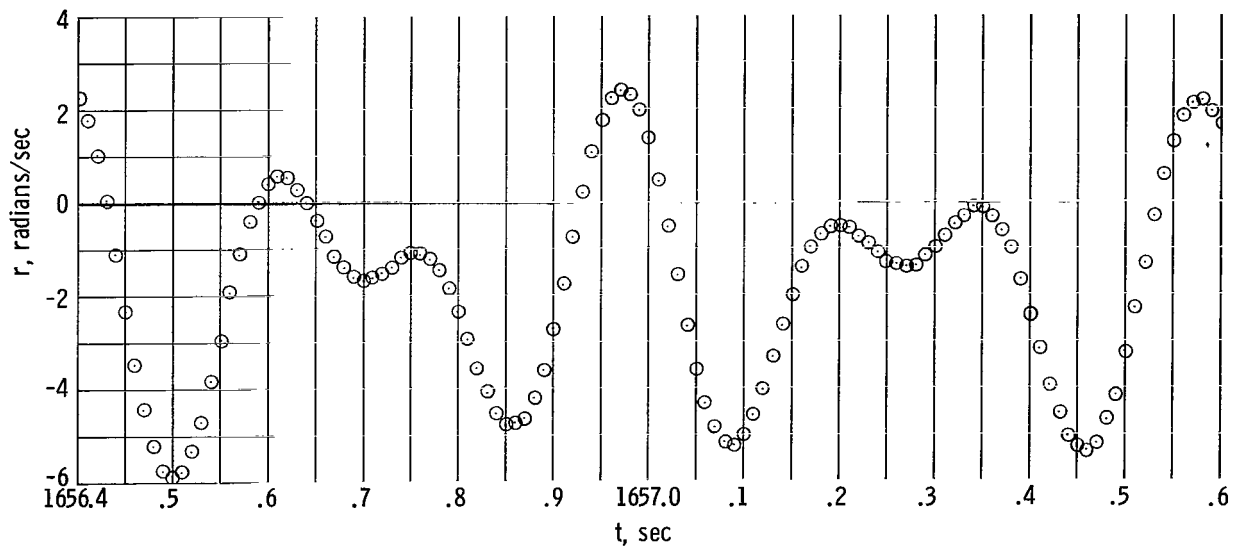
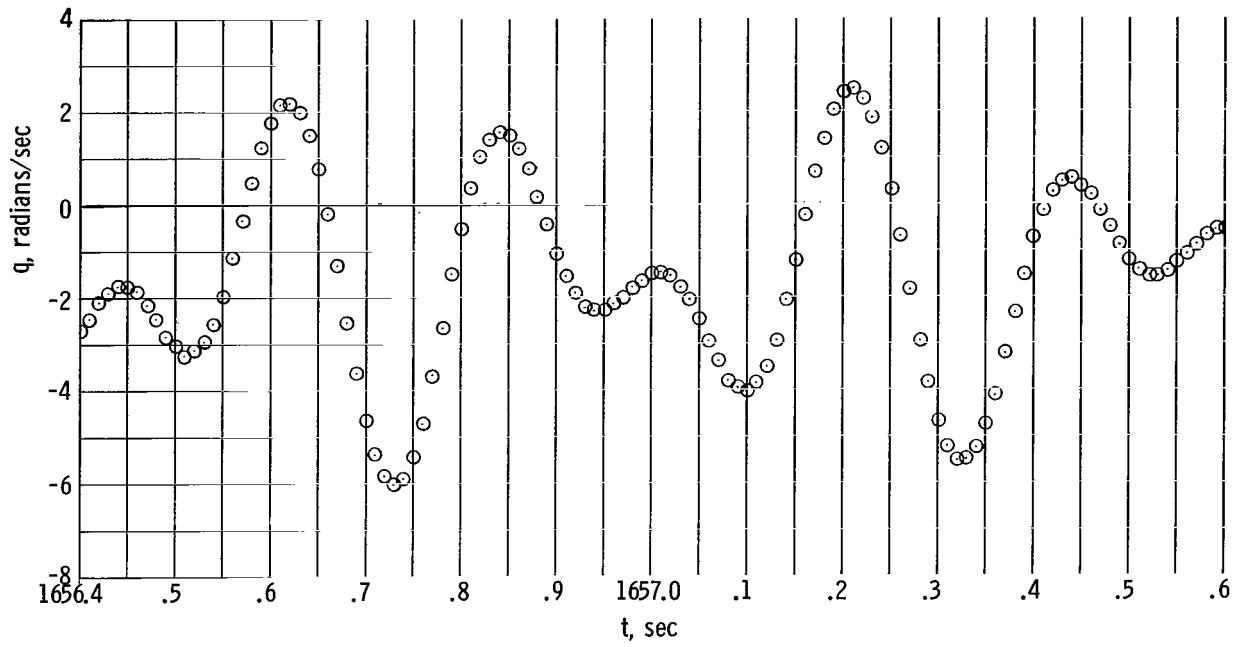
(f) $t = 1654.0$ to 1655.2 seconds.

Figure 7.- Continued.



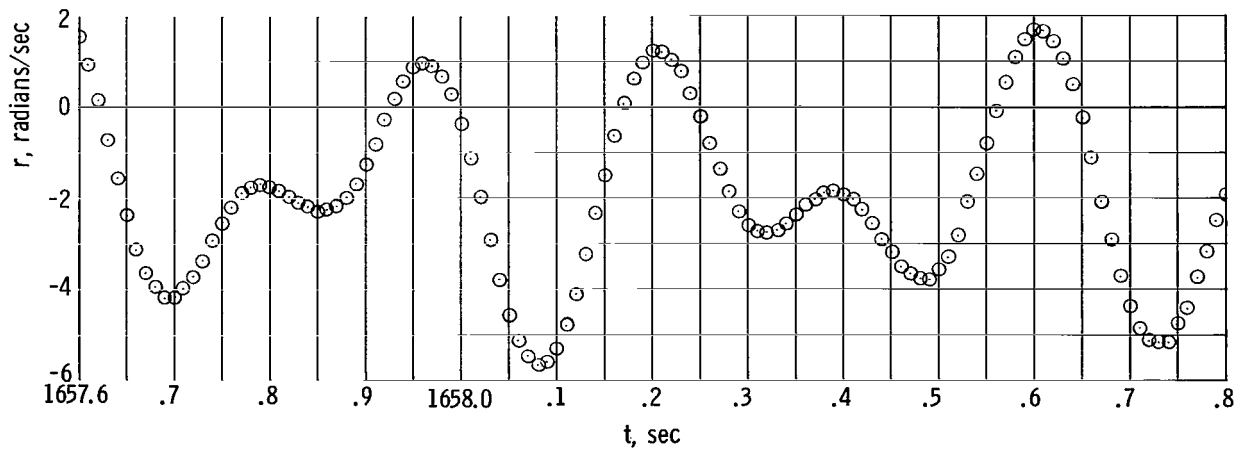
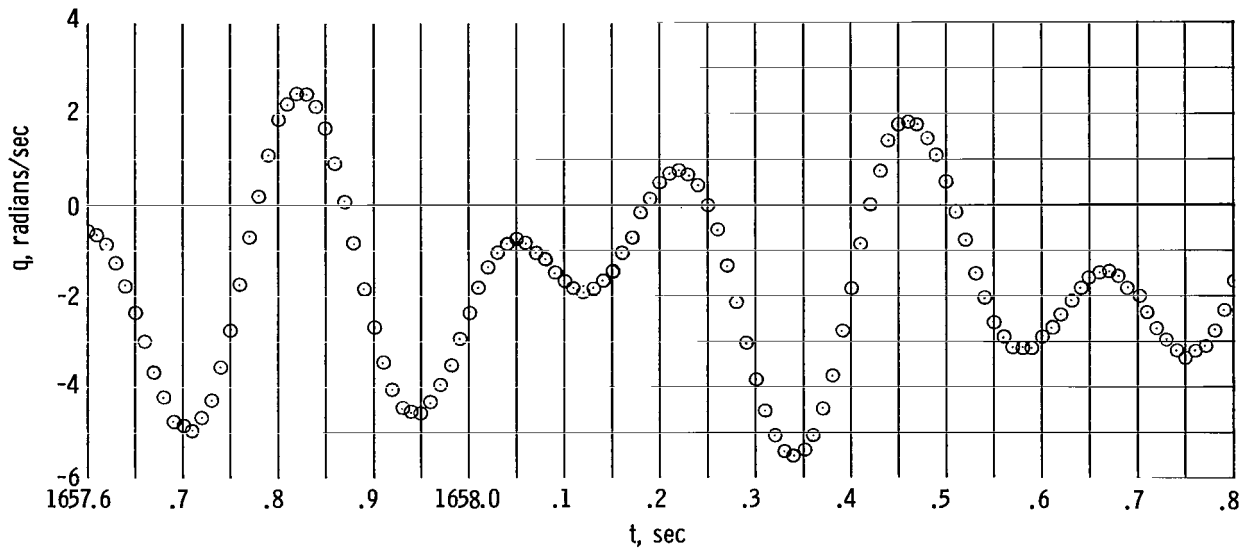
(g) $t = 1655.2$ to 1656.4 seconds.

Figure 7.- Continued.



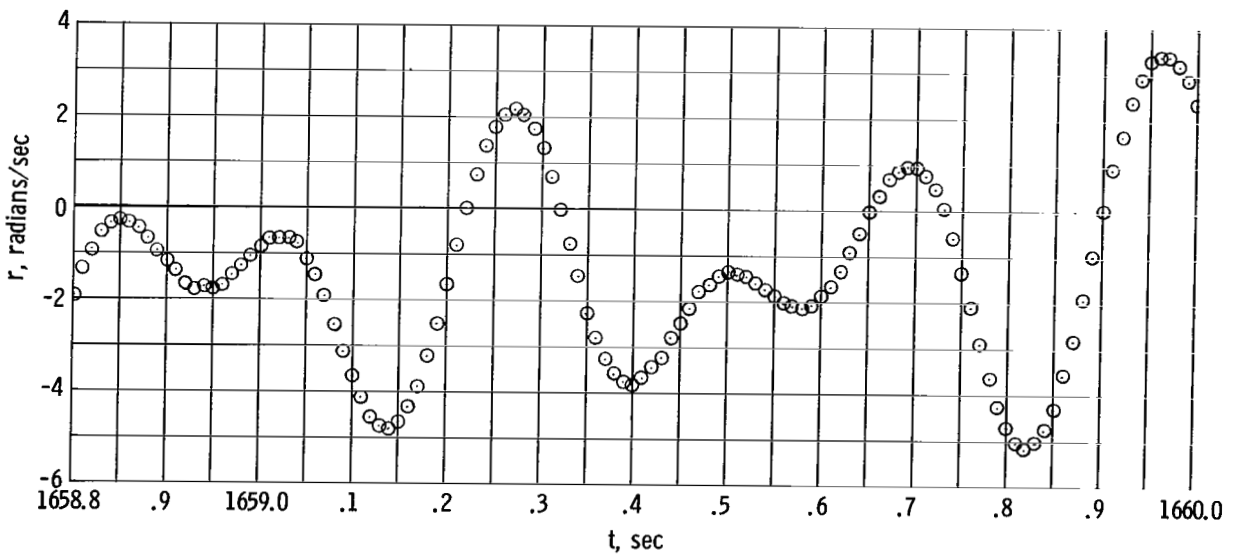
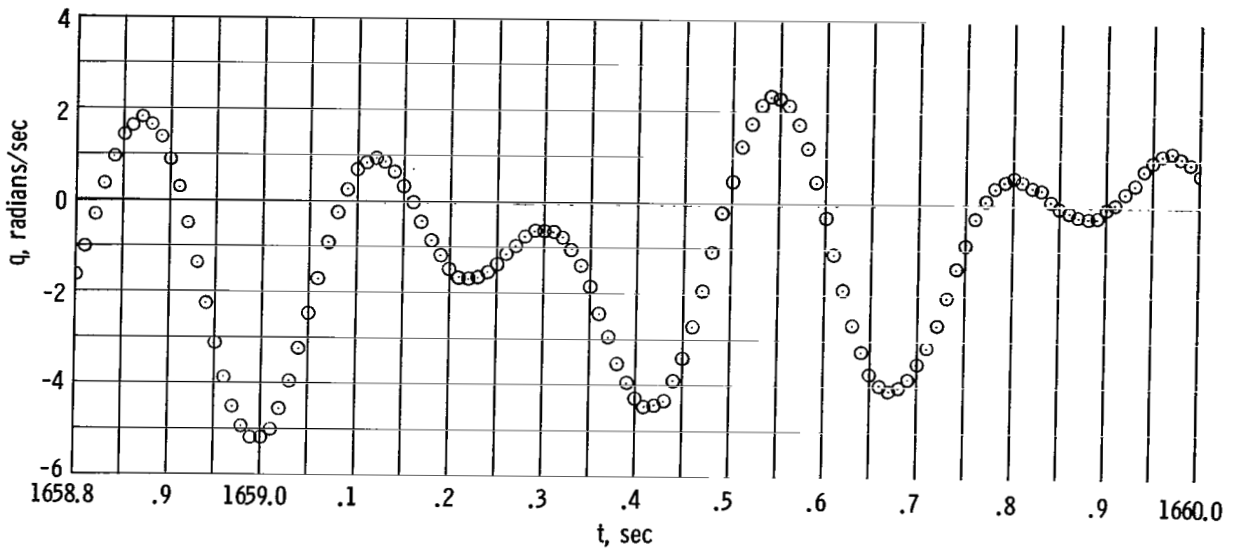
(h) $t = 1656.4$ to 1657.6 seconds.

Figure 7.- Continued.



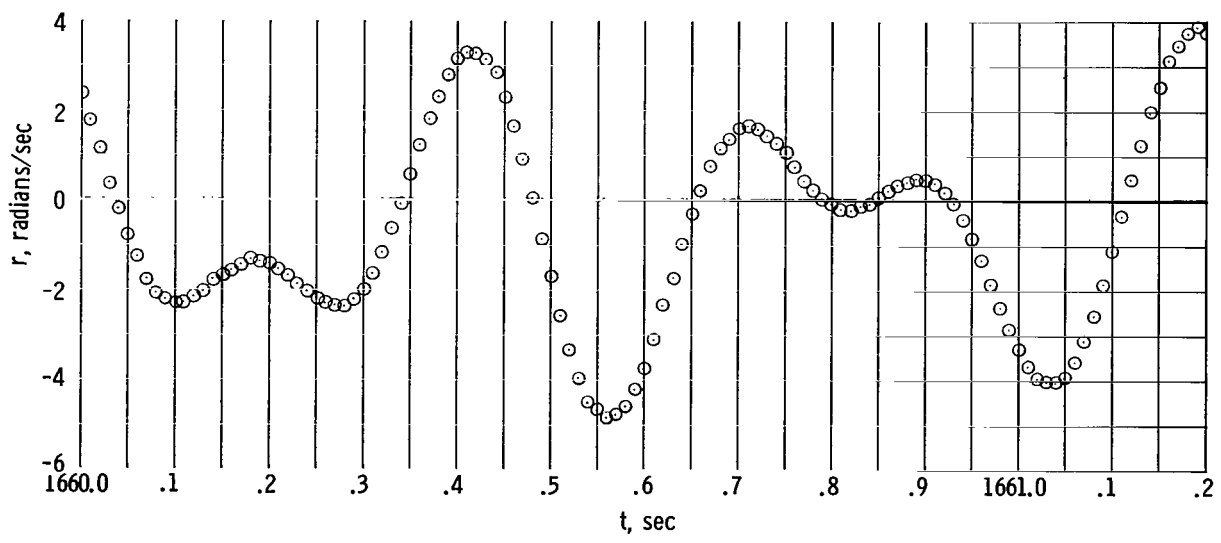
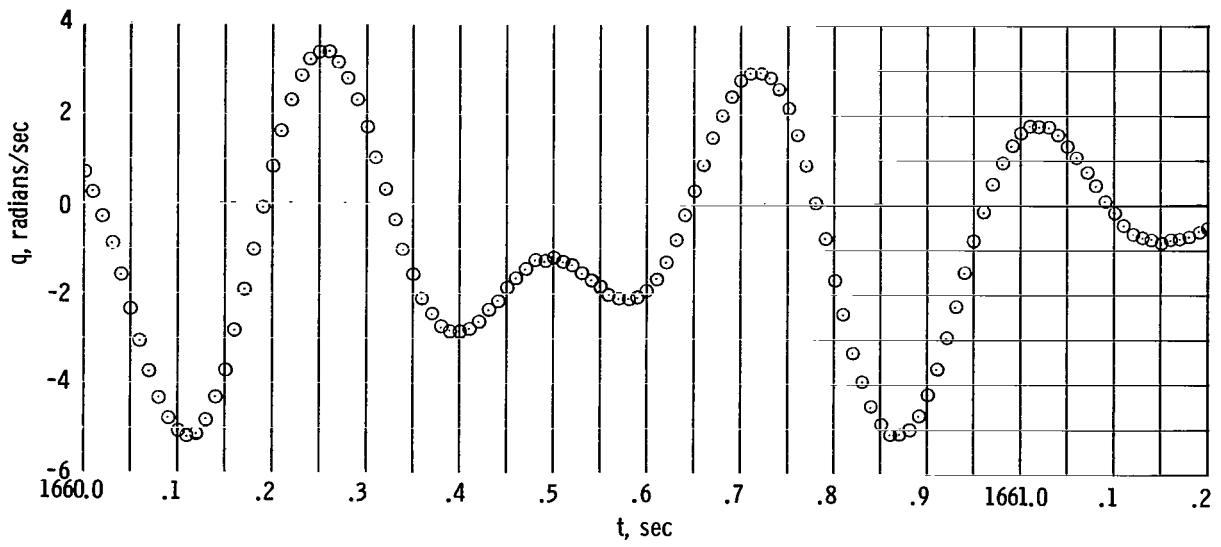
(i) $t = 1657.6$ to 1658.8 seconds.

Figure 7.- Continued.



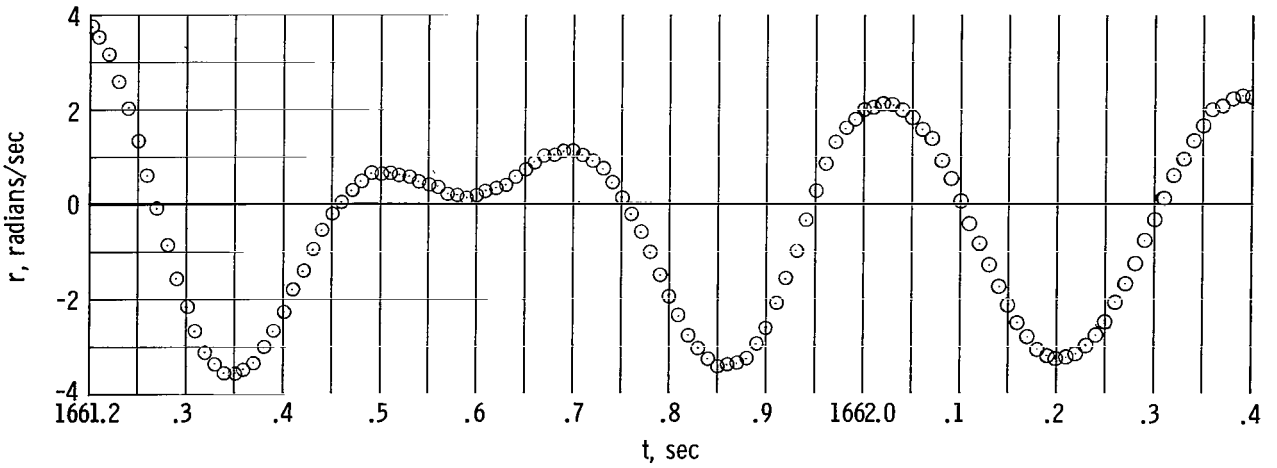
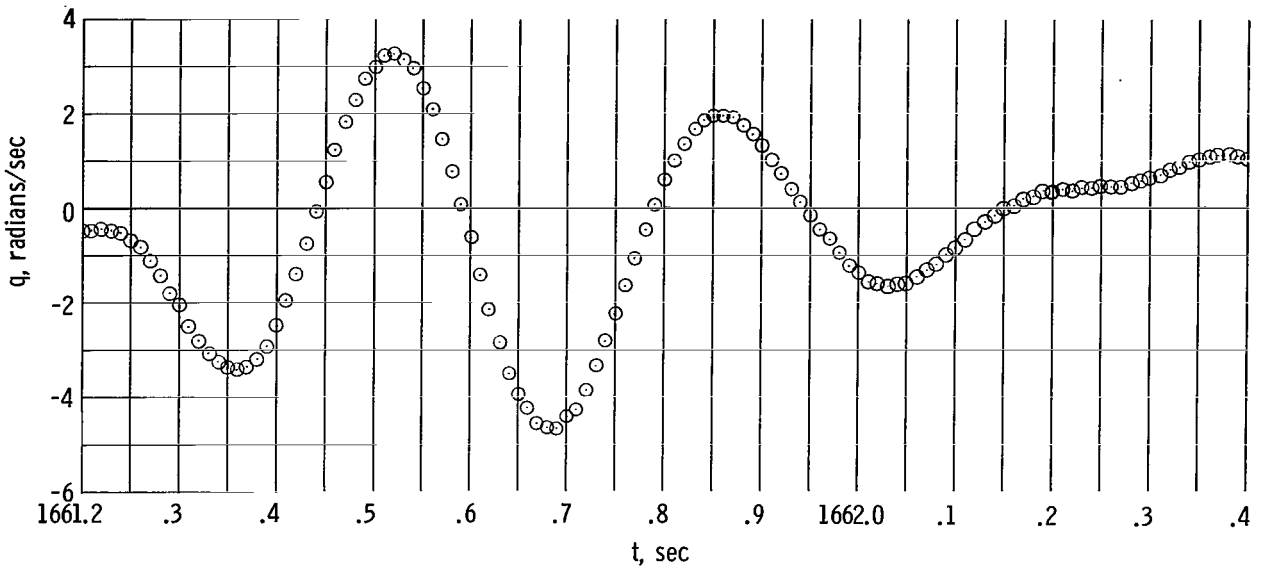
(j) $t = 1658.8$ to 1660.0 seconds.

Figure 7.- Continued.



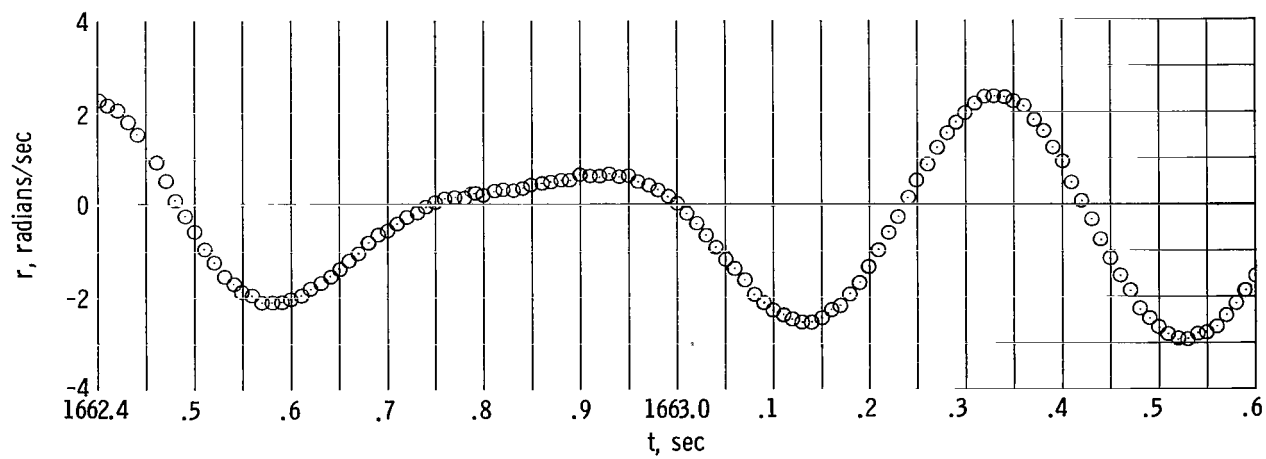
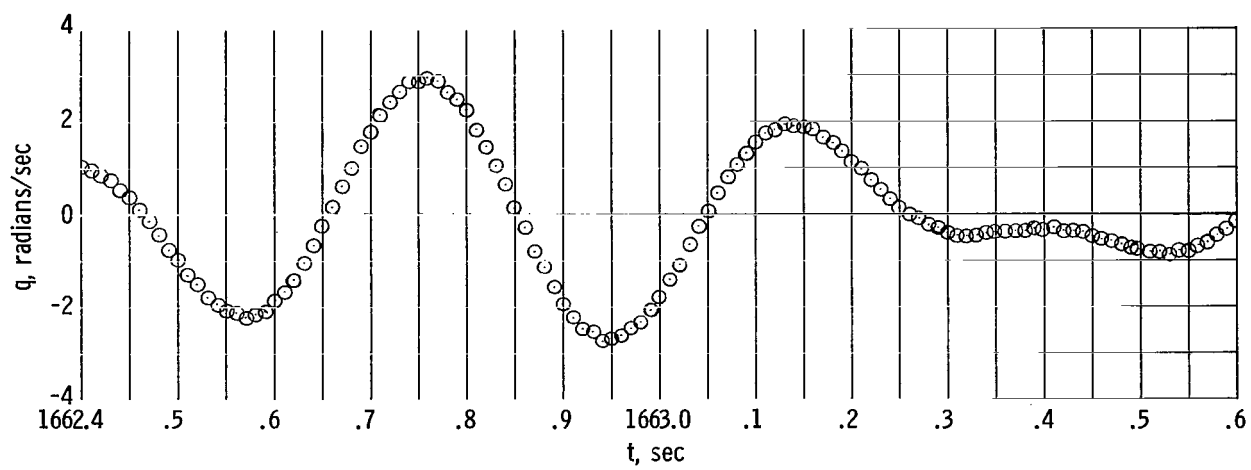
(k) $t = 1660.0$ to 1661.2 seconds.

Figure 7.- Continued.



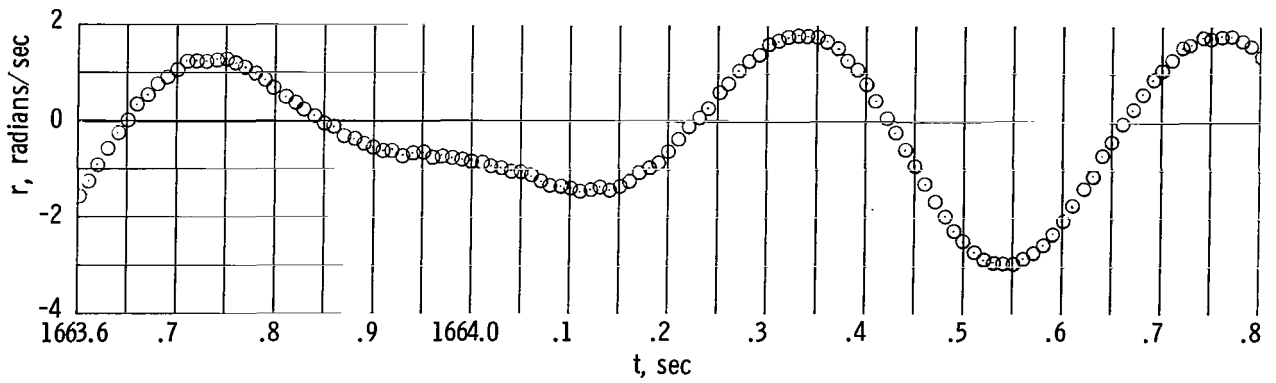
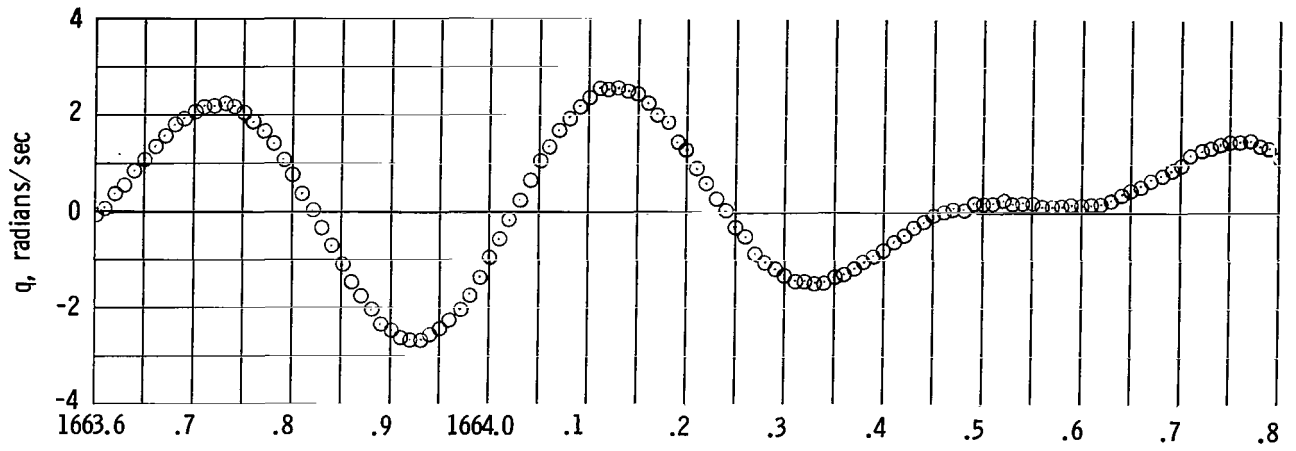
(I) $t = 1661.2$ to 1662.4 seconds.

Figure 7.- Continued.



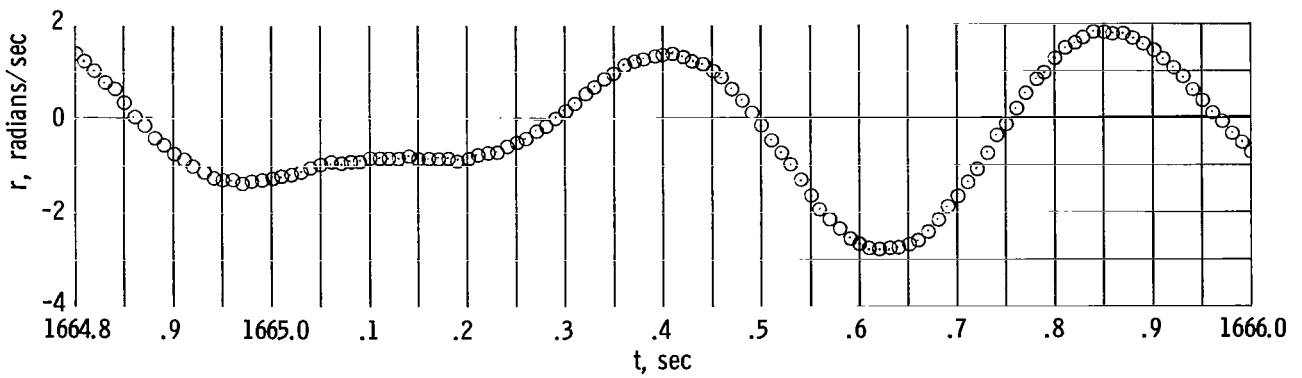
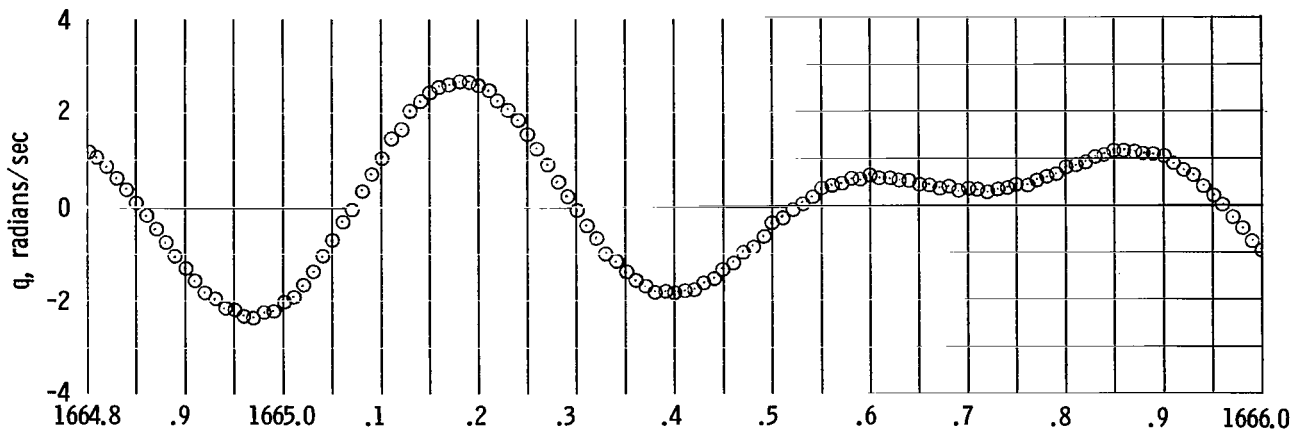
(m) $t = 1662.4$ to 1663.6 seconds.

Figure 7.- Continued.



(n) $t = 1663.6$ to 1664.8 seconds.

Figure 7.- Continued.



(a) $t = 1664.8$ to 1666.0 seconds.

Figure 7.- Concluded.

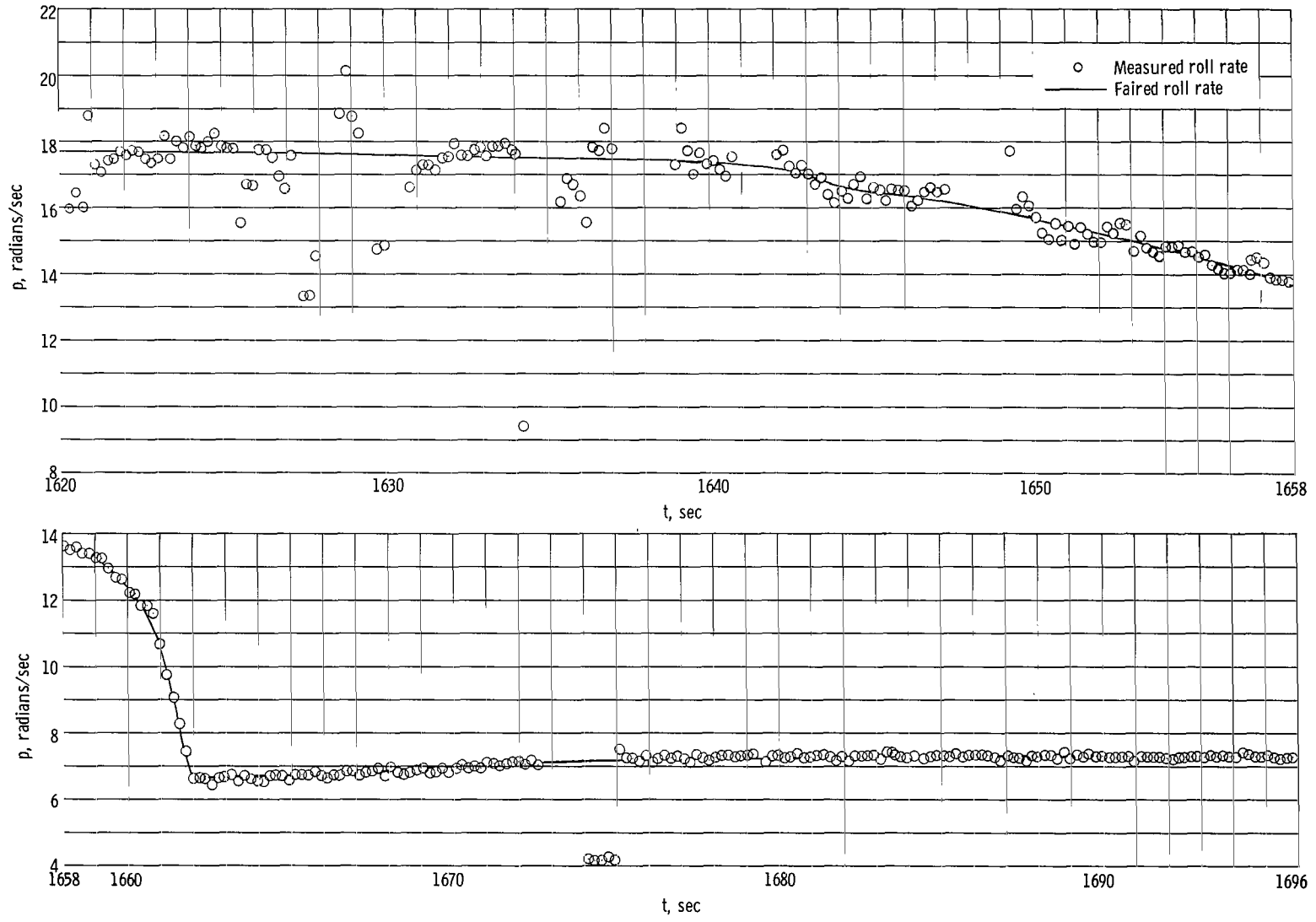


Figure 8.- Variation of roll rate with elapsed flight time.

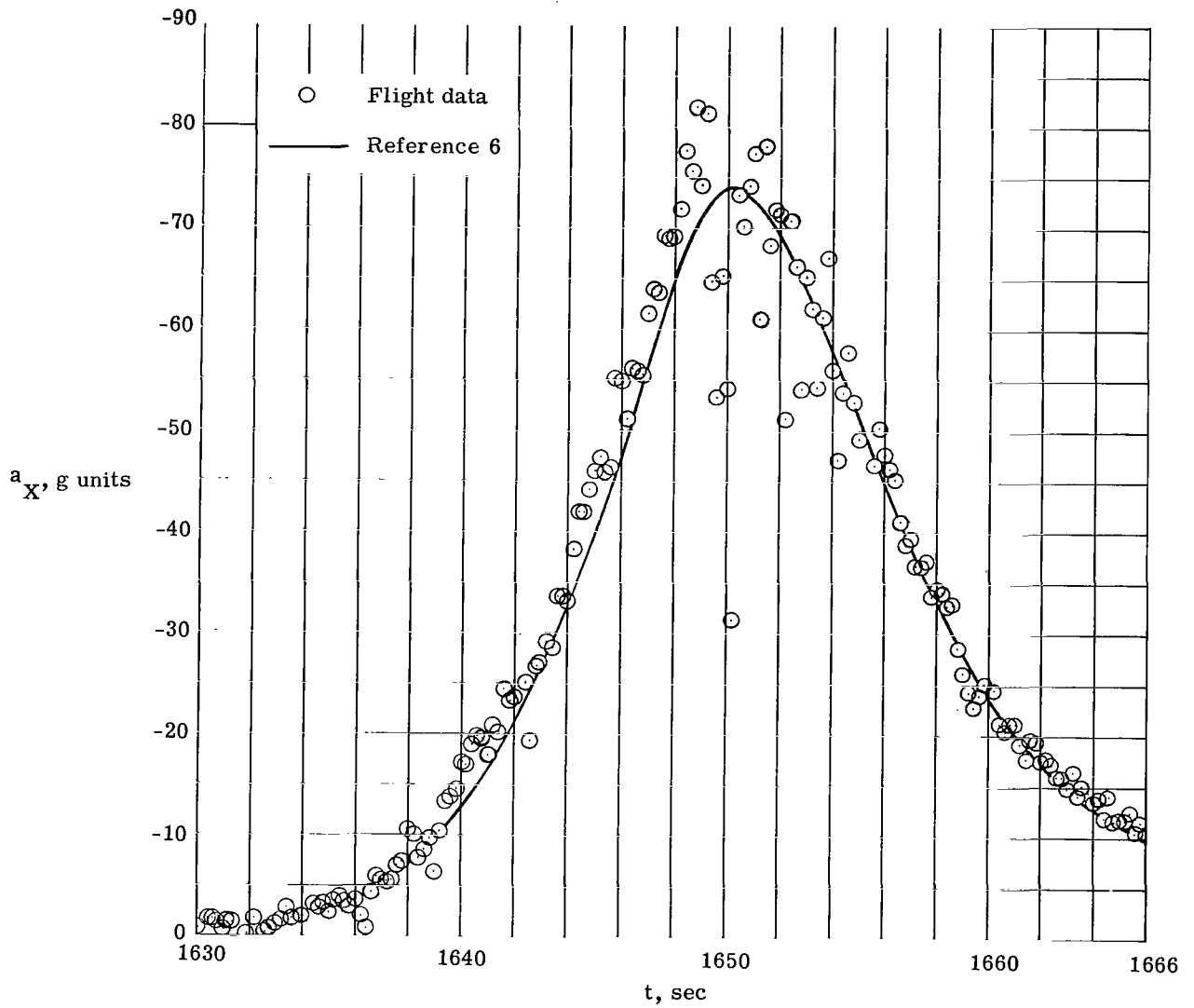
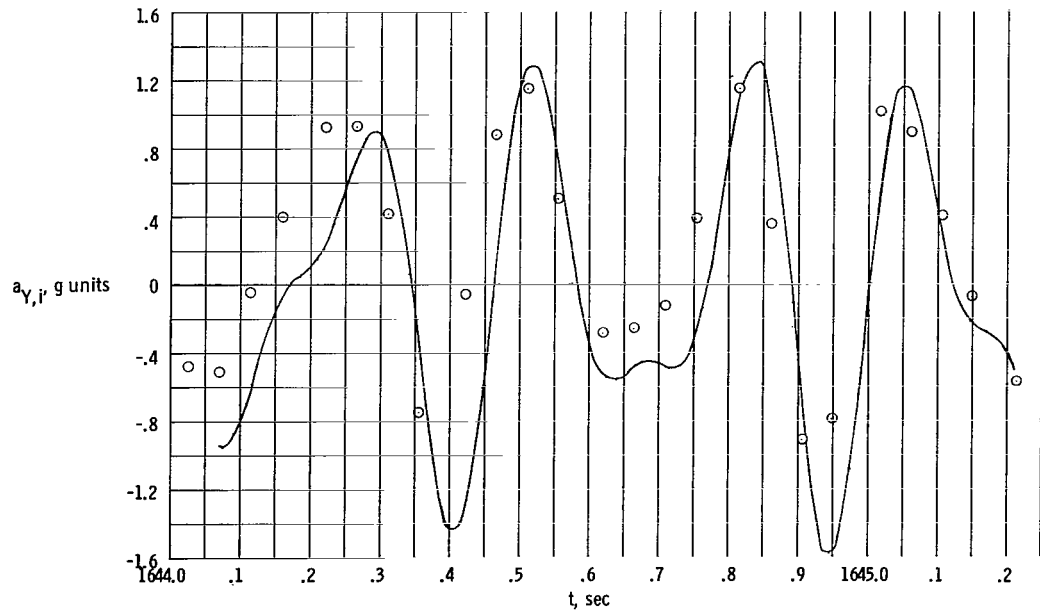
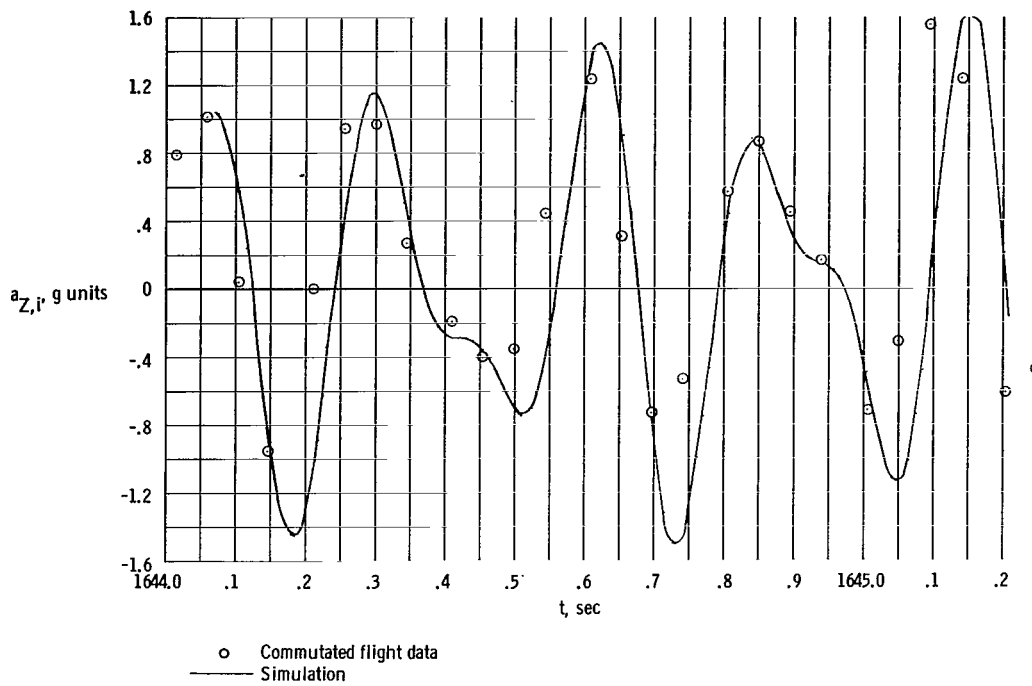
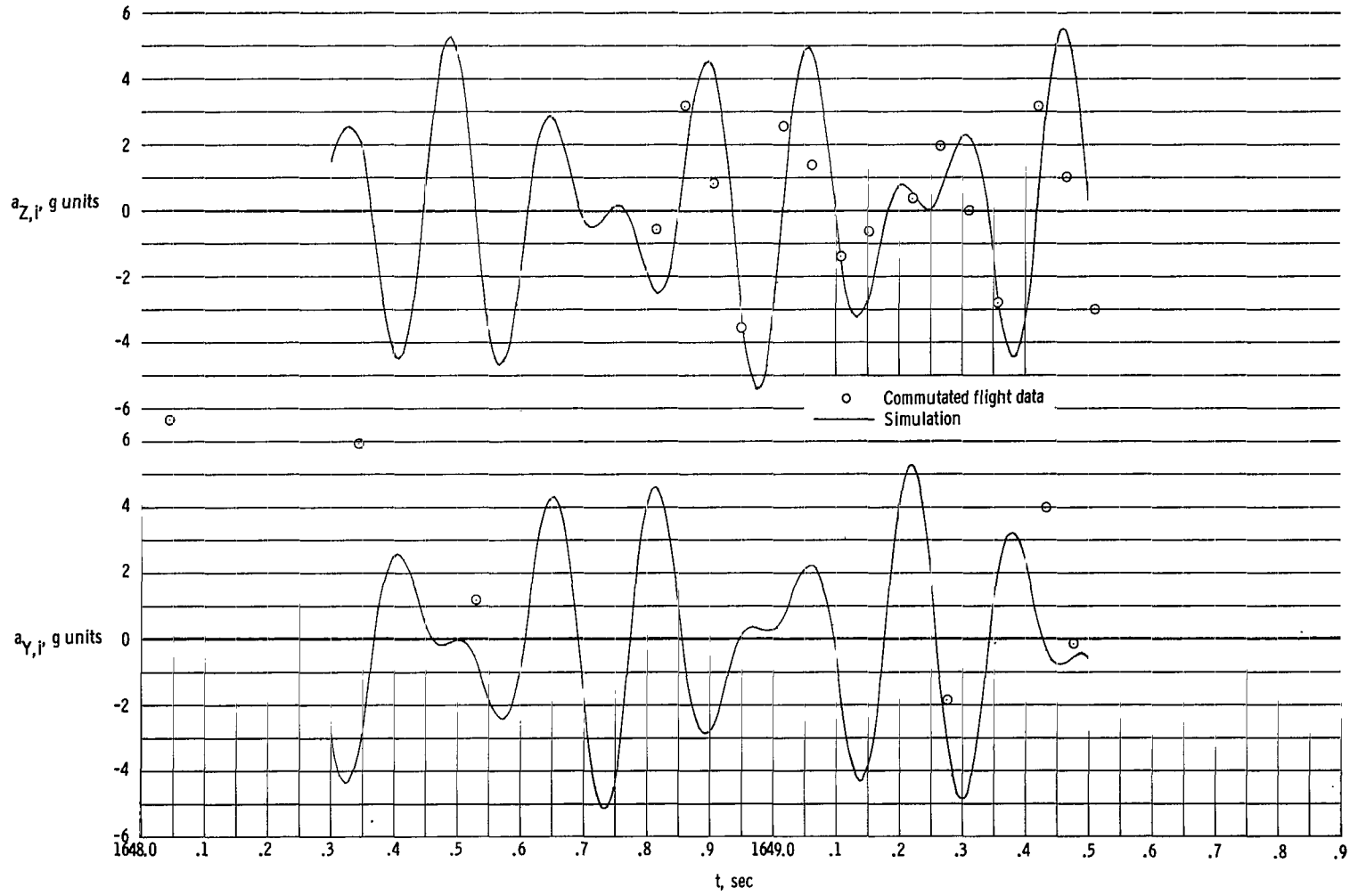


Figure 9.- Variation of longitudinal acceleration with elapsed flight time.



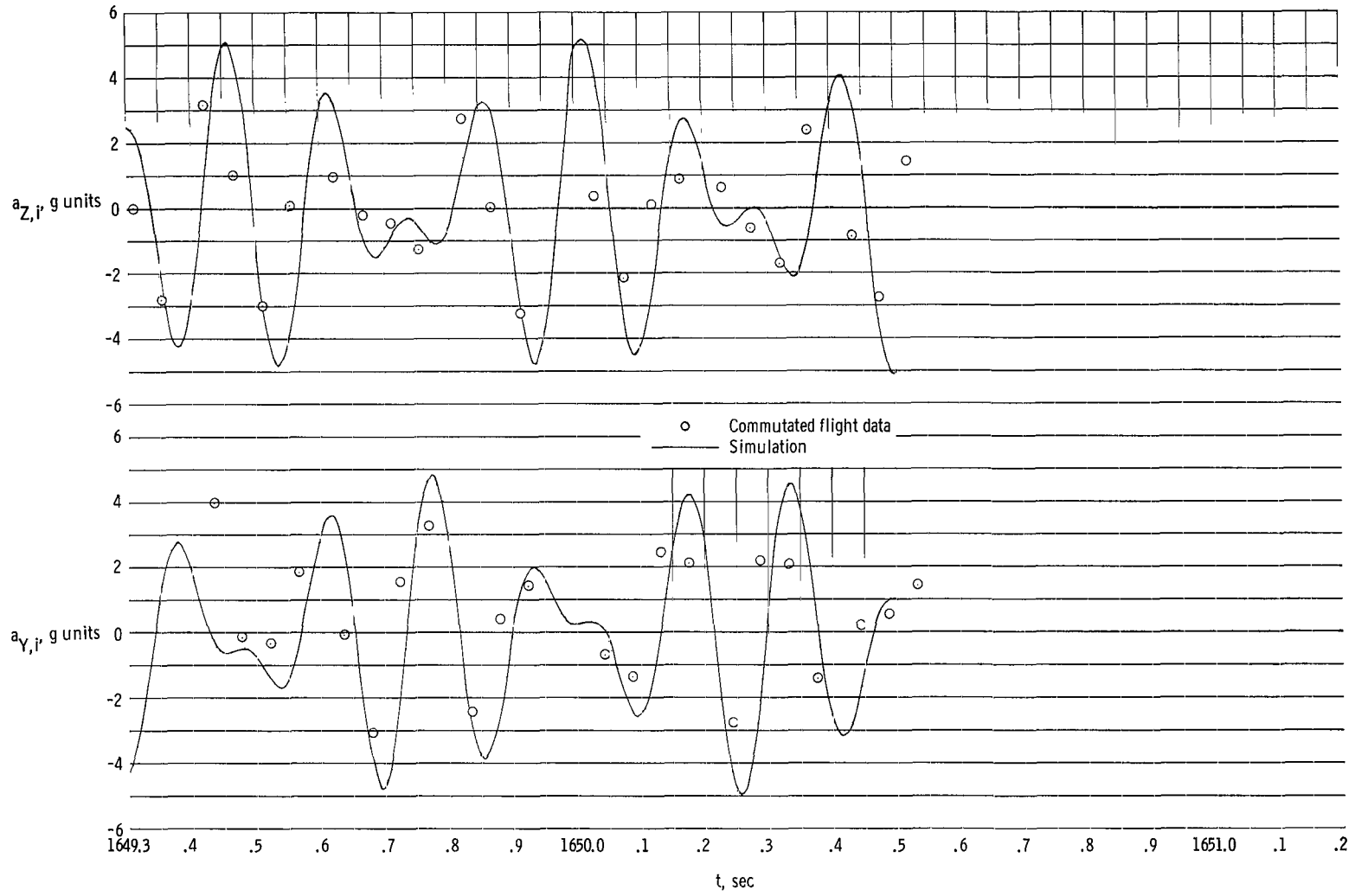
(a) $t = 1644,0$ to $1645,2$ seconds.

Figure 10.- Flight measured normal and lateral accelerations and simulation results.



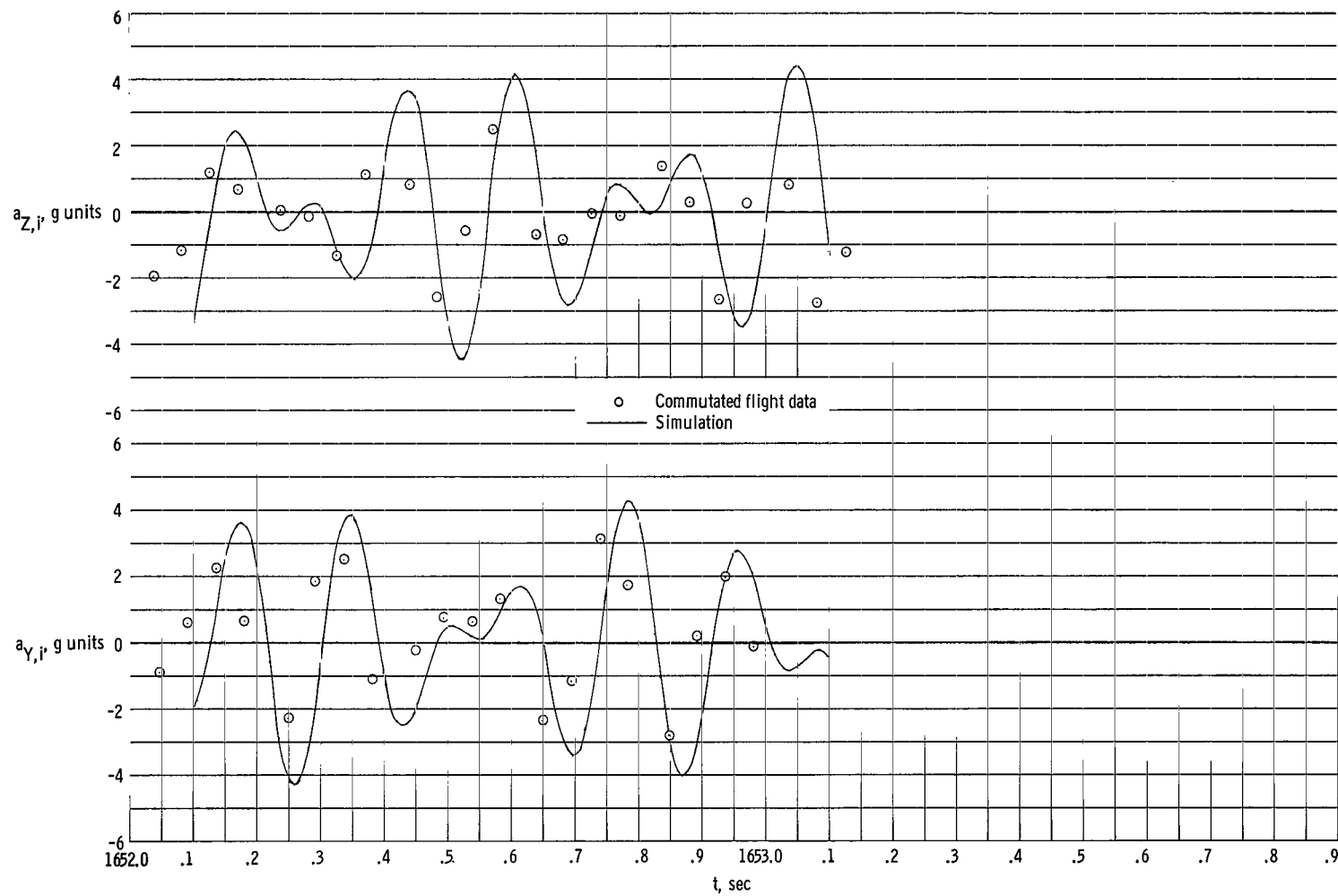
(b) $t = 1648.0$ to 1649.5 seconds.

Figure 10.- Continued.



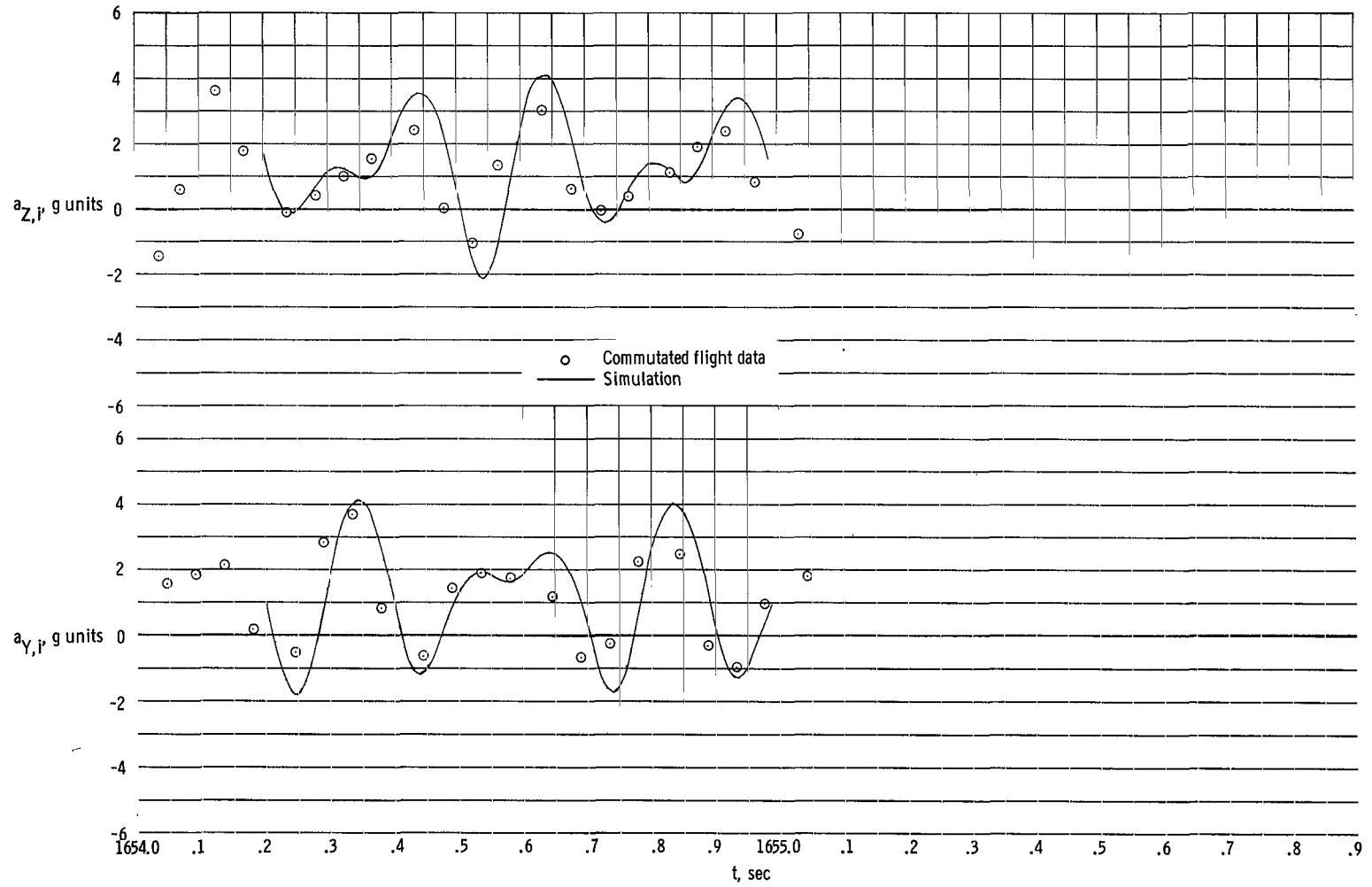
(c) $t = 1649,3$ to $1650,6$ seconds.

Figure 10.- Continued.



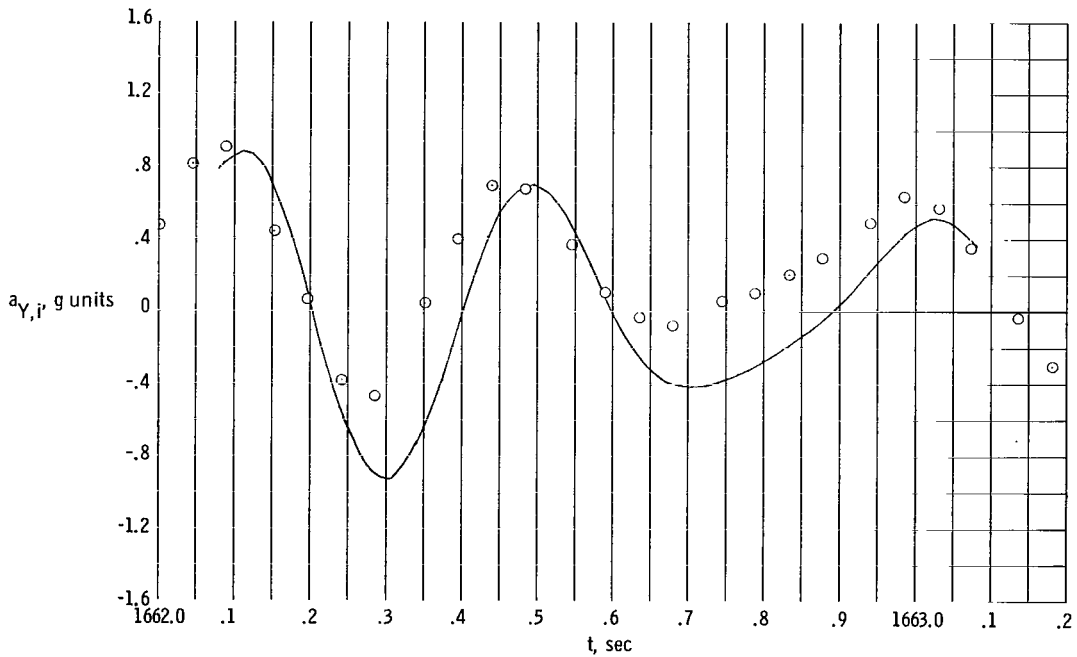
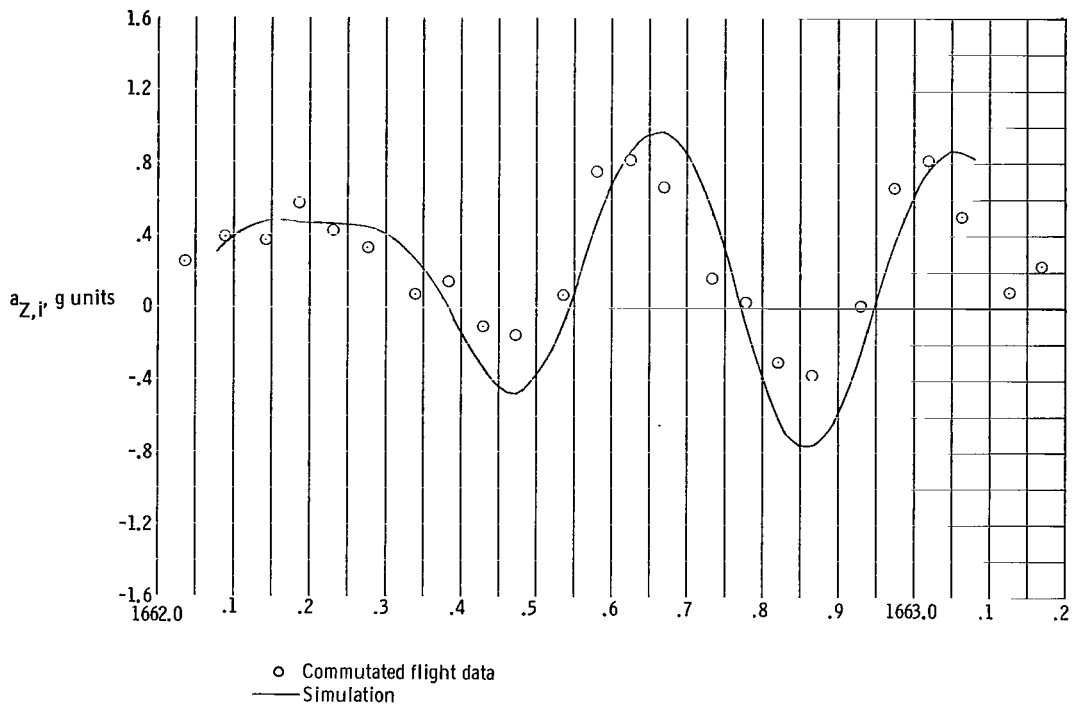
(d) $t = 1652.0$ to 1653.1 seconds.

Figure 10.- Continued.



(e) $t = 1654.0$ to 1655.1 seconds.

Figure 10.- Continued.



(f) $t = 1662.0$ to 1663.2 seconds.

Figure 10.- Concluded.

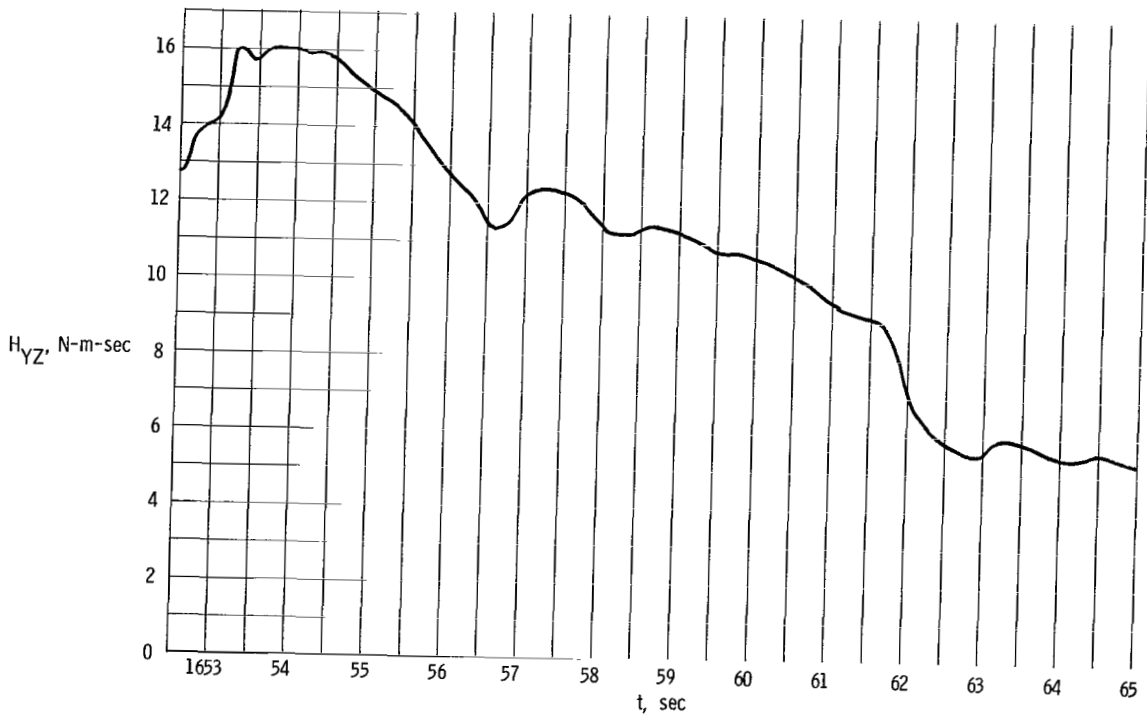
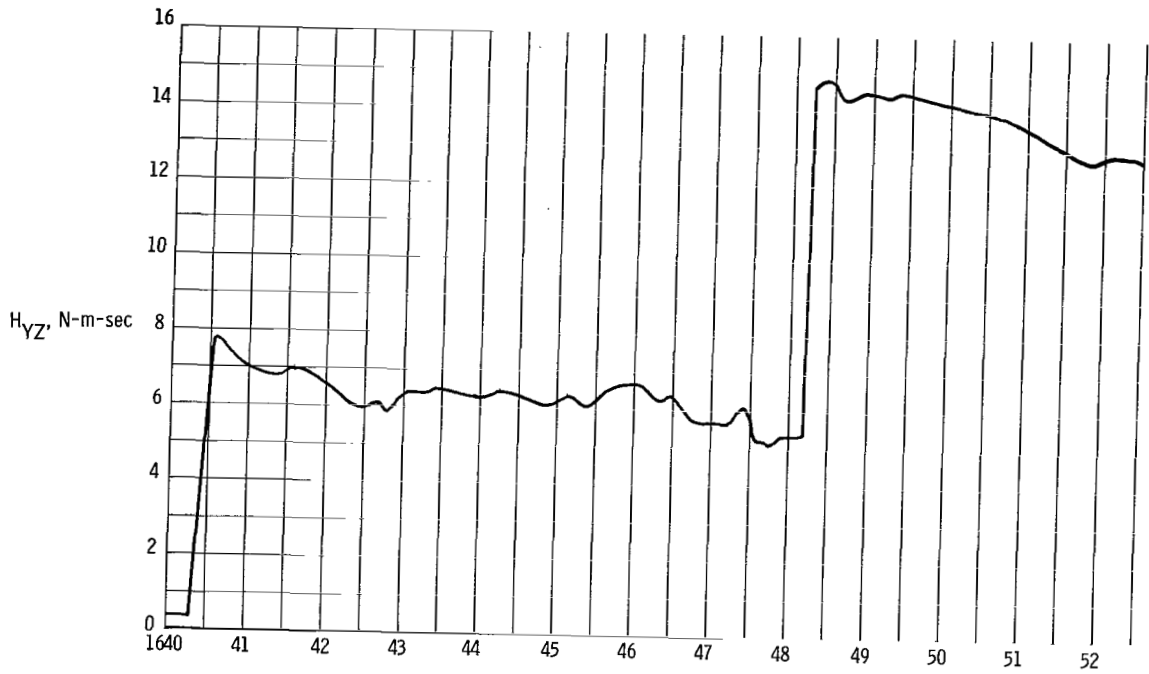
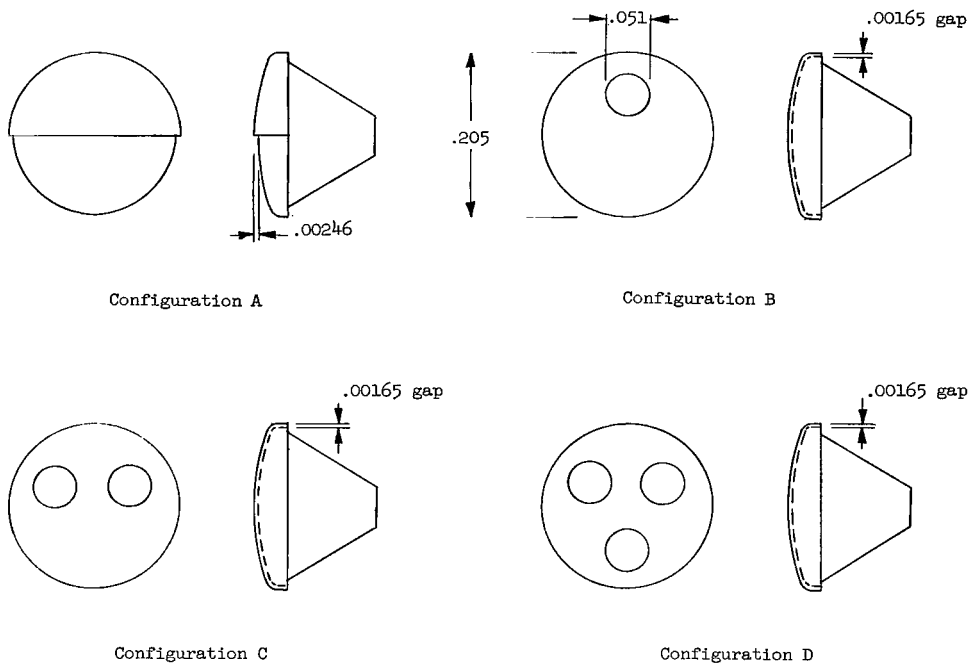


Figure 11.- Variation of resultant angular momentum about Y_b - and Z_b -axes with elapsed flight time.



All dimensions are given in meters

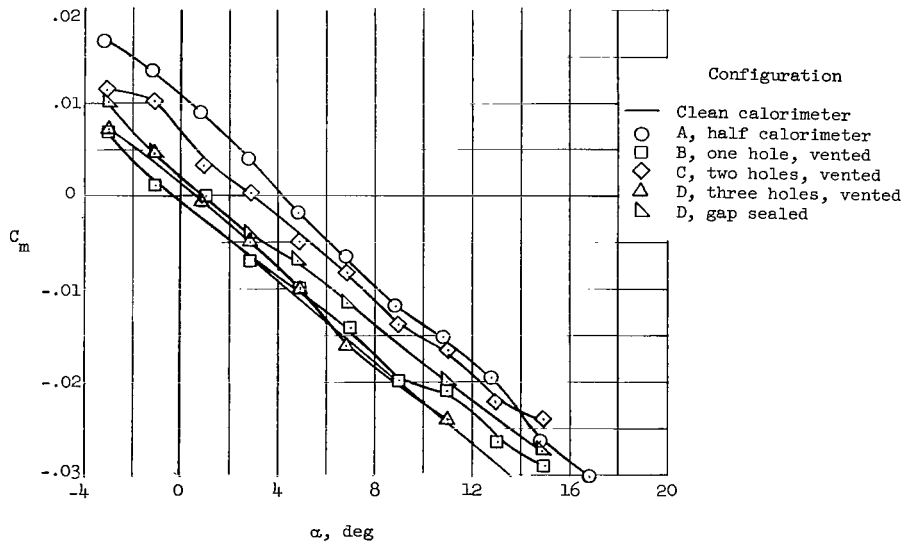


Figure 12.- Effect of modifications to calorimeter face on the pitching moments of a 1/3-scale model of the reentry package. Mach number, 4.63.

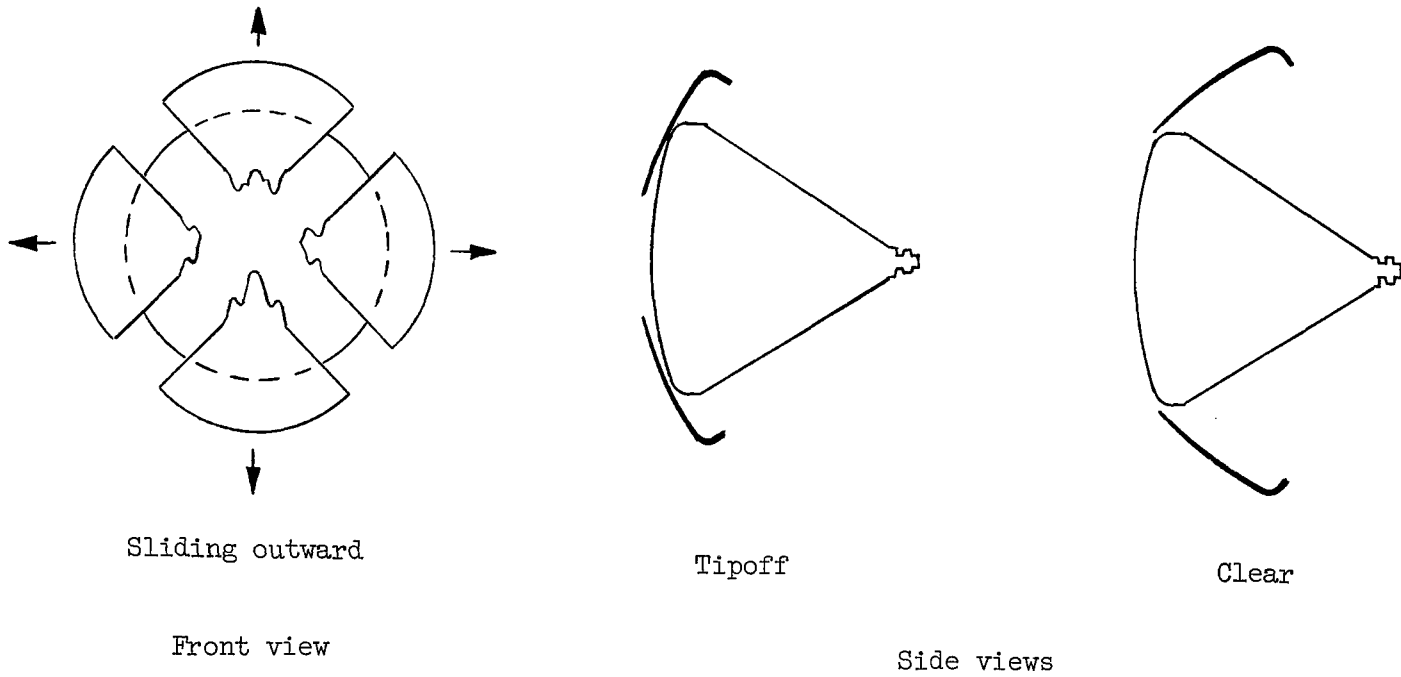


Figure 13.- Illustration of the movement of the heat-shield sectors during ejections.

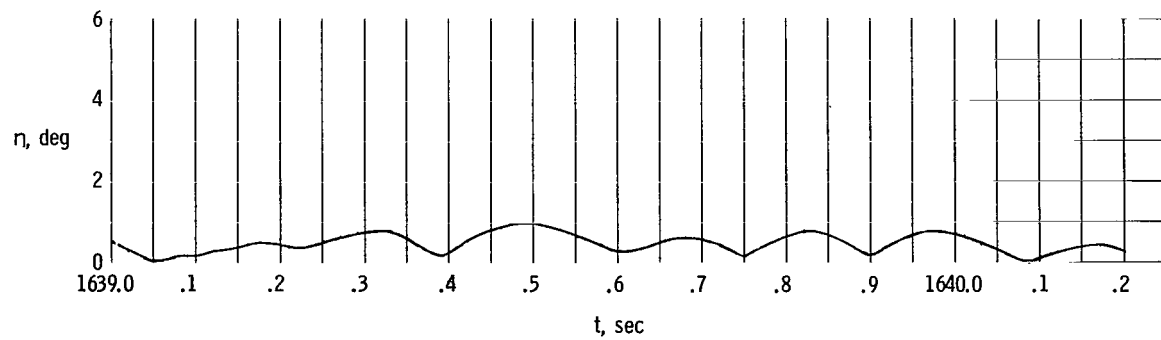
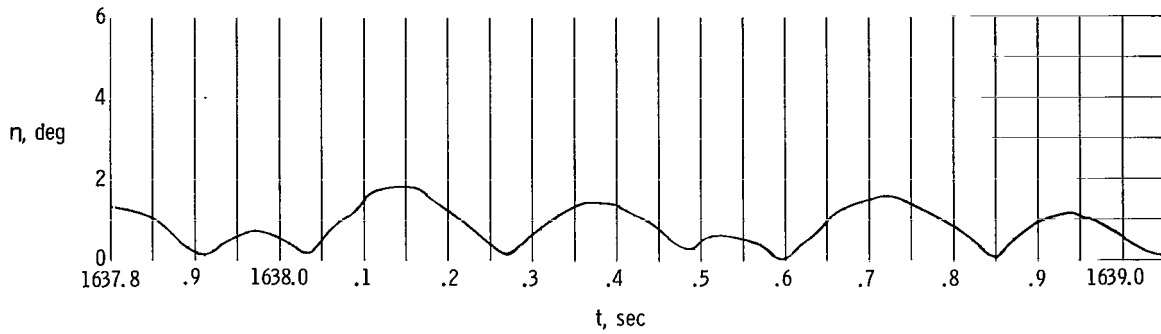
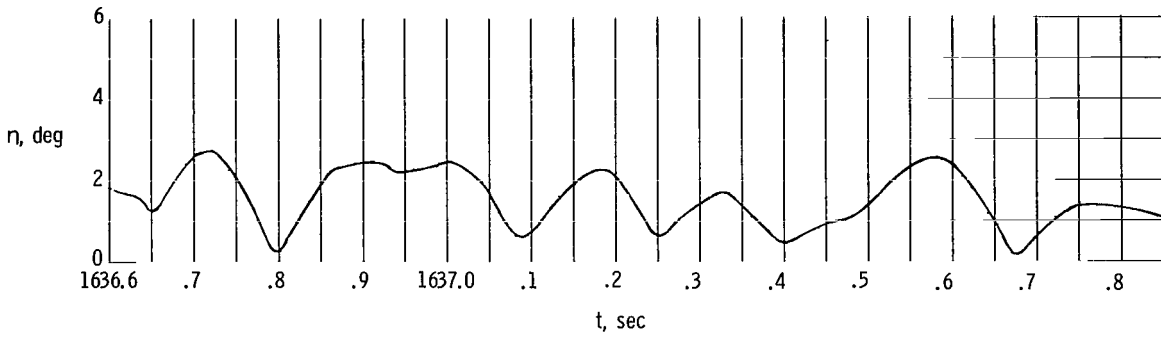
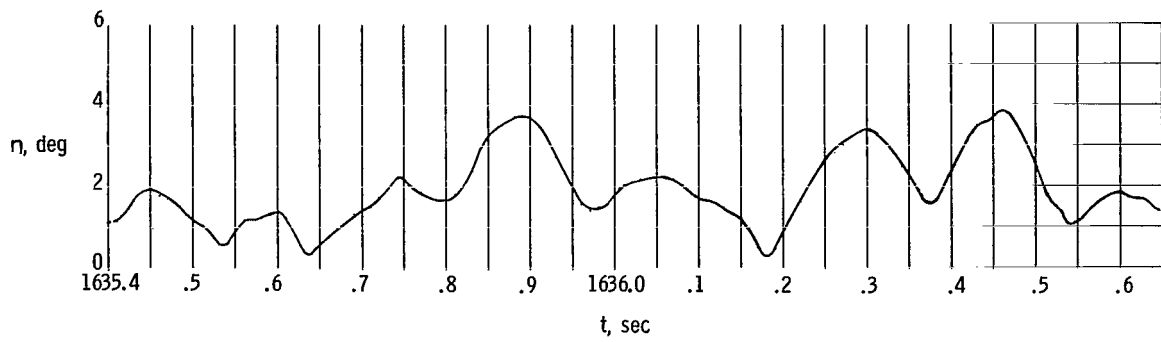
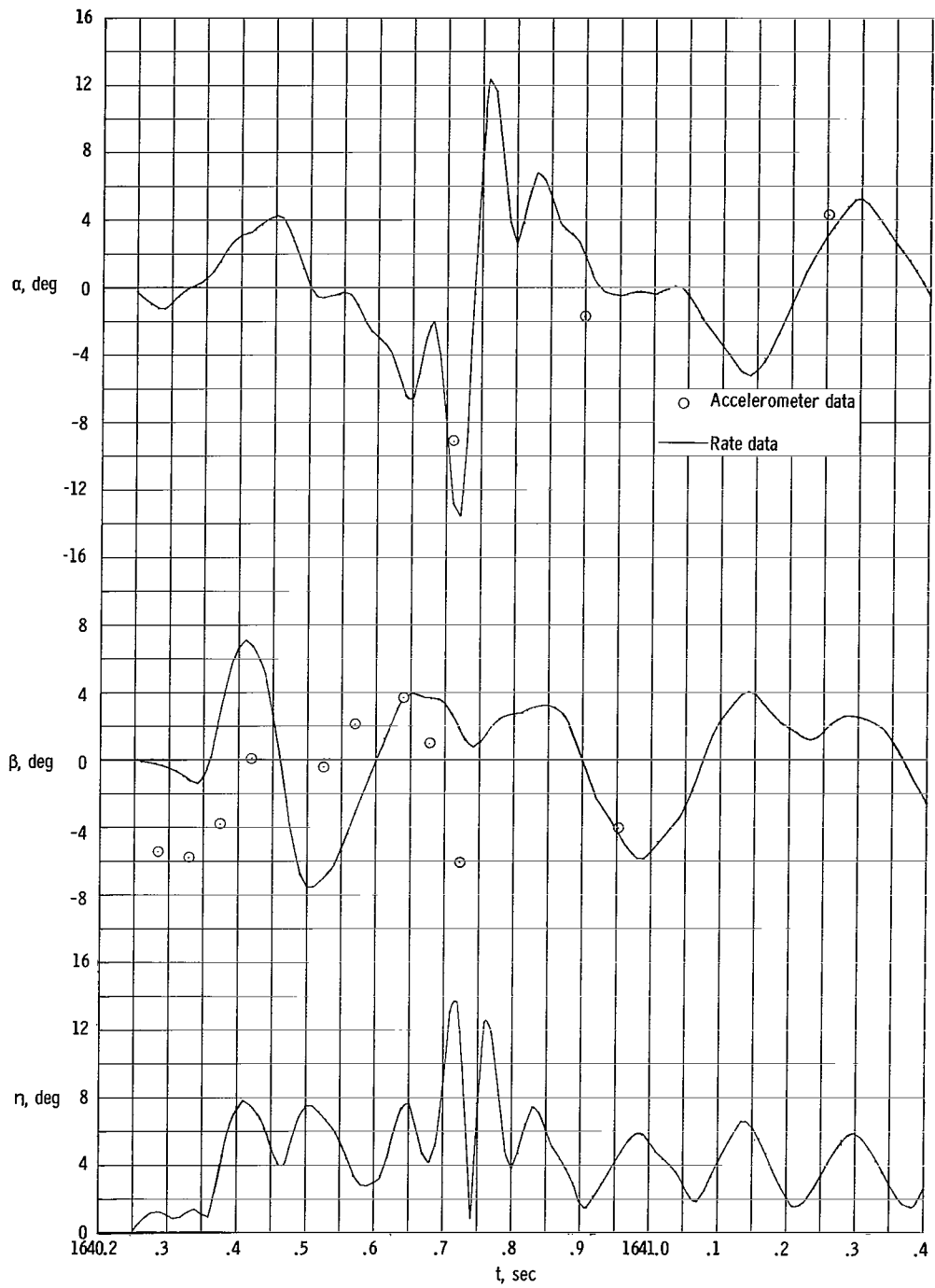
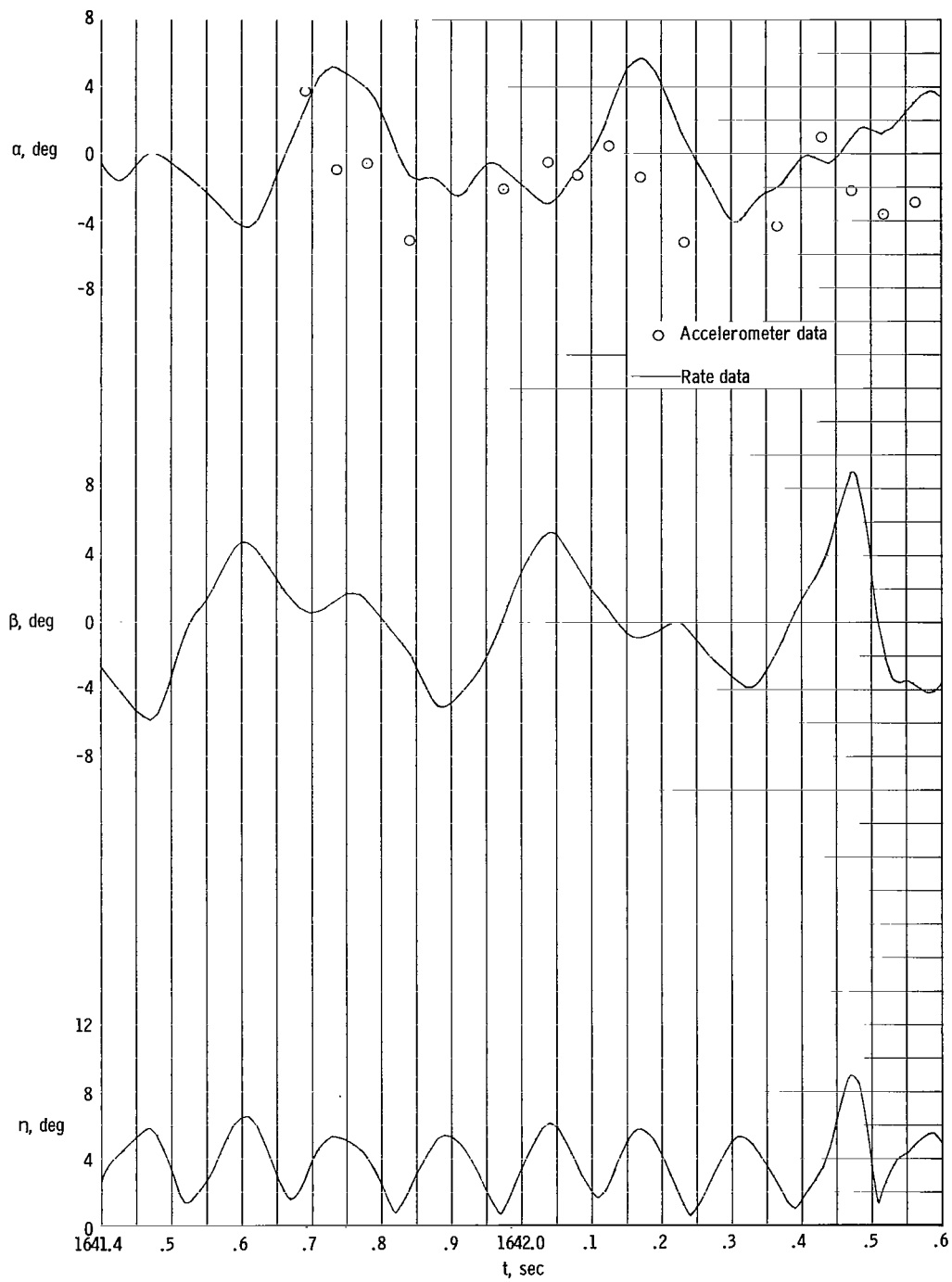


Figure 14.- Total angles of attack prior to melting of first beryllium calorimeter.



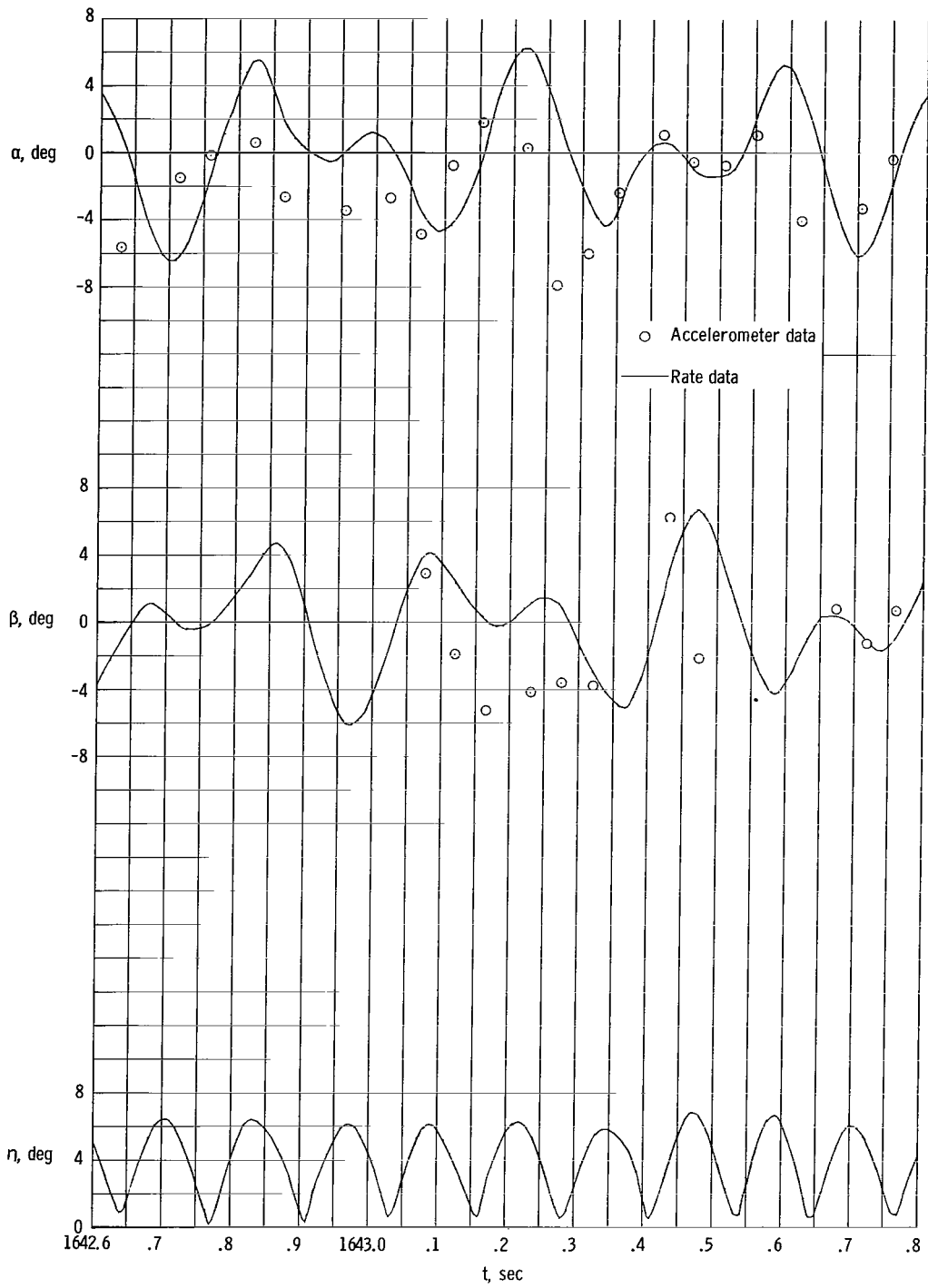
(a) $t = 1640.2$ to 1641.4 seconds.

Figure 15.- Angle of attack, angle of sideslip, and total angle of attack from melting of the first beryllium calorimeter to ejection of the second phenolic-asbestos heat shield.



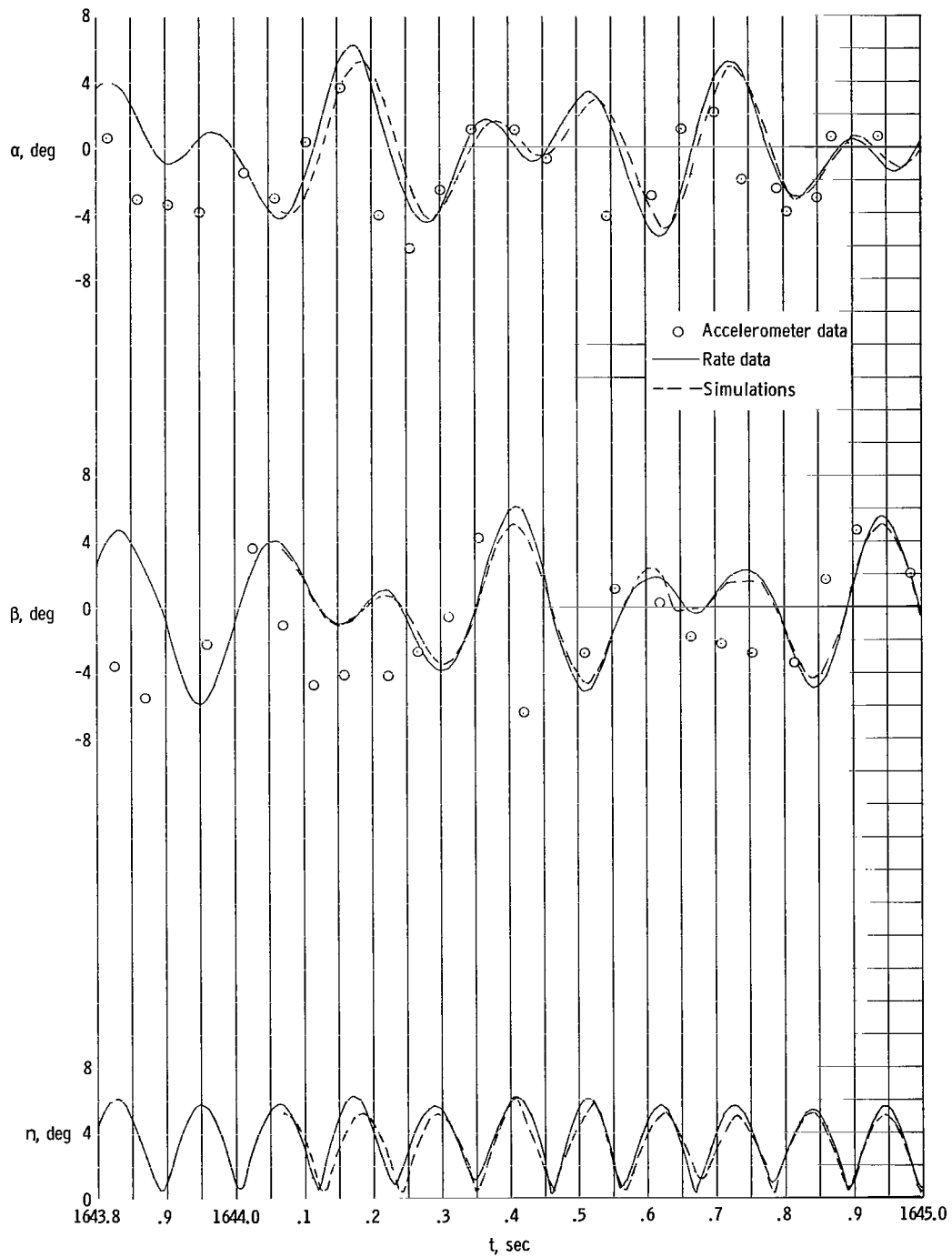
(b) $t = 1641.4$ to 1642.6 seconds.

Figure 15.- Continued.



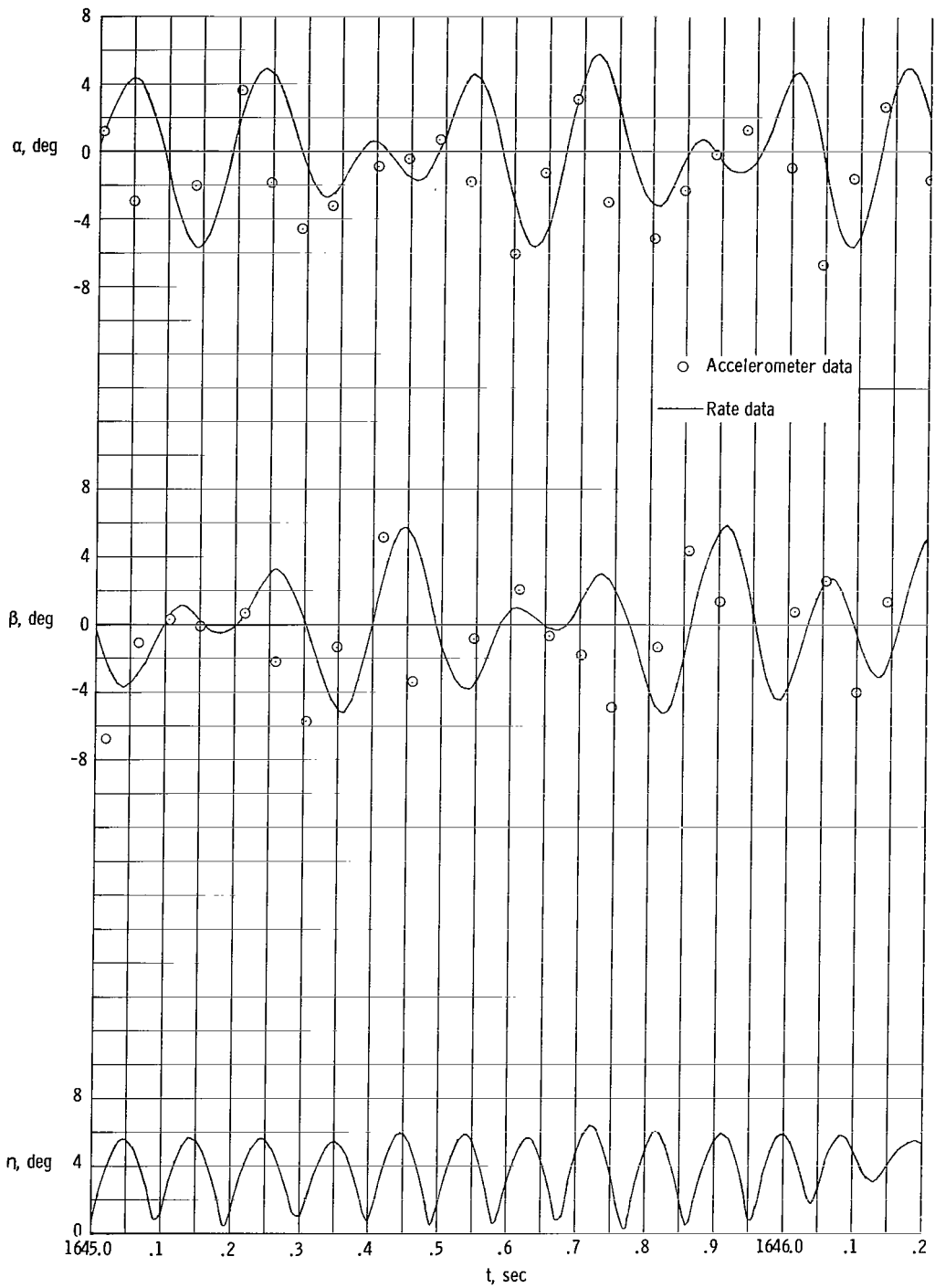
(c) $t = 1642.6$ to 1643.8 seconds.

Figure 15.- Continued.



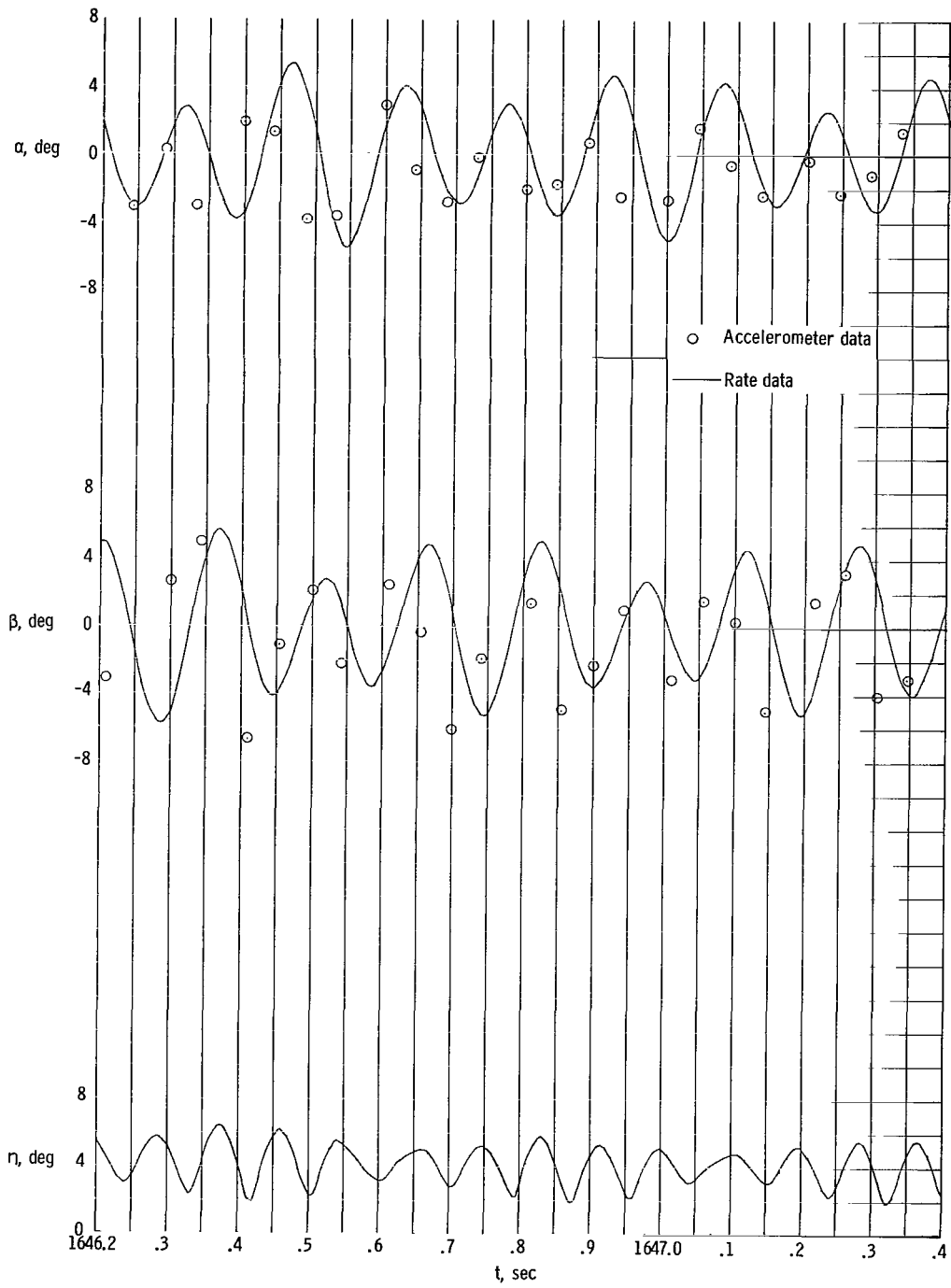
(d) $t = 1643,8$ to $1645,0$ seconds.

Figure 15.- Continued.



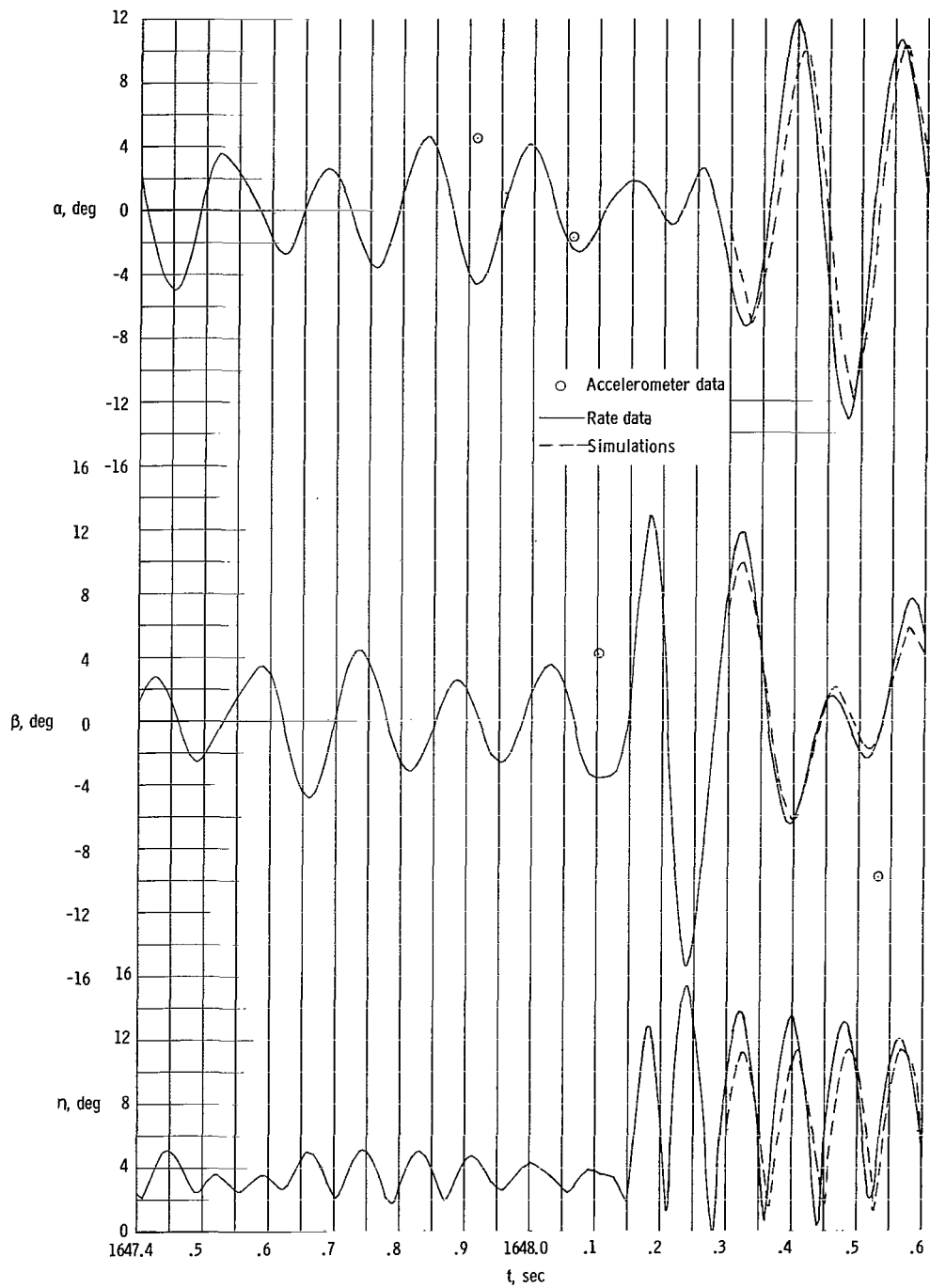
(e) $t = 1645.0$ to 1646.2 seconds.

Figure 15.- Continued.



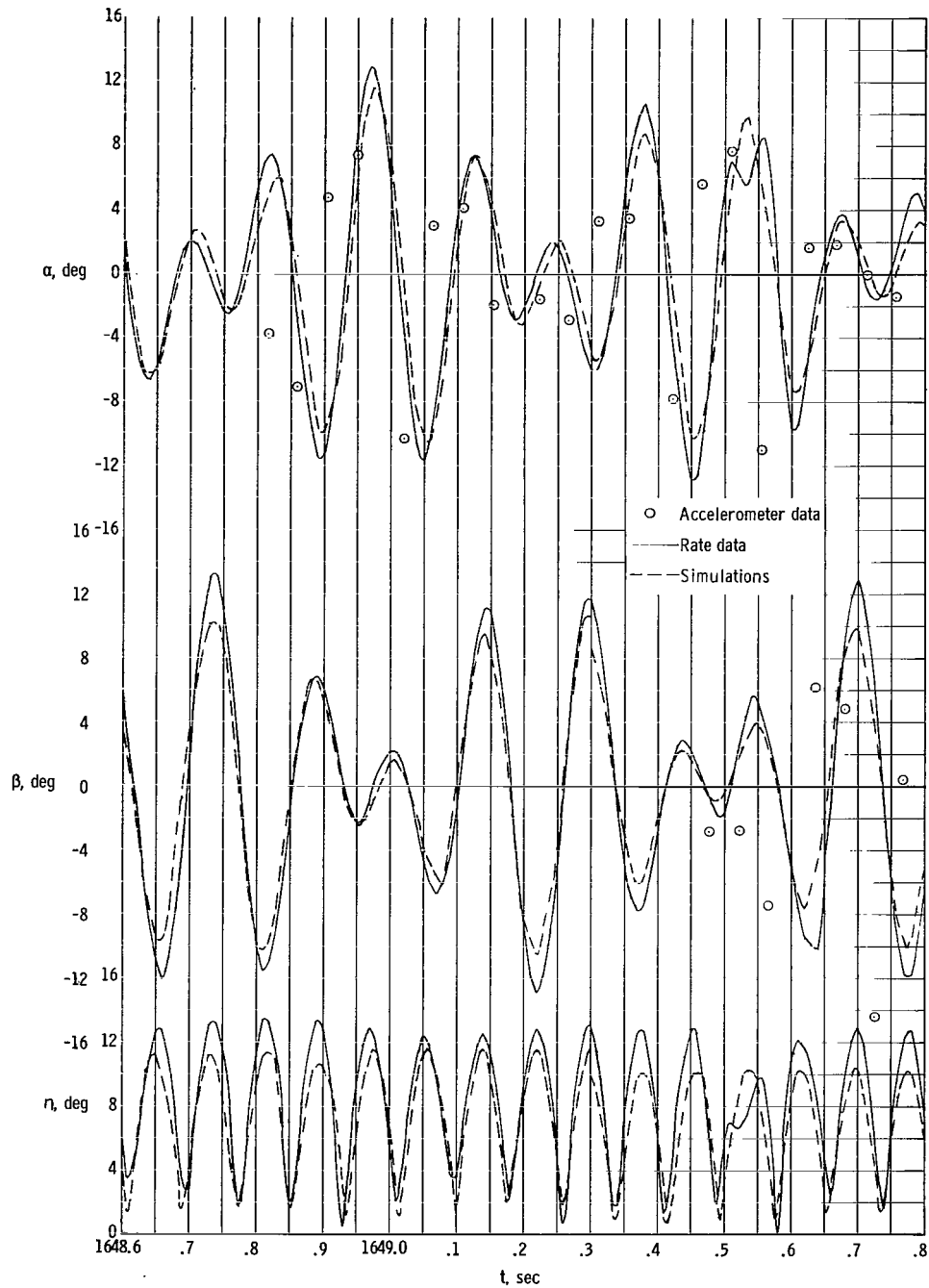
(f) $t = 1646.2$ to 1647.4 seconds.

Figure 15.- Concluded.



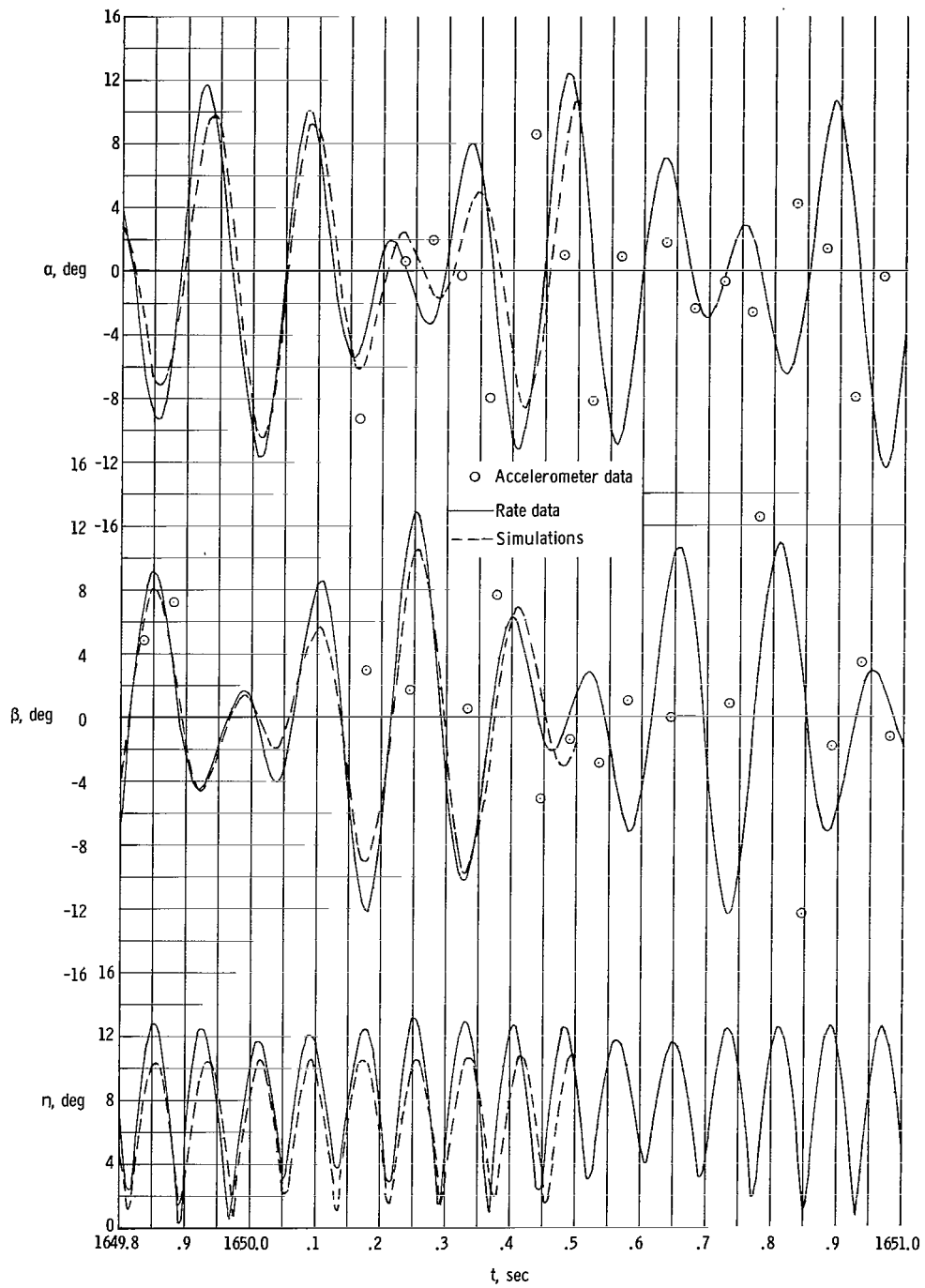
(a) $t = 1647.4$ to 1648.6 seconds.

Figure 16.- Angle of attack, angle of sideslip, and total angle of attack from ejection of the second phenolic-asbestos heat shield to $t = 1665.4$ seconds.



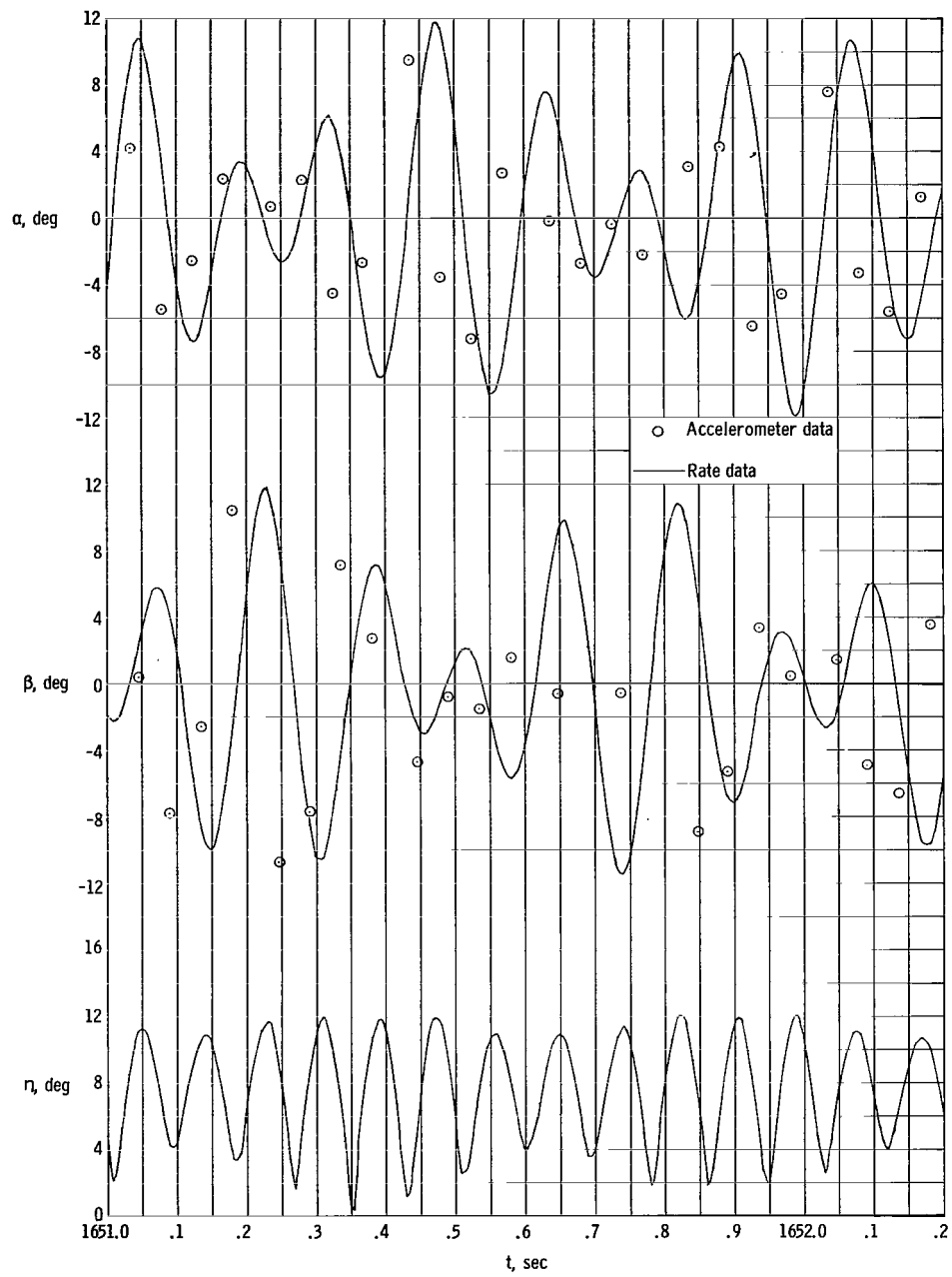
(b) $t = 1648.6$ to 1649.8 seconds.

Figure 16.- Continued.



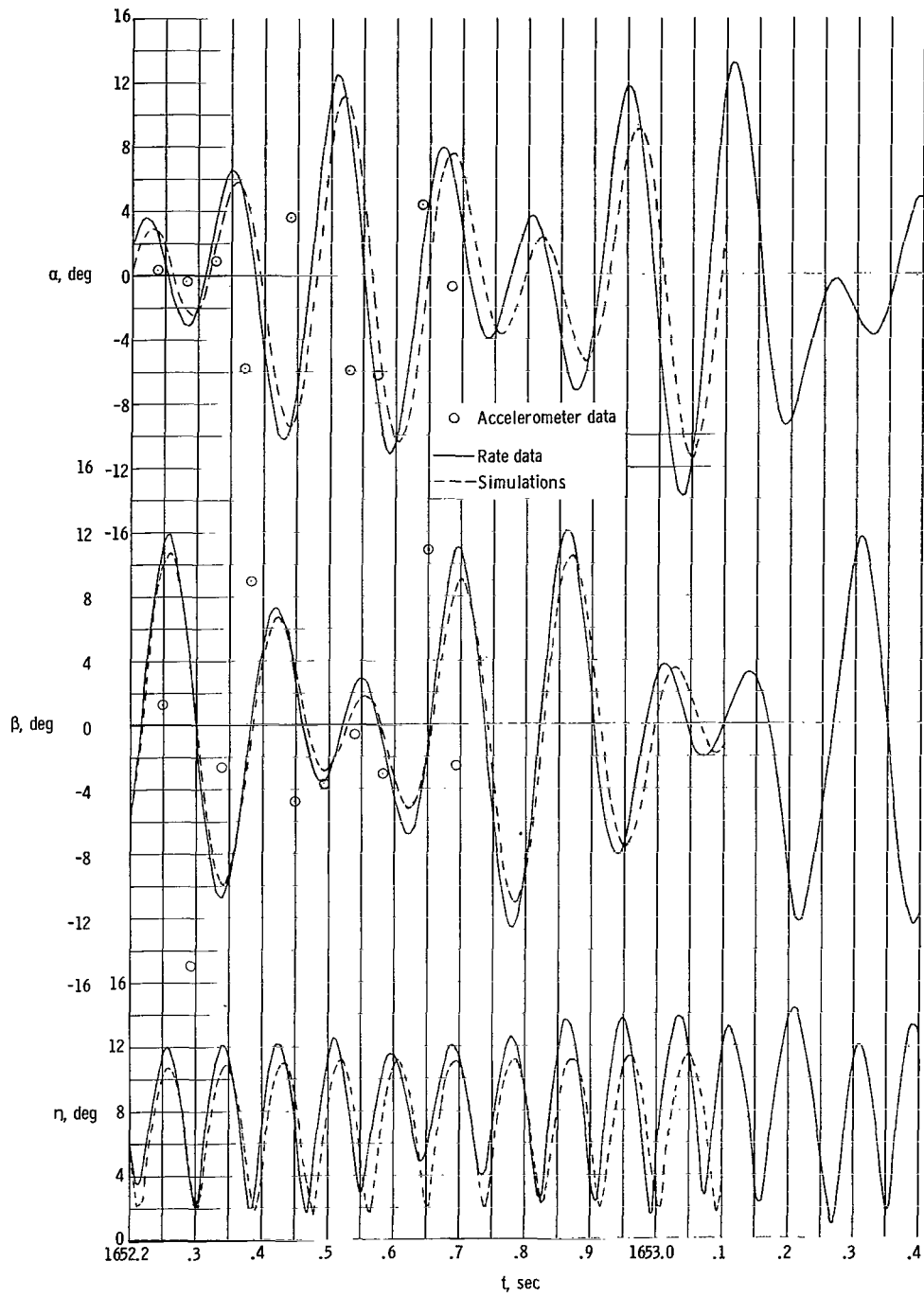
(c) $t = 1649.8$ to 1651.0 seconds.

Figure 16.- Continued.



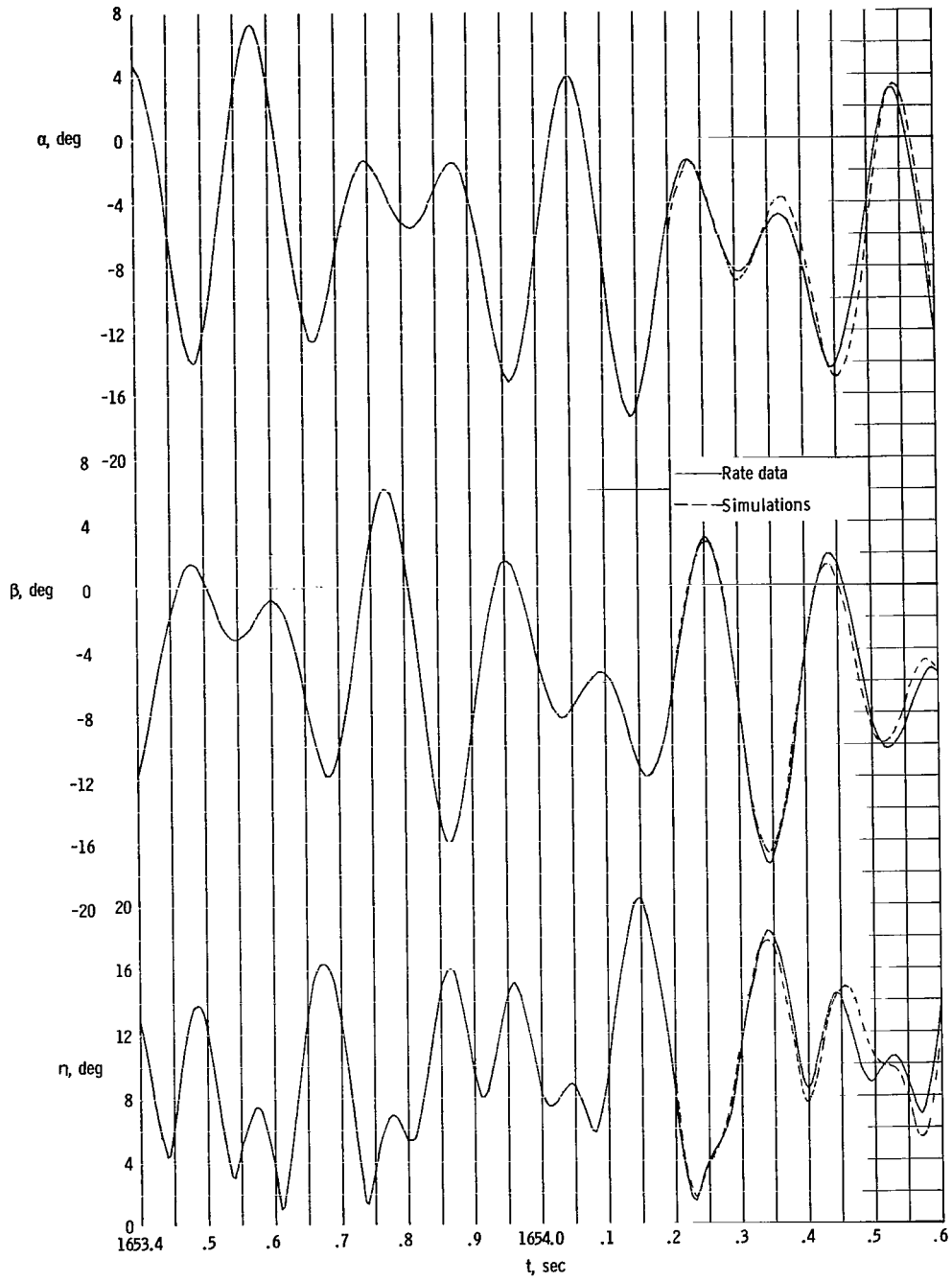
(d) $t = 1651.0$ to 1652.2 seconds.

Figure 16.- Continued.



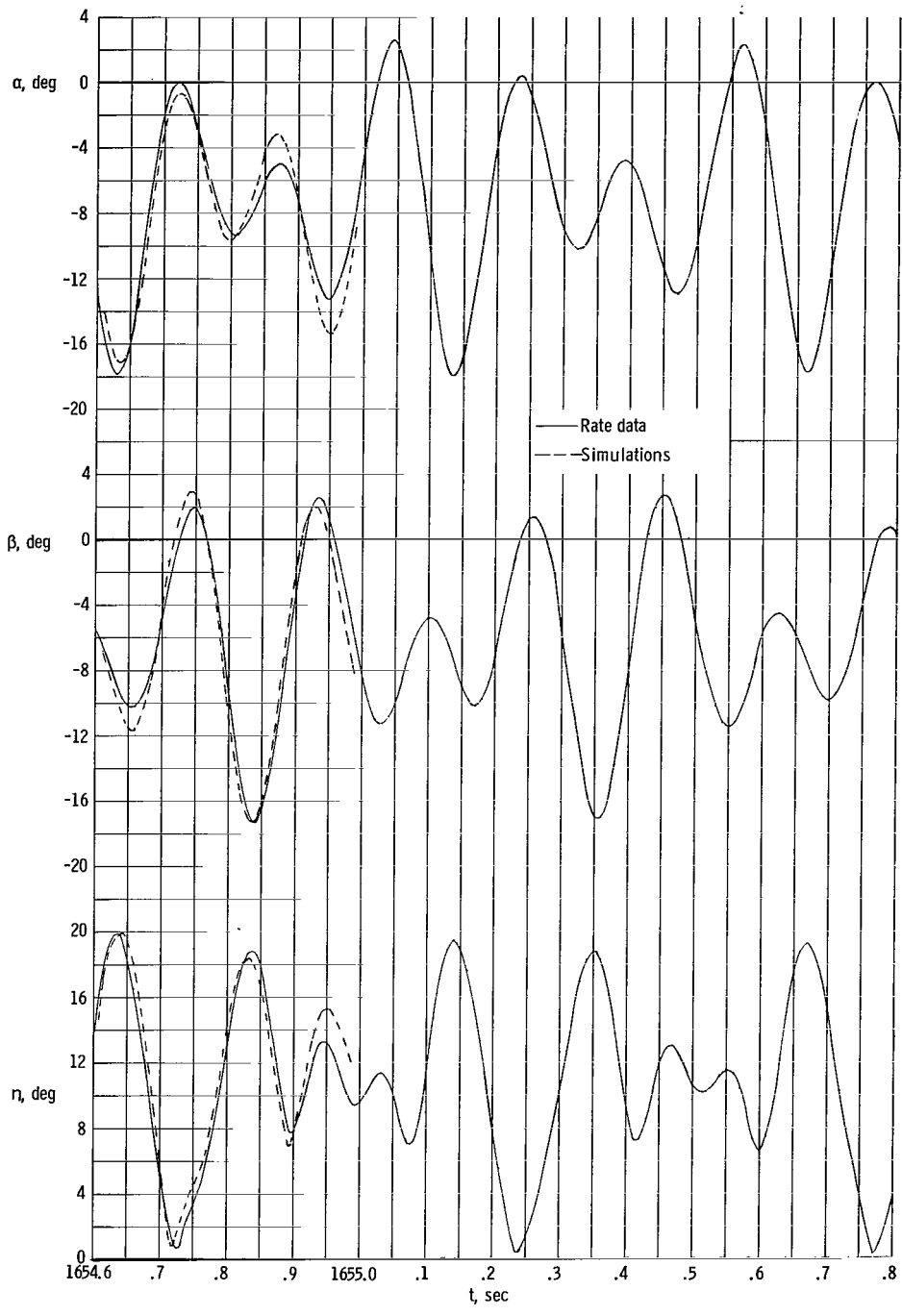
(e) $t = 1652.2$ to 1653.4 seconds.

Figure 16.- Continued.



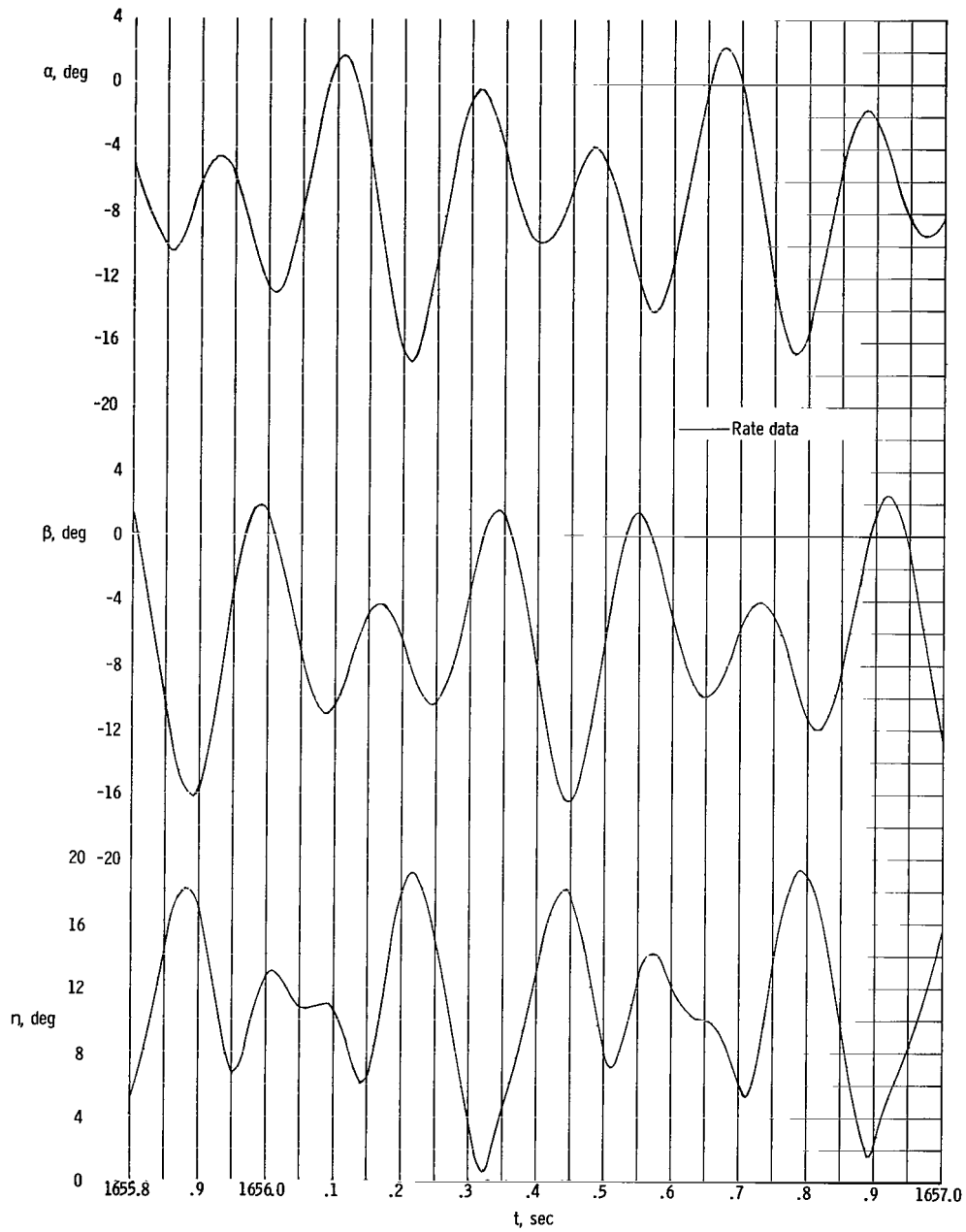
(f) $t = 1653.4$ to 1654.6 seconds.

Figure 16.- Continued.



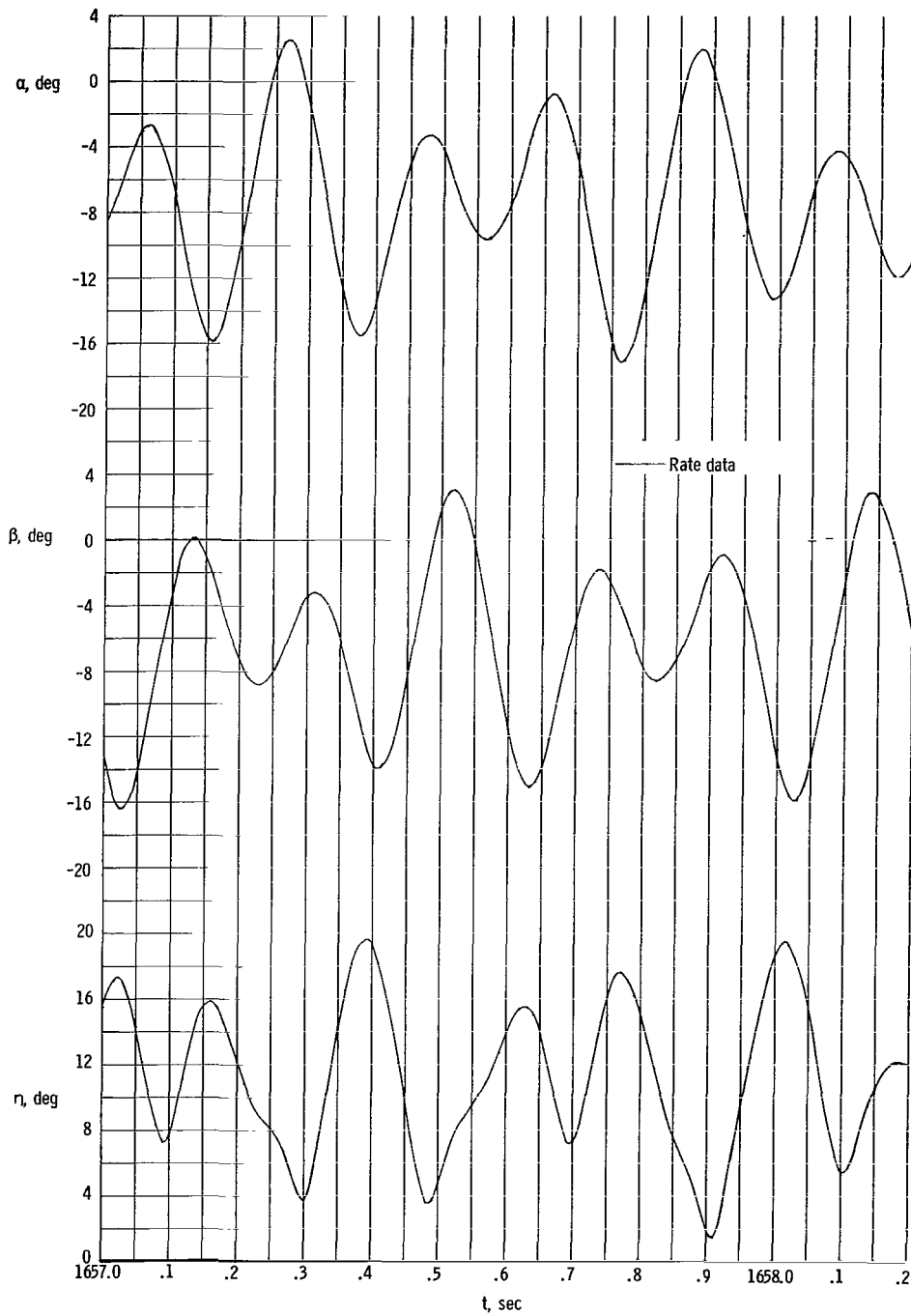
(g) $t = 1654.6$ to 1655.8 seconds.

Figure 16.- Continued.



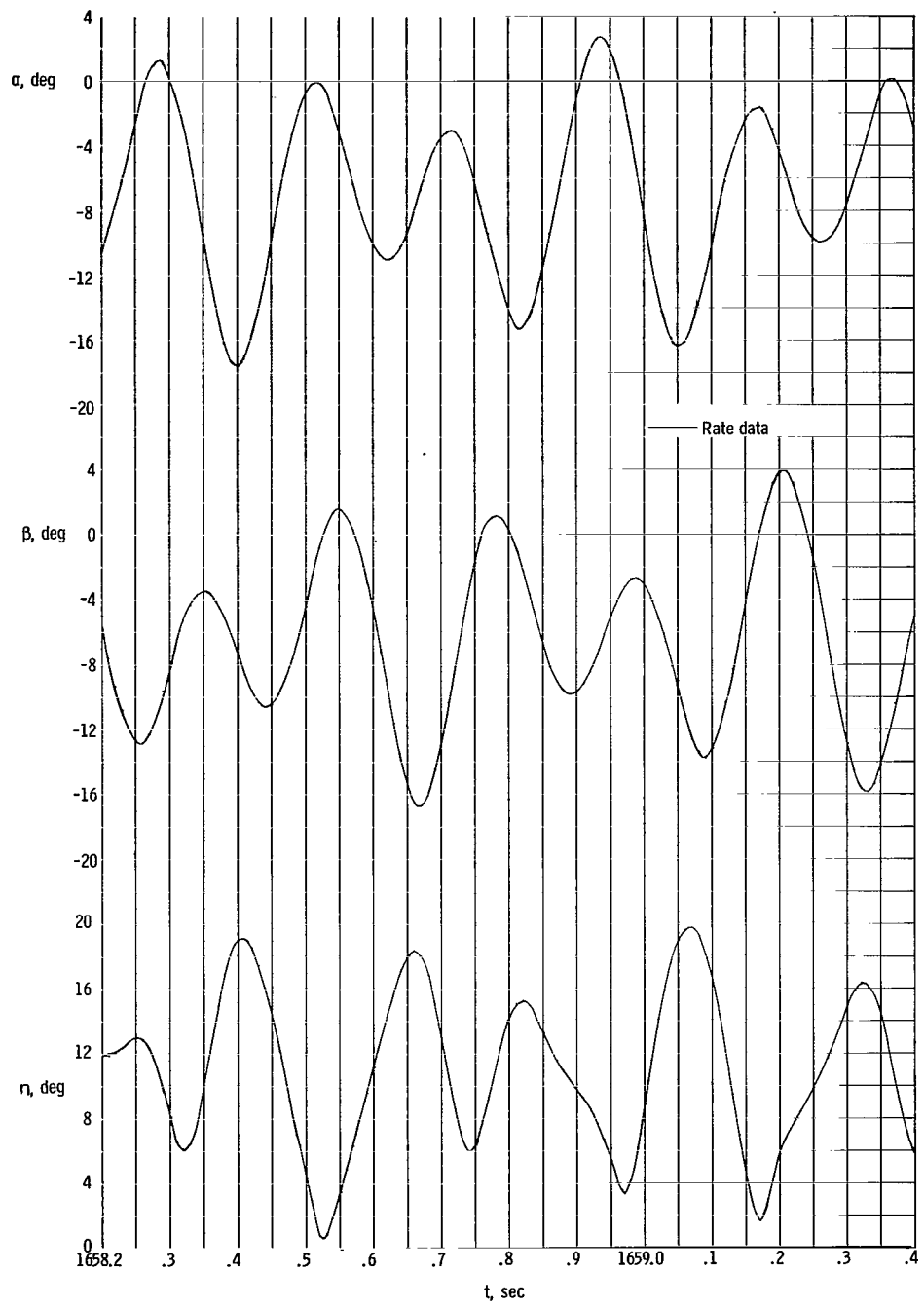
(h) $t = 1655.8$ to 1657.0 seconds.

Figure 16.- Continued.



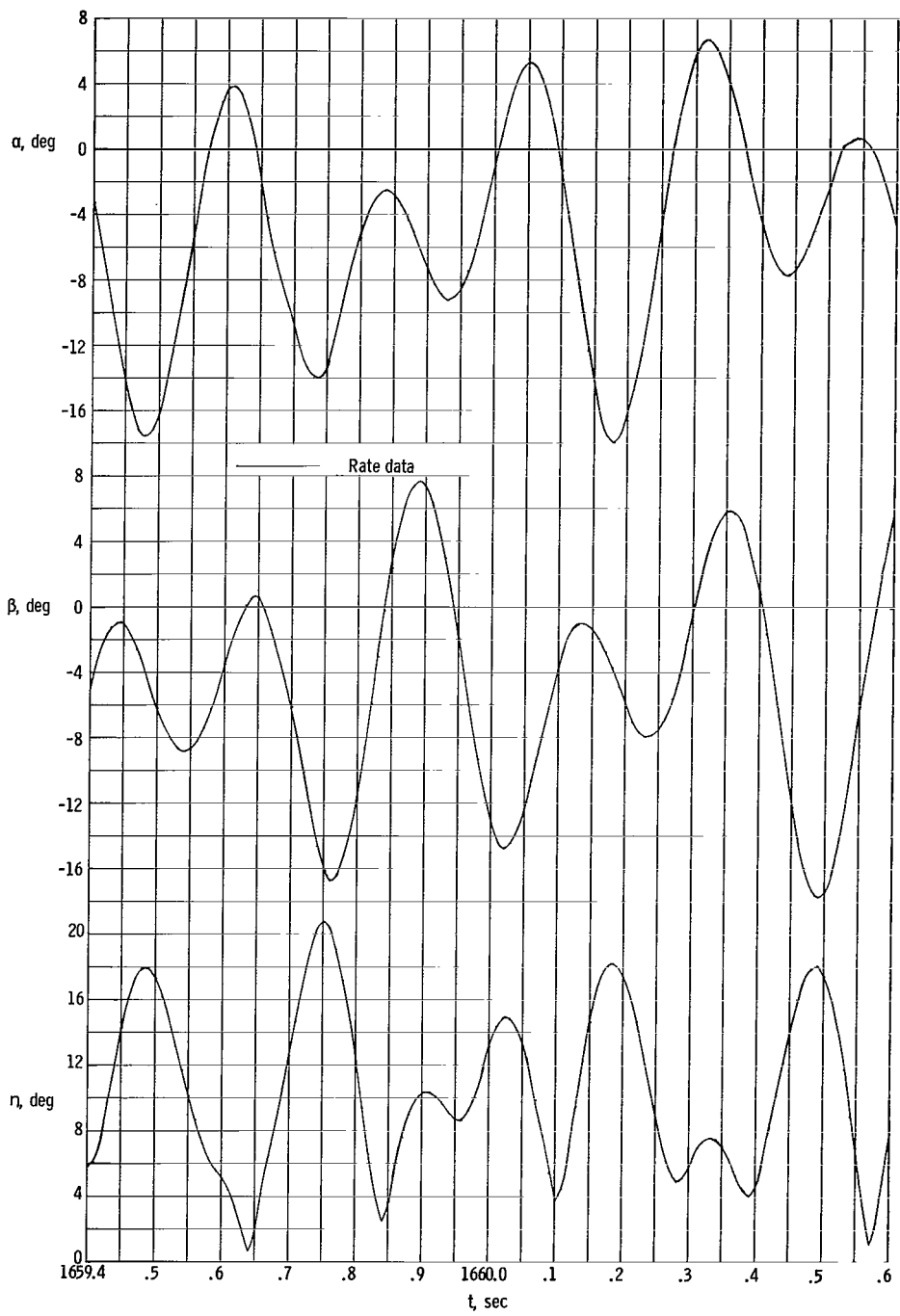
(i) $t = 1657.0$ to 1658.2 seconds.

Figure 16.- Continued.



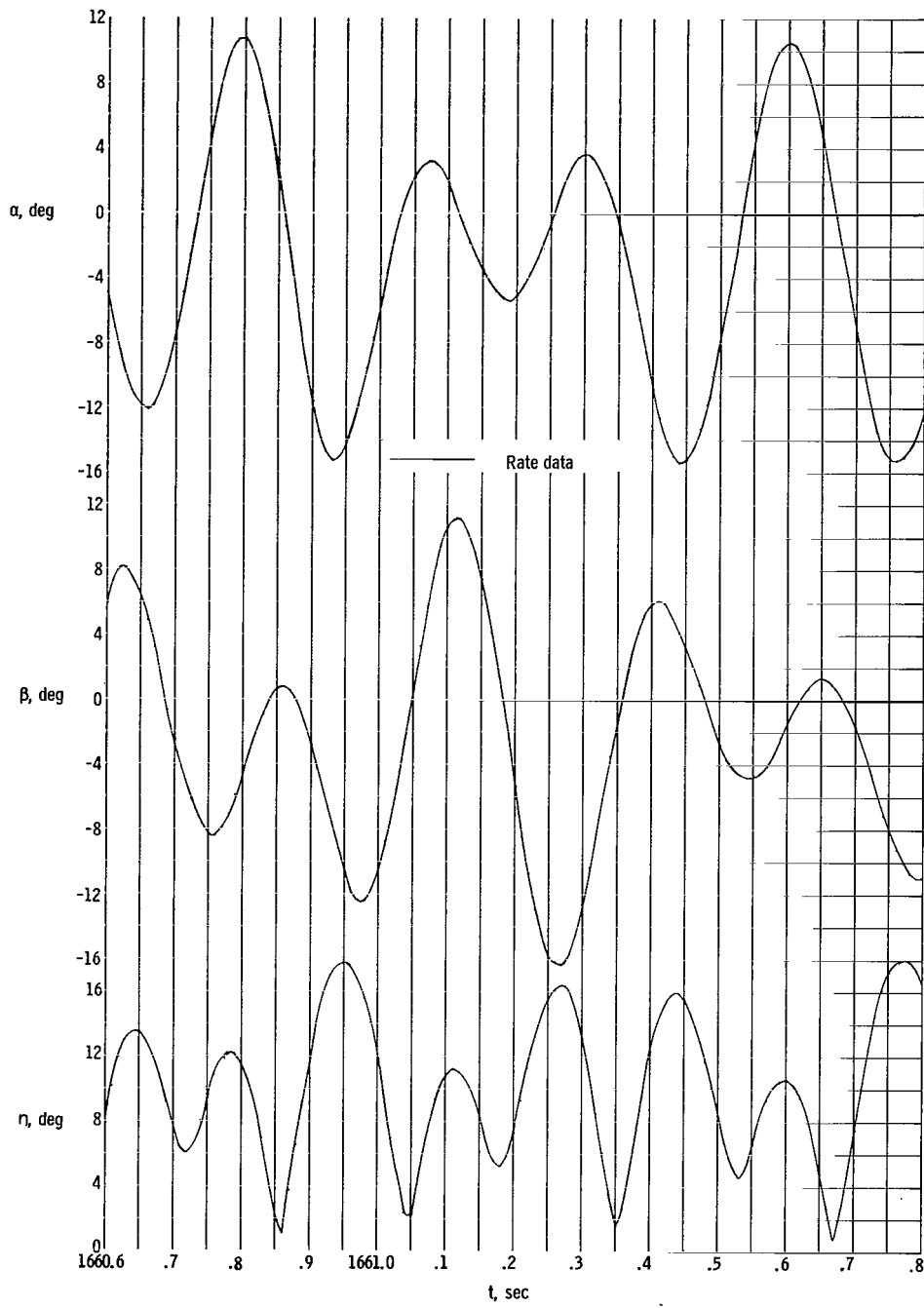
(j) $t = 1658.2$ to 1659.4 seconds.

Figure 16.- Continued.



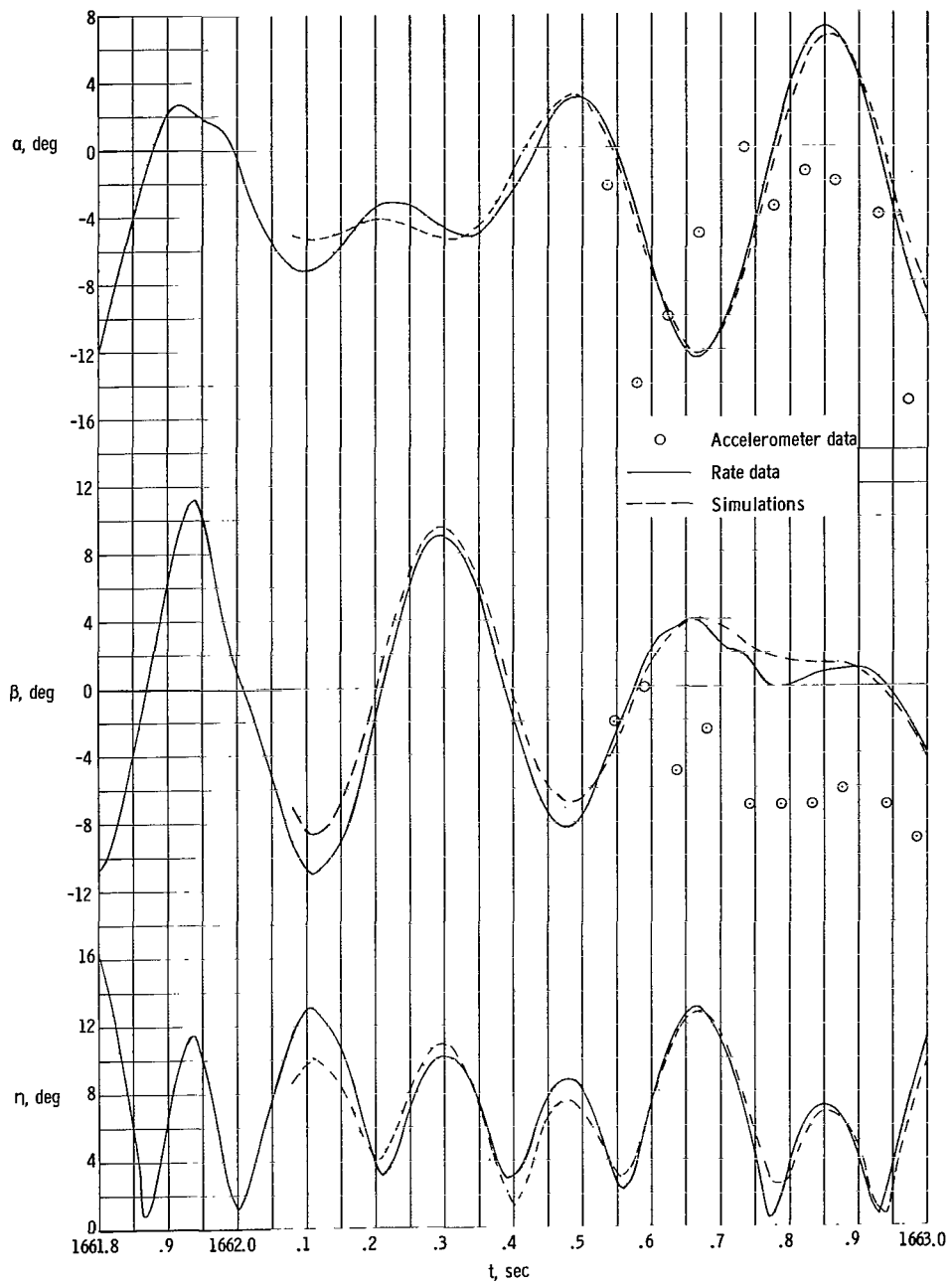
(k) $t = 1659.4$ to 1660.6 seconds.

Figure 16.- Continued.



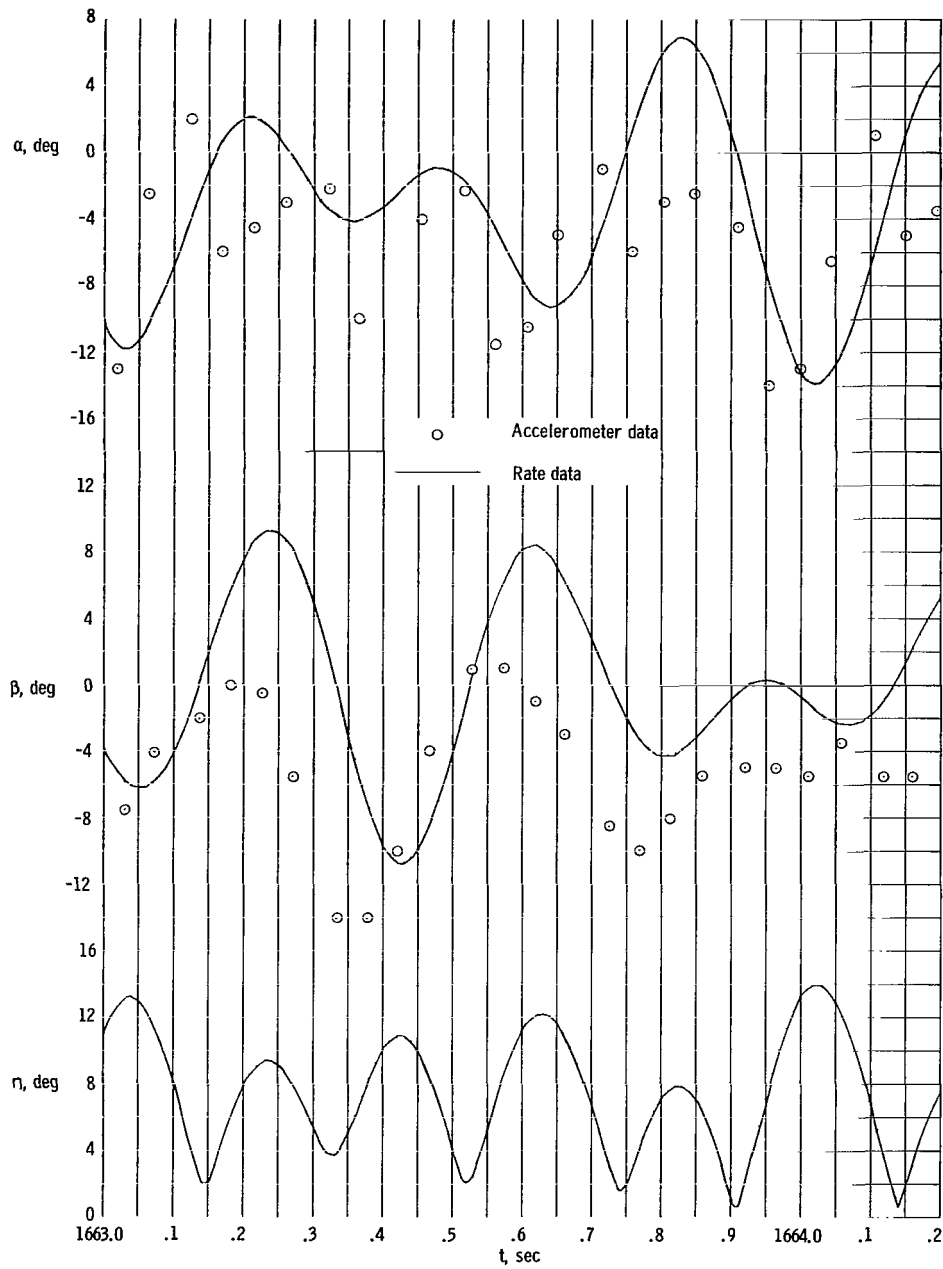
(I) $t = 1660.6$ to 1661.8 seconds.

Figure 16.- Continued.



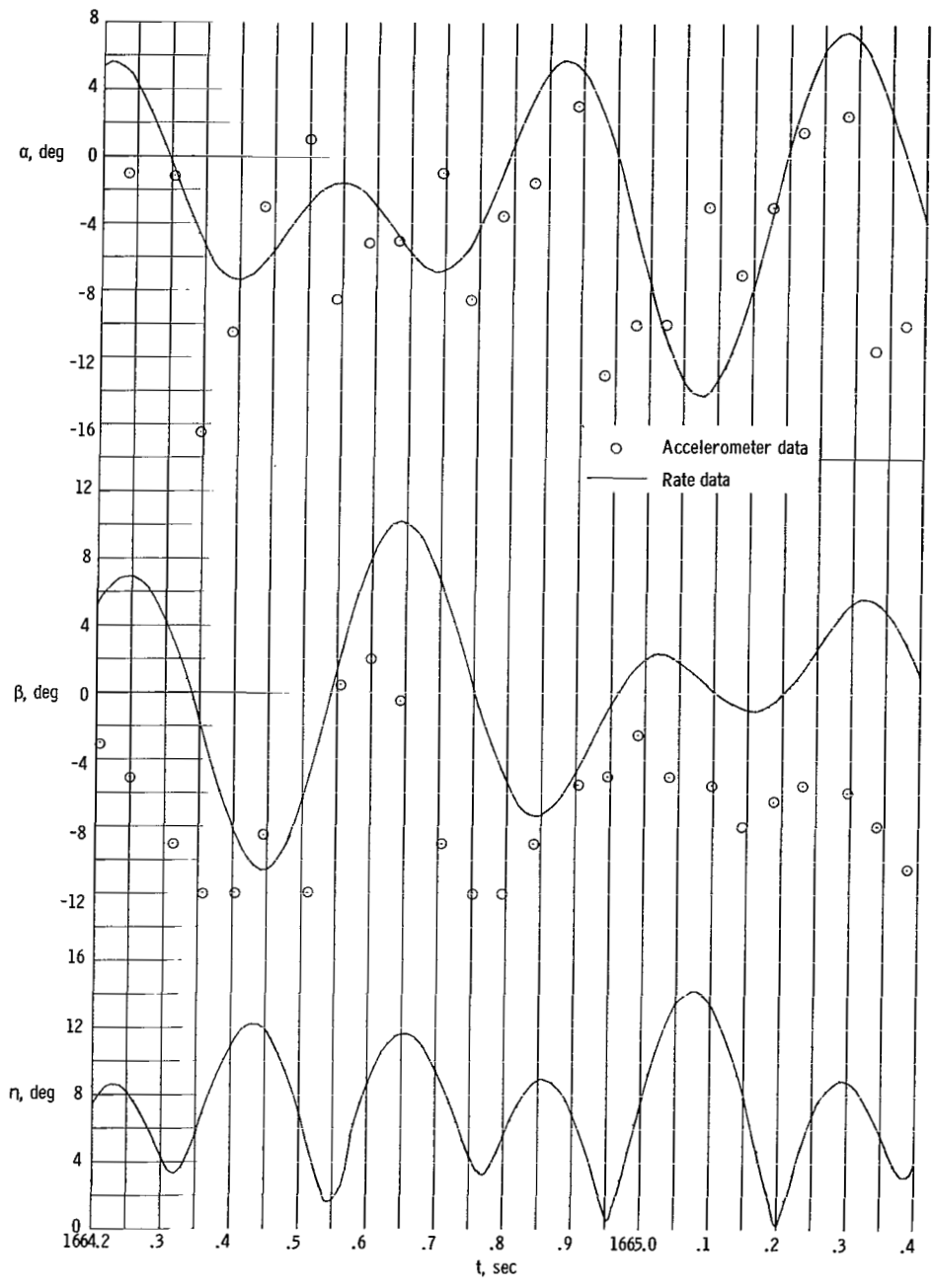
(m) $t = 1661.8$ to 1663.0 seconds.

Figure 16.- Continued.



(n) $t = 1663.0$ to 1664.2 seconds.

Figure 16.- Continued.



(o) $t = 1664.2$ to 1665.4 seconds.

Figure 16.- Concluded.

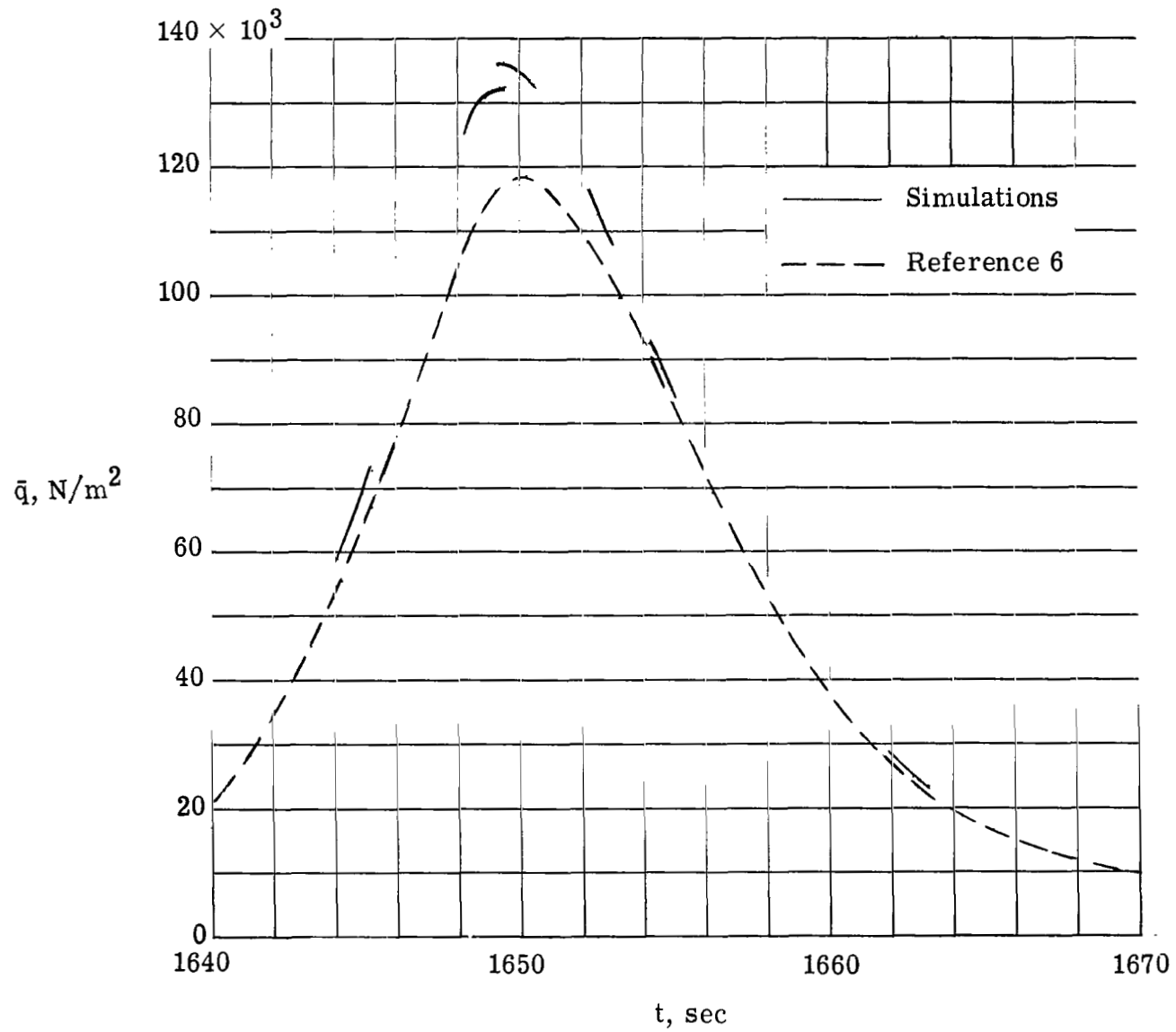


Figure 17.- Dynamic-pressure time history from trajectory simulation of reference 6 and dynamic-pressure values required by present simulations.

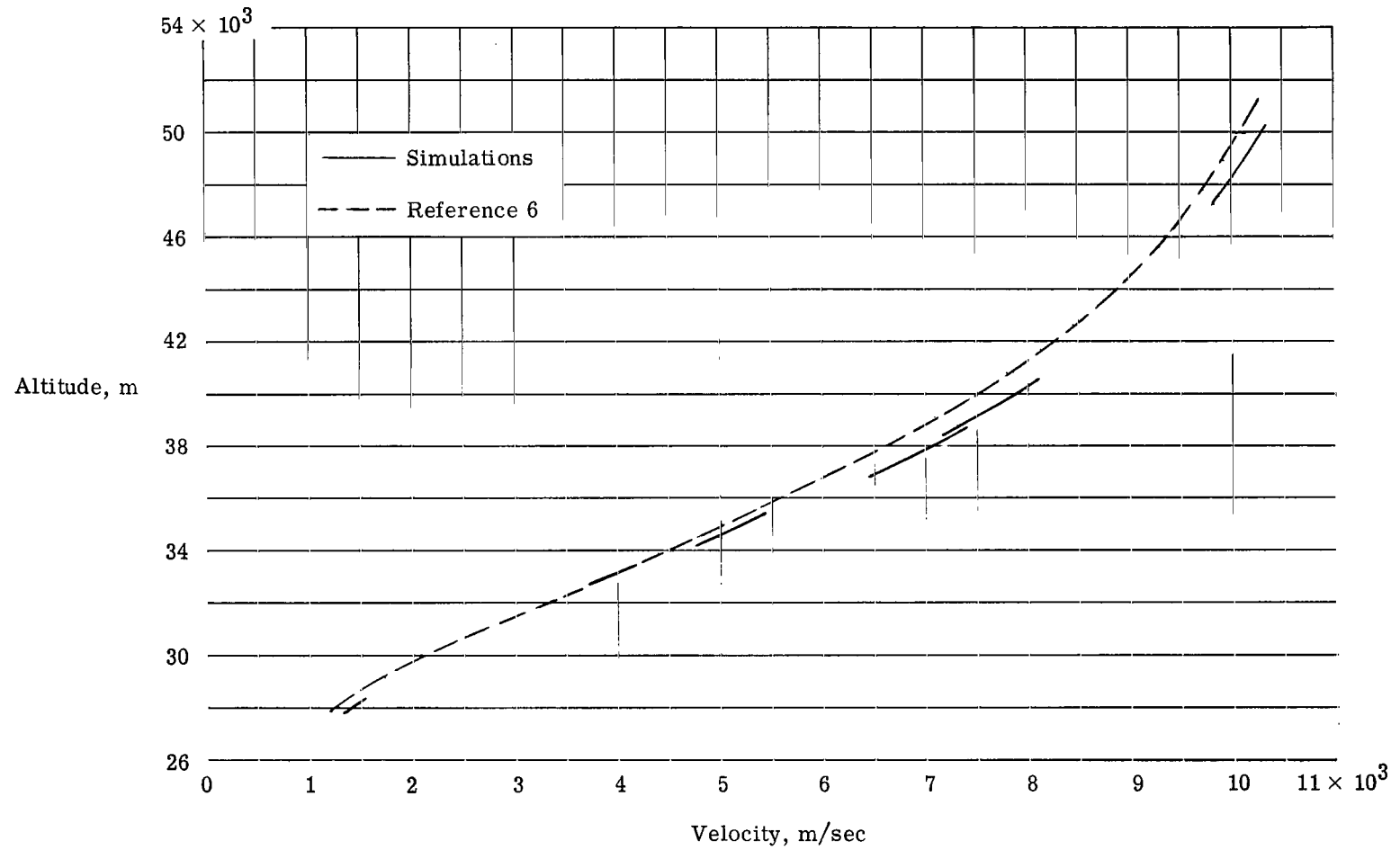


Figure 18.- Variation of altitude with velocity from trajectory simulation of reference 6 and altitude-velocity profile required by present simulations.

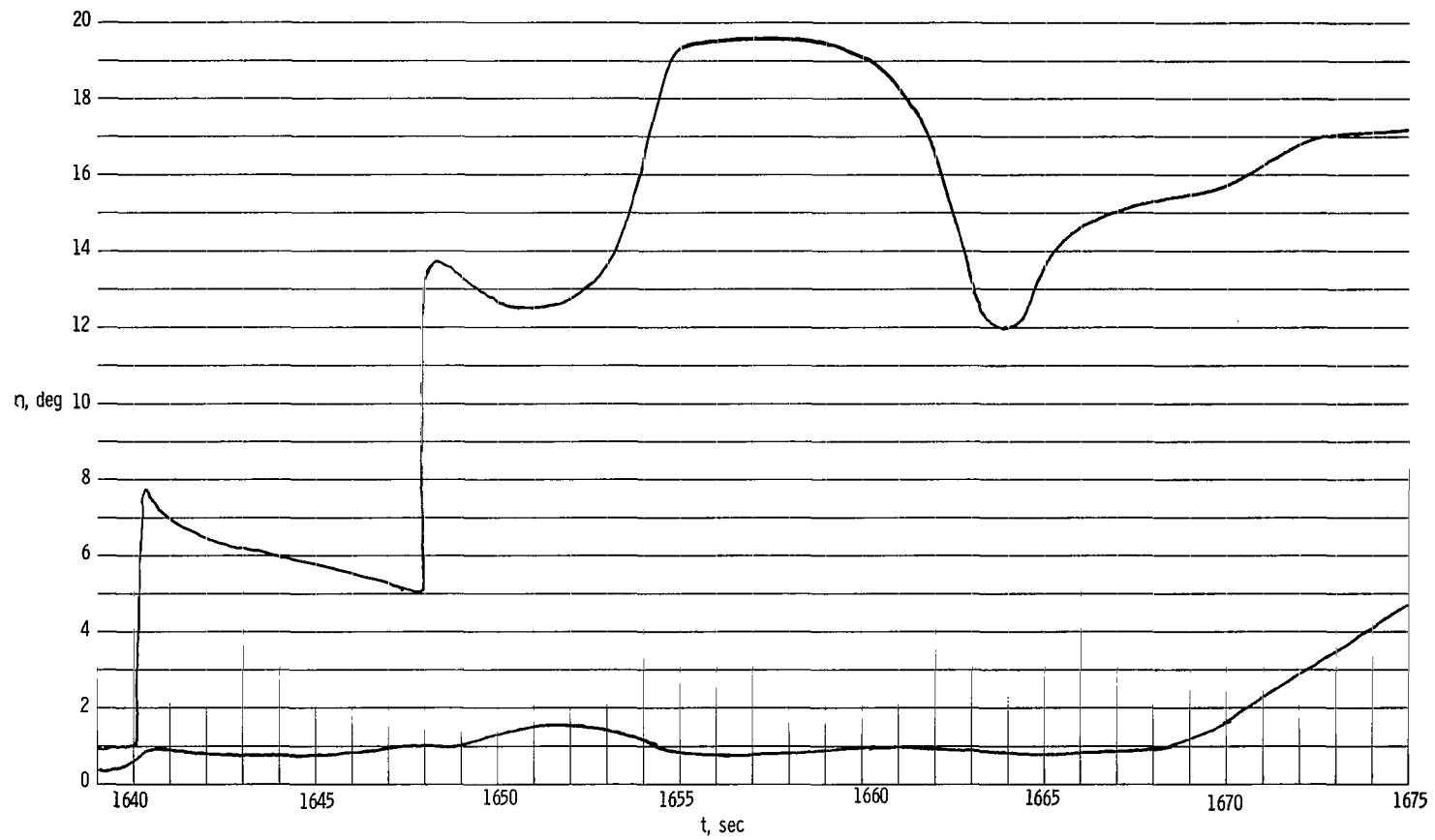


Figure 19.- Total angle-of-attack envelope.

"The aeronautical and space activities of the United States shall be conducted so as to contribute . . . to the expansion of human knowledge of phenomena in the atmosphere and space. The Administration shall provide for the widest practicable and appropriate dissemination of information concerning its activities and the results thereof."

—NATIONAL AERONAUTICS AND SPACE ACT OF 1958

NASA SCIENTIFIC AND TECHNICAL PUBLICATIONS

TECHNICAL REPORTS: Scientific and technical information considered important, complete, and a lasting contribution to existing knowledge.

TECHNICAL NOTES: Information less broad in scope but nevertheless of importance as a contribution to existing knowledge.

TECHNICAL MEMORANDUMS: Information receiving limited distribution because of preliminary data, security classification, or other reasons.

CONTRACTOR REPORTS: Scientific and technical information generated under a NASA contract or grant and considered an important contribution to existing knowledge.

TECHNICAL TRANSLATIONS: Information published in a foreign language considered to merit NASA distribution in English.

SPECIAL PUBLICATIONS: Information derived from or of value to NASA activities. Publications include conference proceedings, monographs, data compilations, handbooks, sourcebooks, and special bibliographies.

TECHNOLOGY UTILIZATION PUBLICATIONS: Information on technology used by NASA that may be of particular interest in commercial and other non-aerospace applications. Publications include Tech Briefs, Technology Utilization Reports and Notes, and Technology Surveys.

Details on the availability of these publications may be obtained from:

SCIENTIFIC AND TECHNICAL INFORMATION DIVISION
NATIONAL AERONAUTICS AND SPACE ADMINISTRATION

Washington, D.C. 20546